

**TRANSFORMATION TECHNIQUES FROM  
SCALAR WAVE FIELDS TO POLARIZED  
OPTICAL FIELDS FOR  
WIDE-VIEWING-ANGLE HOLOGRAPHIC  
DISPLAYS**

A DISSERTATION SUBMITTED TO  
THE GRADUATE SCHOOL OF ENGINEERING AND SCIENCE  
OF BILKENT UNIVERSITY  
IN PARTIAL FULFILLMENT OF THE REQUIREMENTS FOR  
THE DEGREE OF  
DOCTOR OF PHILOSOPHY  
IN  
ELECTRICAL AND ELECTRONICS ENGINEERING

By  
Onur Külçe  
June 2018

TRANSFORMATION TECHNIQUES FROM SCALAR WAVE  
FIELDS TO POLARIZED OPTICAL FIELDS FOR WIDE-  
VIEWING-ANGLE HOLOGRAPHIC DISPLAYS

By Onur Külçe

June 2018

We certify that we have read this dissertation and that in our opinion it is fully adequate, in scope and in quality, as a dissertation for the degree of Doctor of Philosophy.

---

Levent Onural (Advisor)

---

Haldun M. Özaktaş

---

Mehmet Tankut Özgen

---

Gözde Akar

---

Seyit Sencer Koç

Approved for the Graduate School of Engineering and Science:

---

Ezhan Karaşan  
Director of the Graduate School

## ABSTRACT

# TRANSFORMATION TECHNIQUES FROM SCALAR WAVE FIELDS TO POLARIZED OPTICAL FIELDS FOR WIDE-VIEWING-ANGLE HOLOGRAPHIC DISPLAYS

Onur Külçe

Ph.D. in Electrical and Electronics Engineering

Advisor: Levent Onural

June 2018

Although the optical waves are vector-valued electromagnetic waves in nature, in holographic three-dimensional television (3DTV) research, an optical field to be displayed is usually modeled as a scalar wave field. In this respect, during the display phase, the scalar wave should be mapped to a polarized optical field with the intention that the desired scalar results are obtained through the generated polarized waves. This mapping has usually been implemented by directly equating the scalar field to the transverse field components of a simply polarized electric field. Although this conventional method is valid in paraxial fields, it becomes erroneous in wide-angle fields due to the nonnegligibly large longitudinal component of the electric field. In order to make a quantitative analysis of error arising from this mapping, a 2D linear-shift invariant (LSI) system is derived from Maxwell's equations, where the inputs and the output are the transverse and longitudinal components, respectively. The magnitude responses of the filters used in the system and some discrete simulations also indicate the longitudinal component becomes the dominant term in large propagation angles. In order to obtain desired scalar results in wide-angle fields, we develop two other techniques which can be used for different purposes. In the first technique, we apply a pair of 2D lowpass filters to the scalar field before mapping it to the transverse components, where the lowpass filters are derived so as to equalize the power spectra of the given scalar field and the resulting electric field. It is shown through discrete simulations that the excessive amplification of the longitudinal component and the deteriorations in the electric field intensity in large propagation angles are prevented by the specified lowpass filters. In the second technique, we first impose a constraint on the electric field vector to be generated such that the amplitude vector of a plane wave has a simple polarization state at plane which is orthogonal to the corresponding propagation direction. Then, the

components of the vector amplitude of the plane wave at that locally transverse plane are directly matched with the amplitude of the corresponding plane wave component of the scalar field. As a result of the second technique, the desired intensity images can be obtained if an imaging sensor captures a locally paraxial segment of the field on its observation plane; this is the case for common sensors. The validity of the second technique is justified through the computer simulation of a holographic display of a computer generated 3D object. In the simulation, the proposed method outperforms the conventional method and ends up with the correct intensity of the scalar field associated with the object at different tilted and rotated planes. In conclusion, use of the scalar theory of optics becomes possible also in wide-angle fields as a consequence of the developed techniques and the prescribed scalar results can be realized by means of wide-viewing-angle holographic displays.

*Keywords:* Wide-Viewing-Angle Holographic Display, Optical Field Generation, Scalar-to-Polarized Field Mapping, Optical Signal Processing.

## ÖZET

# GENİŞ GÖRÜŞ AÇILI HOLOGRAFİK EKРАНLAR İÇİN SAYIL DALGA ALANLARINDAN KUTUPLANMIŞ OPTİK ALANLARA DÖNÜŞÜM TEKNİKLERİ

Onur Külçe

Elektrik ve Elektronik Mühendisliği, Doktora

Tez Danışmanı: Levent Onural

Haziran 2018

Optik dalgalar doğada vektör değerli elektromanyetik dalgalar olarak var olduğu halde, holografik üç boyutlu televizyon (3DTV) çalışmalarında, görüntülenecek bir optik alan genellikle sayıl dalga olarak modellenir. Bu bağlamda, görüntüleme safhasında, üretilen kutuplanmış alanın istenilen sayıl sonuçları vermesi amacıyla sayıl dalga kutuplanmış bir optik alana eşlenmelidir. Bu eşleme, genellikle, sayıl alanın, basitçe kutuplanmış elektrik alanın enine alan bileşenlerine doğrudan eşitlenmesiyle gerçekleştirilmektedir. Bu geleneksel yöntem dar açılı alanlarda geçerli olduğu halde, geniş açılı alanlarda ihmal edilemez büyüklükteki boyuna bileşen sebebiyle hatalı sonuç vermektedir. Bu eşleme dolayısıyla ortaya çıkan hatanın sayısal analizini yapmak için, girdi ve çıktıları elektrik alanın enine ve boyuna bileşenleri olan iki boyutlu (2B) doğrusal-değişimden bağımsız (LSI) bir sistem Maxwell denklemlerinden türetilmiştir. Sistemde kullanılan süzgeçlerin büyüklük tepkisi ve sayısal benzetimler de boyuna bileşenin büyük yayılım açılarında baskın terim olduğunu göstermiştir. Geniş açılı alanlarda istenen sayıl sonuçları ortaya çıkarmak için, farklı amaçlarla kullanılacak iki teknik geliştirdik. İlk teknikte, sayıl dalgayı enine bileşenlere eşlemeden önce bir çift düşük frekans süzgecinden geçirdik. Bu düşük frekans süzgeçleri, verilen sayıl alan ile sonuçta ortaya çıkan elektrik alanın güç spektrumlarını eşitleyecek şekilde tasarlandı. Hesaplanan düşük frekans süzgeçlerinin, yüksek yayılım açılarında boyuna bileşenin aşırı güçlenmesini ve elektrik alan yoğunluğundaki bozulmaları önlediği sayısal benzetimlerle gösterilmiştir. İkinci teknikte, ilk olarak, üretilecek elektrik alan vektörüne, düzlem dalgaların genlik vektörünün ilgili yayılım yönüne dik düzlem üzerinde basit bir kutuplanma ilişkisine sahip olması şeklinde bir kısıt getirildi. Devamında, düzlem dalganın vektör genliğinin bölgesel dik düzlem üzerindeki bileşenleri, sayıl dalganın ilgili düzlem dalga bileşenine ait genliğine

doğrudan eşlendi. İkinci tekniğin sonucu olarak, istenen yeğinlik görüntüleri, eğer görüntüleme algılayıcıları yaygın olarak kullanılan algılayıcılarda olduğu gibi gözlem düzlemi üzerindeki alanın bölgesel dar açılı kısmını yakalıyorsa elde edilebilmektedir. İkinci tekniğin geçerliliği, bir bilgisayar üretimi 3B nesnenin holografik görüntülemesinin bilgisayar benzetimiyle doğrulanmıştır. Benzetimde, önerilen yöntem geleneksel yöntemle göre üstün gelmekte ve önerilen yöntemde nesneye ait sayıl alanın yeğinliği farklı eğik ve döndürülmüş düzlemlerde doğru olarak üretilmektedir. Sonuç olarak, geliştirilen yöntemler sayesinde, optiğin sayıl teorisinin kullanımı geniş açılı alanlarda da mümkün olmakta ve tasarlanan sayıl sonuçlar geniş görüş açılı holografik ekranlar aracılığıyla elde edilmektedir.

*Anahtar sözcükler:* Geniş Görüş Açılı Holografik Görüntüleme, Optik Alan Üretimi, Sayıl Alanları Kutuplanmış Alanlara Eşleme, Optik Sinyal İşleme.

## Acknowledgement

First of all, I would like to express my gratitude to my supervisor, Prof. Levent Onural, for his guidance and support throughout this work. I thank him especially for providing me with the opportunity to work in such an exciting research topic.

I thank Prof. Haldun M. Özaktaş, Prof. Mehmet Tankut Özgen, Prof. Gözde Akar and Prof. Seyit Sencer Koç for reading and commenting on this thesis. I also thank Prof. Ayhan Altıntaş for his participation in the thesis monitoring committee before his leave.

I thank our department administration, especially, the chair, Prof. Orhan Arıkan, and the administrative secretary, Mürüvet Parlakay, for creating an excellent research environment.

I also thank Prof. Levent Onural, Prof. Haldun M. Özaktaş, Prof. Enis Çetin, Prof. Orhan Arıkan, Prof. Erdal Arıkan and Dr. Alper Kutay for gaining me teaching skills.

I thank my wife, Ayyüce, my mother, Nihal, my father, Süha, and my brother, Orkun, for their continuous and invaluable support in every aspect of my life. I dedicate this dissertation to them.

Finally, I thank The Scientific and Technological Research Council of Turkey (TÜBİTAK) for the financial support in the form of a scholarship.

# Contents

<b>1</b>	<b>Introduction</b>	<b>1</b>
1.1	Background and Motivation . . . . .	1
1.2	Approach, Contributions and Limitations . . . . .	4
1.3	Scalar and Electromagnetic Wave Field Principles . . . . .	8
1.3.1	Scalar Diffraction Theory . . . . .	8
1.3.2	Electromagnetic Field Fundamentals . . . . .	11
1.4	Organization of the Dissertation . . . . .	14
<b>2</b>	<b>Conventional Scalar-to-Polarized Optical Field Transformation Technique and Its Limitations</b>	<b>16</b>
2.1	Theoretical and Numerical Evaluation of the Validity of the Con- ventional Scalar Approximation in Optical Wave Fields . . . . .	17
2.1.1	Systems Characterization for Electromagnetic Fields . . . . .	17
2.1.2	Properties of the Filters . . . . .	25
2.1.3	Vector versus Scalar Modeling of Optical Diffraction . . . . .	28
2.1.4	Digital Simulator . . . . .	30
2.2	Effect of the Flat Panel and Pixelated 3D Display Parameters on the Use of the Conventional Scalar Approximation . . . . .	36
2.2.1	Computation of the Longitudinal Component of Electric Field in Pixelated Flat Panel Displays . . . . .	36
2.2.2	Distribution of the Magnitude of the Longitudinal Compo- nent over the Frequency Plane . . . . .	38
2.2.3	Validity of the Conventional Scalar Approximation as a Function of the Pixel Size . . . . .	43

2.3	Analysis of Local Error in Wide Optical Fields due to the Conventional Scalar Approximation . . . . .	45
2.3.1	Importance of the Location of an Optical Sensor in Wide Optical Fields . . . . .	45
2.3.2	Computation of Local Error in Parallel and Tilted Planes . . . . .	47
2.3.3	Simulation Results . . . . .	49
2.4	Summary . . . . .	52
<b>3</b>	<b>Set of Electromagnetic Fields that can be Fully Represented by a Scalar Wave Field</b>	<b>55</b>
3.1	Systems Formulation of the Computation of the Magnetic Field from the Transverse Components of the Electric Field . . . . .	56
3.2	A General Constraint on the Scalar Representation of Electromagnetic Fields . . . . .	58
<b>4</b>	<b>Power Spectrum Equalizing Scalar-to-Polarized Optical Field Transformation Technique</b>	<b>62</b>
4.1	Inverse Filtering for Power Spectrum Equalization . . . . .	62
4.1.1	Simulation Results . . . . .	68
4.2	Use of the Power Spectrum Equalized Model in a Phase Retrieval Problem . . . . .	84
<b>5</b>	<b>Local Polarization-Constrained Scalar-to-Polarized Optical Field Transformation Technique</b>	<b>88</b>
5.1	Mapping a Given Scalar Field to a Local Polarization-Constrained Electric Field . . . . .	89
5.2	Scalar and Electric Fields Recorded by a Viewer Located at an Oblique Angle . . . . .	94
5.3	Conditions for a Satisfactory Reconstruction of a Given Scalar Field by the Local Polarization-Constrained Electric Field . . . . .	104
5.4	Design of Rotation Matrices Applicable to a Table-top Holographic Display Configuration . . . . .	108
5.5	Simulation Results . . . . .	113
<b>6</b>	<b>Conclusions</b>	<b>128</b>

<b>A Proof of the Energy of the Filter Functions <math>\mathcal{G}_{\{x,y\},p}(\hat{\mathbf{k}})</math> Being In-</b>	
<b>finite</b>	<b>146</b>

# List of Figures

2.1	The computation steps of the $z$ component of the electric field, including free space propagation, are shown as a block diagram. . . . .	23
2.2	For the propagating field case, a finite portion of the imaginary parts of the impulse responses of the filters are shown. $(x, y) = (0, 0)$ corresponds to the center of the images; the horizontal axis is $x$ and the vertical axis is $y$ . . . . .	24
2.3	The radial variation of $\mathcal{G}_{\{x,y\},p}^{polar}(\kappa, \phi)$ with the normalized frequency variable $v = \kappa/k$ is shown. The frequency variable $v$ is the normalized version of $\kappa$ by $k$ . . . . .	25
2.4	The magnitude response of the filters are shown as 3D surface plots, where $v_x$ and $v_y$ are the normalized frequency variables: $v_x = k_x/k$ and $v_y = k_y/k$ . . . . .	27
2.5	One period of the $x$ and $y$ components, which are the same, of the input field for the simulation is shown. . . . .	34
2.6	For $N = 2^{14}$ , the magnitude of the $z$ component corresponding to the input fields, $E_x[n, m, 0] = E_y[n, m, 0] = \cos\left[\frac{\pi}{N}(n^2 + m^2)\right]$ is shown at a logarithmic scale for better illustration. . . . .	35

2.7 The  $\left| \mathcal{E}_z(\hat{\mathbf{k}}) \right|$  of Equation 2.54 are shown as gray scale images in three cases. In the figures, the frequency axes are along the spatial frequency variables  $k_x$  and  $k_y$  that correspond to the horizontal and vertical axes, respectively and  $k_x, k_y \in [-k, k)$ . The centers of the images correspond to  $(k_x, k_y) = (0, 0)$  point. The frequency increases along the horizontal axis from left to right, and along the vertical axis from top to bottom. The images are shown in log scale for better illustration. The horizontal and vertical lines in Figure 2.7c indicate the locations of 1D cross-sections shown in Figure 2.8. . . . . . 41

2.8 Horizontal and vertical profiles of Figure 2.7c at  $k_y = k/8$  and  $k_x = 0$  are shown. . . . . 42

2.9 The error in the scalar approximation,  $\epsilon$ , is shown for a single pixel as a function of the normalized width of the active region with respect to the wavelength, which is assumed as  $\lambda = 500 \text{ nm}$ . 44

2.10 A holographic display setup is shown in a 2D space. The display is located at the  $z = 0$  plane and different optical sensors, which are shown in different geometries, are located at different parallel and tilted planes. . . . . 46

2.11 The chosen signals which are used in the simulation are shown. For the sake of brevity, the simulations are performed for one-dimensional signals and the  $y$  component of the electric field is assumed to be zero. Figure 2.11a presents the real part of the chosen scalar field which is also associated with the  $x$  component of the electric field. Figure 2.11b presents the magnitude of the resulting  $z$  component of the electric field, that is also the source of error in the scalar approximation. Figure 2.11c shows the chosen digital Gaussian function with  $\hat{\sigma} = 32$ . . . . . 51

- 2.12 Simulation results are shown. Figure 2.12a presents the space-frequency analysis of the  $x$  component of the electric field, that is given by Equation 2.67 and its real part is shown in Figure 2.11a. Figure 2.12b presents the space-frequency analysis of the  $z$  component of the electric field, whose magnitude is shown in Figure 2.11b. Figure 2.12c shows the local error, which is calculated by Equation 2.70, in the scalar approximation for the tested signals. . . . 53
- 4.1 The magnitude of the corresponding transfer functions which satisfy Equation 4.4 are shown for different polarizations in propagating fields. The centers of the images correspond to  $(k_x, k_y) = (0, 0)$ . 67
- 4.2 The test patterns, which are given by Equations 4.29, 4.30 and 4.32, are shown.  $n$  and  $\hat{p}$  increase from left to right and  $m$  and  $\hat{q}$  increase from top to bottom. The top-left of the images shown in Figures 4.2a and 4.2b correspond to  $(n, m) = (0, 0)$  and the center of the image shown in Figure 4.2c corresponds to  $(\hat{p}, \hat{q}) = (0, 0)$ . . . 73
- 4.3 The reconstructed intensity patterns for the first simulation are shown for  $C = 1$ , i.e. diagonally polarized field. The original intensity pattern is shown in Figure 4.3a. The resulting intensity patterns due to the conventional and proposed mappings are shown in Figures 4.3b, and 4.3c, respectively. Before jointly mapping the patterns to the grayscale range, the contrast of  $\hat{P}_{con}[n, m]$  is linearly shrank. Figure 4.3d shows the independently gray-scaled version of Figure 4.3c. Figure 4.3e shows  $\hat{P}_{con}[n, m]$  in the log-scale. The top-left corner of the images correspond to  $(n, m) = (0, 0)$ . 76

4.4 The reconstructed intensity patterns for the first simulation are shown for  $C = -j$ , i.e. left-hand circularly polarized field. The original intensity pattern is shown in Figure 4.4a. The resulting intensity patterns due to the conventional and proposed mappings are shown in Figures 4.4b and 4.4c, respectively. Before jointly mapping the patterns to the grayscale range, the contrast of  $\hat{P}_{con}[n, m]$  is linearly shrank. Figure 4.4d shows the independently gray-scaled version of Figure 4.4c. Figure 4.4e shows  $\hat{P}_{con}[n, m]$  in the log-scale. The top-left corner of the images correspond to  $(n, m) = (0, 0)$ . . . . . 78

4.5 The test patterns for the second simulation are shown. The image plane is assumed to be located 20 cm away from the SLM. Wavelength is 500 nm. The top-left corner of the images correspond to  $(n, m) = (0, 0)$ . . . . . 81

4.6 The reconstructed intensity patterns are shown for  $C = 0$ , i.e. x-polarized field. The original intensity pattern is shown in Figure 4.5a, and the intensity patterns as the result of the conventional and proposed mappings are shown in Figures 4.6a, 4.6b, and 4.6c, respectively. The patterns shown in these three figures are mapped to gray level images using the same scale. Figure 4.6d shows the independently gray-scaled version of Figure 4.6c. The top-left corner of the images correspond to  $(n, m) = (0, 0)$ . . . . . 83

4.7 The simulation results are shown as gray scale images at  $z = 0$  and  $z = d = 20$  cm for  $N = 512$ . The top-left corners correspond to  $(n, m) = (0, 0)$ ,  $n$  and  $m$  increase from left to right and from top to bottom, respectively. Different gray scales are used in Figures 4.7c and 4.7d, as indicated by the color bars, for the sake of visibility of the underlying Gaussian pattern which is dominated by the amplified random noise due to the uncompensated highpass effect in the conventional procedure. The results indicate that the scalar intensity patterns are preserved if the proposed mapping is applied instead of the conventional mapping. . . . . 87

5.1 The angular variables of a unit normal of a viewer,  $V$ , which is located at a  $z_V = l_V \in \mathbb{R}^+$  plane is shown. . . . . 95

5.2 The projections of the passband of a filter, that is shown as a red thick arc, to both local and global spatial frequency domains are shown. For simplicity, the illustration includes a 2D frequency domain associated with a 2D space, by omitting the  $k_x$  and  $k_{x_V}$  axes. The projection of the passband region onto the global frequency axis includes the frequency interval  $k_2 < k_y < k_1$  and the projection onto the local frequency axis includes the interval  $-k_c/2 < k_{y_V} < k_c/2$ . It can be seen that the bandwidth in the local frequency axis is larger than the bandwidth in the global frequency axis. That is,  $k_c > |k_1 - k_2|$ . . . . . 99

5.3 A sample collection of electric field vectors are shown in a 2D space ( $x$  and  $x_V$  axes are omitted). The dotted line in both figures indicates the 2D cross-section of the field at a  $z_V$  plane. For simplicity,  $y_V$  coordinate axis is not shown. The sum of the vector components at each point are the same in both figures. However, their decomposition along different coordinate axes become different in two figures. . . . . 102

5.4 A generic table-top wide-viewing-angle holographic display is shown. The planar display which is shown in solid black color lies on the  $x$ - $y$  plane. The 3D image, which is represented as a colored ghost icosahedron, is generated by the display. Each figure shows a different scene of the ghost image captured from a different angle. So, each captured scene is a different paraxial segment of the field diffracted from the display. . . . . 109

5.5 A sample rotated coordinate frame on a transverse plane are shown for a given  $\hat{\mathbf{k}}$ , where  $\boldsymbol{\kappa}_{z_{\mathbf{k}}}(\hat{\mathbf{k}})$  is the unit vector along the propagation direction implied by  $\hat{\mathbf{k}}$  and also represents the unit normal of the observation plane of a viewer  $V$ , that is shown in transparent gray color. The axis whose unit vector is denoted as  $\boldsymbol{\kappa}_{y_{\mathbf{k}}}(\hat{\mathbf{k}})$  points towards the positive  $z$ -axis and intersects with it. Also, the axis whose unit vector is denoted as  $\boldsymbol{\kappa}_{x_{\mathbf{k}}}(\hat{\mathbf{k}})$  lies parallel to the  $x$ - $y$  plane. 110

5.6 The 3D rigid object whose hologram is generated for the computer simulation and the chosen coordinate frame are shown. . . . . 118

5.7 The magnitudes of the field components on the SLM surface are shown. Figure 5.7a shows the patterns for the conventional method, where the scalar field and the  $x$  and  $y$  components of the electric field are, apart from a constant multiplier, equal. Figures 5.7b and 5.7c show the  $x$  and  $y$  components for the proposed model, respectively. The centers of the images correspond to  $(m, n) = (0, 0)$ . . . . . 120

5.8 Simulation results for  $(\theta, \phi) = (37^\circ, 316^\circ)$  case is shown. Figures 5.8a, 5.8b and 5.8c are the desired scalar field intensity, the obtained intensity pattern due to the conventional mapping and the obtained intensity pattern due to the proposed mapping, respectively, where  $I_s$ ,  $I_{E,con}$  and  $I_{E,pro}$  are jointly mapped to the grayscale levels. Figure 5.8d shows the normalized histogram of the pointwise polarization state of the resulting electric field due to the proposed mapping. . . . . 124

5.9 Simulation results for  $(\theta, \phi) = (60^\circ, 176^\circ)$  case is shown. Figures 5.9a, 5.9b and 5.9c are the desired scalar field intensity, the obtained intensity pattern due to the conventional mapping and the obtained intensity pattern due to the proposed mapping, respectively, where  $I_s$ ,  $I_{E,con}$  and  $I_{E,pro}$  are jointly mapped to the grayscale levels. Figure 5.9d shows the normalized histogram of the pointwise polarization state of the resulting electric field due to the proposed mapping. . . . . 125

5.10 Simulation results for  $(\theta, \phi) = (70^\circ, 74^\circ)$  case is shown. Figures 5.10a, 5.10b and 5.10c are the desired scalar field intensity, the obtained intensity pattern due to the conventional mapping and the obtained intensity pattern due to the proposed mapping, respectively, where  $I_s$ ,  $I_{E,con}$  and  $I_{E,pro}$  are jointly mapped to the grayscale levels. Since  $I_s$  and  $I_{E,pro}$  cannot be seen clearly in Figures 5.10a, and 5.10c, we map  $I_s$  and  $I_{E,pro}$  jointly to the grayscale levels and show in Figures 5.10d and 5.10e, respectively. Figure 5.10f shows the normalized histogram of the pointwise polarization state of the resulting electric field due to the proposed mapping. . . . . 127

# Chapter 1

## Introduction

In this dissertation, we develop novel techniques for polarized optical field generation that can be utilized in various wide-viewing-angle holographic display applications.

### 1.1 Background and Motivation

From a physical and scientific point of view, an effort has been continuously made to understand the nature of light since the ancient ages. Scientists and mathematicians have developed different, but related theories to explain the behavior of light for different circumstances. Besides its novel aspects, it is logical to expect from a new theory that it should be able to explain all the optical phenomena which have already been explained by the old ones. So, a new theory should cover all the aspects of older theories. On the other hand, from a technological and application point of view, engineers do not easily abandon a simpler theory. This attitude of engineers is quite acceptable, because, as long as that old theory leads to novel optical designs and meets the demands coming from the society, there is no need to struggle with the new analytical and mathematical complexities. However, it is quite sure that, as necessities and demands which cannot be met

by the older theories arise, transition to a new theory becomes inevitable for the engineers, as well.

The research on holography, which was invented by Denis Gabor in 1948 [1], is a good example of this relation between science and technology. Although it has been known from the times of James Clerk Maxwell (1860) that the light is an electromagnetic wave, and hence it has a vectorial nature, engineers who work on holography and three-dimensional television (3DTV) have generally used the scalar wave theory of light in their designs, where the roots of this theory dates back to 17<sup>th</sup> century. The reason that the scalar theory has not been abandoned is the observation that it explains some fundamental optical phenomena, such as interference and diffraction in free space needed to implement holographic designs for small propagation angles. Since the scalar wave theory has been sufficient to explain and understand holography, apparently, there was no driving force to modify the underlying fundamental theory. However, as it is envisioned in some science-fiction movies, the society expects from a good quality true 3DTV that a viewer should be able to see a displayed 3D ghost image from any angle; this 3D image should be optically indistinguishable from its original 3D scene [2]. At this point, the scalar theory fails to meet this demand and the electromagnetic nature of light should be taken into account as we need to start dealing with wide-angle optical fields.

The monochromatic scalar wave theory characterizes an optical wave field in free space in terms of a complex amplitude defined at each point in 3D space. As it is given by the scalar diffraction theory, it is sufficient to characterize the scalar field only over a two-dimensional (2D) plane; by using the field information over a 2D plane, the optical field can be calculated over the entire 3D space [3–10]. The physical interference of optical wave fields can also be explained by using the simple mathematical addition operation on the complex amplitudes of the interfering waves. This analytical formulation paves the way for the application of the well-known and easy-to-use Fourier transform and signal processing techniques in scalar optical fields, as well [4, 9–12]. Moreover, if the intensity of the optical field is of concern, which is the case in many display and imaging applications, calculation of the magnitude square of the complex amplitude gives the predicted

and desired intensity pattern.

As opposed to the scalar characterization, the vector field characterization of an optical field requires specifying a direction information in addition to the complex amplitude at each point in 3D space. This direction information cannot be chosen arbitrary and the generated polarized field should obey Maxwell's equations. In some cases, it might be quite difficult to satisfy these equations. So, if the polarization information is not important in an application, an optical engineer or a designer may choose not to deal with the electromagnetic constraints due to such computational complexities. Moreover, a desired scalar result can be obtained using different polarized light field configurations. In other words, different electromagnetic fields may yield the same scalar result. So, imposing a polarization constraint in an optical field may lead to a misconception that the desired scalar results can be obtained only if the imposed polarization constraint is applied. As a result, the scalar characterization is preferable over the electromagnetic characterization in analysis and design of optical fields in various disciplines, such as computational optics, computational imaging and phase retrieval [13–20], conventional holography [1,4,10,12,21–29], 3DTV [24,25,27,29–55] and phase-space representations [8,56–59].

On the other hand, although the scalar characterization of an optical field is useful in many cases, during the realization and implementation phase of an optical design, it is required to include the polarization state of the generated optical field into the calculations due to the physical constraints imposed by Maxwell's equations. Due to this vector field formalism requirement, the operations of commonly used 3D displays and spatial light modulators (SLMs) depend on electromagnetic principles [4,12,60–63]. Since these displays fill the 3D space with a polarized light, a scalar field generated by such a display is necessarily accompanied by the generated polarization state. Therefore, in order to obtain the desired scalar results, an appropriate transformation should be determined between the given scalar field and the generated polarized optical field.

As the simplest transformation method, it is analytically shown for a paraxial imaging system that, the scalar field can be directly mapped to the transverse field

components of a simply polarized electric field in [3, 64]. In [65], it is stated that the scalar diffraction theory characterizes the electromagnetic field diffraction under paraxial conditions for simply polarized fields. This theoretical treatment has been justified in a number of setups that use SLMs [38, 39, 42–44, 48, 66], where a paraxial scalar optical field is realized by generating a simply polarized electromagnetic field. Since these fields are paraxial, the longitudinal component of the electric field can be neglected and there is no need to take this component into account in such fields. On the other hand, in the case of wide-angle fields, the longitudinal component becomes nonnegligibly large. Therefore, direct mapping of a given scalar field to the transverse field components of a simply polarized vector field, where we call this mapping as the “conventional mapping” throughout the dissertation, ends up with a large error due to the large longitudinal component. So, in order to prevent such errors in large propagation angles, more sophisticated transformation techniques should be performed for the scalar-to-vector field mapping, where this aim generates the motivation behind this work.

## 1.2 Approach, Contributions and Limitations

It is well known that the scalar diffraction between parallel planes can be formulated as a 2D linear-shift invariant (LSI) system [4, 9, 10, 12]. Since the plane waves are eigenfunctions of LSI systems, the input-output relations of such systems can be simply written as a multiplication operation in the 2D Fourier domain. Moreover, through the fast Fourier transform (FFT) algorithm, computer simulations for the LSI systems can be completed in a reasonable computation time [67]. Besides this analytical and computational simplicity, since the spatial frequency of a plane wave corresponds to the propagation direction of that plane wave, Fourier transform techniques give a great insight to analyze a field at different propagation angles. In this respect, we adopt this plane wave expansion approach and use signal processing terminology throughout the dissertation.

As it will be shown in the following chapters, the plane wave expansion method simplifies not only the free space propagation calculations but also the relations

between the scalar components of electromagnetic field. That is, we are going to show that the computation between the scalar components of electromagnetic fields can be expressed also as 2D LSI systems; that leads to simple multiplications in the Fourier domain. By investigating the transfer functions of these systems, we end up with an evaluation tool for the validity of the conventional scalar-to-vector field mapping. In this way, we investigate the limitations of the conventional method for different circumstances.

In this dissertation, we develop novel transformation techniques from a given scalar wave field to a polarized optical field such that anticipated scalar results can be realized through electromagnetic waves in wide-viewing-angle holographic display applications. In order to obtain scalar results through polarized optical fields, first, a one-to-one relation between the set of scalar fields and the set of polarized light fields which will be generated by a display should be determined. Such a relation enables a unique transition between scalar and polarized light fields. In this respect, we say that a 3D scalar field *fully* represents a 3D electromagnetic field if there is a one-to-one relation between the scalar field and the corresponding electromagnetic field. In other words, if there is a predetermined procedure in finding a 3D electromagnetic field from a given scalar field uniquely, then we say that a scalar field fully represents the corresponding electromagnetic field. However, establishing a unique relation between the scalar and polarized fields may not be always useful. If the predetermined procedure becomes analytically and computationally complex, then, representation of the polarized field through a scalar wave field may not be feasible and the set of scalar results which can be obtained through generated polarized fields may be limited to a limited number of cases. In this respect, in order to set up a simple one-to-one relation between scalar and polarized optical fields, we further limit the definition of the *full representation* of electromagnetic fields to those cases, where the predetermined procedure used to calculate the polarized field from the scalar field is the same at each 2D planar cross-section of 3D space. We also find this definition of *full representation* useful since the free space propagation formula between parallel planes are the same for both the scalar fields and the scalar components of the vector field. So, if there is a unique relation between a scalar field and a

polarized field at a 2D plane, then, it is guaranteed that this relation is preserved at each 2D plane.

In determining a method for the full representation, we first put a constraint on the electromagnetic fields that will be generated by a display. In the constrained electromagnetic fields, the two components of the electric field, which are the transversal ones with respect to the normal of the chosen 2D plane orientation, become related to each other through an imposed one-to-one 2D LSI operation. This relation can be imposed due to either physical capabilities of the display or preference of a designer. By putting such a constraint, we provide that the set of generated vector fields has one independent scalar component; other scalar components become dependent to that component through Maxwell's equations. As it will be shown, the relations which arise due to Maxwell's equations turn out to be 2D LSI transforms, as well. Then, we show that, if the independent scalar component of the vector field is computed using a given scalar field through another one-to-one 2D LSI system, then, that given scalar field fully represents the generated electromagnetic field. This transform which is used to compute the independent scalar component of the vector field from the given scalar field is completely up to the designer's choice and can be calculated adaptively for different purposes. In this respect, the chosen or derived 2D LSI transform between the given scalar field and the independent scalar component of the vector field may serve to obtain desired scalar results through a constrained polarized field generated by a holographic display.

After developing that constraint, we propose our first transformation method from a given scalar field to the constrained polarized optical field which will be generated by a 3D display. As a result of this transformation, the power spectra of a given scalar field and the resulting electromagnetic field become equal. This method can be used in different imaging and display applications. For example, in a nonparaxial imaging system where the electric field intensity is recorded, the deteriorations which occur due to the excessive amplification of the longitudinal component in large angles are compensated by the developed power spectrum equalization procedure. The power spectrum equalized model does not guarantee a pointwise equality between the scalar field intensity and the electric

field intensity. However, it can be used to decrease the undesired high-frequency components in the recorded intensity pattern. As another example, in an off-axis optical imaging setup where the magnitude of the 2D FT of the field at a tilted and rotated plane is recorded, then the proposed model leads to the exact scalar results.

In the second transformation method, we extend the simple polarization approach to wide-angle fields. That is, the mapping is performed by imposing a polarization constraint on the locally transverse field components of the plane waves. Then, we map the corresponding 2D FT of the scalar field to the 2D FT of the locally transverse field components of the electric field. Since these operations are carried out in the Fourier domain, resulting calculations again turn out to be 2D LSI systems. Moreover, the transfer functions which multiply the 2D FT of the scalar field satisfy the power spectrum equalized model. As a result, the resulting filters provide that the captured electric field segments by the observers located at tilted and rotated planes have a simple polarization state. So, intended scalar results, including scalar intensity, can be obtained at oblique planes through this locally simply polarized optical fields. The developed method is valid as long as a viewer located at a tilted and rotated plane can capture a paraxial segment of the field on that plane. This assumption is common and utilized in the formulation of the recorded field by a recording device [4].

Throughout this dissertation, computer simulations accompany the analytical developments. Therefore, the use of the proposed transform techniques are numerically justified. Moreover, in these simulations, the proposed models are compared to the conventional model and shown that the proposed ones outperform the conventional one.

## 1.3 Scalar and Electromagnetic Wave Field Principles

In this section, a brief review of the scalar and electromagnetic field fundamentals which form a basis for the rest of the dissertation will be presented. In accordance with the historical progress of optics science, the scalar diffraction theory will be outlined first. Then, based on Maxwell's equations, electromagnetic wave field basics will be given. The mathematical variables and parameters that are used throughout the dissertation are defined in this section, as well.

### 1.3.1 Scalar Diffraction Theory

In this dissertation, we assume that the optical field is a monochromatic field. So we omit the time dependency of the wave field,  $e^{-j\omega t}$ , where  $j = \sqrt{-1}$ ,  $t$  and  $\omega$  are the time and temporal frequency variables of the monochromatic field, respectively. Here,  $\omega$  equals to  $ck$  where  $c$  is the speed of light in the free space and  $k$  is the associated wave number of the optical field. The wave number is equal to  $2\pi/\lambda$  radians per unit length, where  $\lambda$  represents the wavelength [3].

Let a scalar function in three-dimensional (3D) space be denoted as  $S : \mathbb{R}^3 \mapsto \mathbb{C}$ . This function represents a physical scalar wave field if it satisfies the scalar wave or Helmholtz equation at each point  $\mathbf{r}$  [3–10],

$$\nabla^2 S + k^2 S = 0 \quad , \quad (1.1)$$

where  $\nabla^2$  is the scalar Laplacian operator. Equation 1.1 is independent from the choice of the coordinate system. Since we use the Cartesian coordinates to represent the spatial coordinates, we write the scalar field as  $S(\mathbf{r})$  where  $\mathbf{r} = [x \ y \ z]^T \in \mathbb{R}^3$ . Then, Equation 1.1 can be written in the Cartesian coordinates as

$$\frac{\partial^2 S(\mathbf{r})}{\partial x^2} + \frac{\partial^2 S(\mathbf{r})}{\partial y^2} + \frac{\partial^2 S(\mathbf{r})}{\partial z^2} + k^2 S(\mathbf{r}) = 0 \quad . \quad (1.2)$$

Next, we initially assume that  $S(\mathbf{r})$  can be written as a sum of plane waves. So, it can be represented in terms of a 3D inverse Fourier transform (IFT) relation

as [68]

$$S(\mathbf{r}) = \frac{1}{8\pi^3} \int \mathcal{S}_{3D}(\mathbf{k}) e^{j\mathbf{k}^T \mathbf{r}} d\mathbf{k} \quad , \quad (1.3)$$

where  $\mathbf{k} = [k_x \ k_y \ k_z]^T \in \mathbb{C}^3$  is the spatial frequency vector and indicates the propagation direction of plane wave components. Please note that, here we do not put a range on the integration as  $\mathbf{k}$  can take complex values in general and  $\mathcal{S}_{3D}(\mathbf{k}) \in \mathbb{C}$  is a function of all the three spatial frequency variables,  $(k_x, k_y, k_z)$ . If we insert  $S(\mathbf{r})$  as represented in Equation 1.3 to the Helmholtz equation, the requirement for the plane waves associated with the non-zero  $\mathcal{S}_{3D}(\mathbf{k})$ s arise as

$$k_x^2 + k_y^2 + k_z^2 = k^2 \quad . \quad (1.4)$$

Equation 1.4 is a result of the monochromaticity condition and a scalar function can represent a physically realizable monochromatic scalar wave if its plane wave components satisfy this equation. In other words, as long as  $k_x^2 + k_y^2 + k_z^2$  is equal to  $k^2$ , any physically realizable monochromatic scalar wave field can be written in terms of Equation 1.3.

Since  $k$  is an independent variable which is determined by the wavelength of the monochromatic field, one of the spatial frequency variables in Equation 1.4 becomes dependent on the other two variables. We choose  $k_z$  as the dependent term and write it as

$$k_z^2 = k^2 - k_x^2 - k_y^2 \quad . \quad (1.5)$$

Then, we put a constraint on the scalar wave fields that we deal with such that  $(k_x, k_y)$  pairs are always real valued. The physical implication of this restriction is that, the amplitude of the plane wave components of the scalar wave field does not decay or grow along  $x$  and  $y$  directions. Moreover, we put another constraint on the field such that, the propagation direction of the propagating plane waves along the  $z$  direction is always positive. Also, the evanescent plane wave components decay along the positive  $z$  direction. Under these restrictions,  $k_z$  can be written as

$$k_z = \begin{cases} \sqrt{k^2 - k_x^2 - k_y^2} & \text{if } k_x^2 + k_y^2 < k^2 \\ j\sqrt{k_x^2 + k_y^2 - k^2} & \text{otherwise} \end{cases} \quad . \quad (1.6)$$

As a result, since  $k_z$  can be uniquely determined from  $k_x$  and  $k_y$  under the imposed restrictions,  $S(\mathbf{r})$  can be written as a two-dimensional (2D) IFT relation as [3–11],

$$S(\mathbf{r}) = \frac{1}{4\pi^2} \int_{-\infty}^{\infty} \mathcal{S}(\hat{\mathbf{k}}) \mathcal{F}_z(\hat{\mathbf{k}}) e^{j\hat{\mathbf{k}}^T \hat{\mathbf{r}}} d\hat{\mathbf{k}} \quad , \quad (1.7)$$

where  $\mathcal{F}_z(\hat{\mathbf{k}}) = e^{jk_z z}$ ,  $\hat{\mathbf{k}} = [k_x \ k_y]^T$  and  $\hat{\mathbf{r}} = [x \ y]^T$ . The relation between  $\mathcal{S}(\hat{\mathbf{k}})$  and  $\mathcal{S}_{3D}(\mathbf{k})$  is given by [68]

$$\mathcal{S}(\hat{\mathbf{k}}) = 2\pi \mathcal{S}_{3D}(\mathbf{k}) \frac{k}{k_z} \quad . \quad (1.8)$$

Equation 1.7 can be seen as the fundamental relation that represents the relation between the 2D scalar field diffraction patterns on two parallel planes. That is, if the scalar field at  $z = 0$  plane is known,  $\mathcal{S}(\hat{\mathbf{k}})$  can be computed using the 2D Fourier transform (FT) relation as [3–11],

$$\mathcal{S}(\hat{\mathbf{k}}) = \int_{-\infty}^{\infty} S(\hat{\mathbf{r}}, 0) e^{-j\hat{\mathbf{k}}^T \hat{\mathbf{r}}} d\hat{\mathbf{r}} \quad . \quad (1.9)$$

Then, Equation 1.7 can be used to find the scalar field at any  $z$  plane using  $\mathcal{S}(\hat{\mathbf{k}})$ . Therefore, Equation 1.7 describes the scalar field diffraction between parallel planes and it can be seen as a 2D linear shift-invariant (LSI) system, where the input is  $S(\hat{\mathbf{r}}, 0)$  and the output is  $S(\hat{\mathbf{r}}, z)$ . By using the convolution property of the FT, the same relation between  $S(\hat{\mathbf{r}}, 0)$  and  $S(\hat{\mathbf{r}}, z)$  can be written in the space domain as [3–11],

$$S(\hat{\mathbf{r}}, 0) ** f_z(\hat{\mathbf{r}}) = S(\hat{\mathbf{r}}, z) \quad , \quad (1.10)$$

where  $**$  represents the 2D convolution operation and  $f_z(\hat{\mathbf{r}})$  can be computed from  $\mathcal{F}_z(\hat{\mathbf{k}})$  as a 2D IFT relation as [4, 5, 11]

$$\begin{aligned} f_z(\hat{\mathbf{r}}) &= \frac{1}{4\pi^2} \int_{-\infty}^{\infty} \mathcal{F}_z(\hat{\mathbf{k}}) e^{j\hat{\mathbf{k}}^T \hat{\mathbf{r}}} d\hat{\mathbf{k}} \\ &= -\frac{1}{2\pi} \frac{\partial}{\partial z} \left[ \frac{e^{jk|\mathbf{r}|}}{|\mathbf{r}|} \right] \\ &= -\frac{e^{jk\sqrt{|\hat{\mathbf{r}}|^2 + z^2}}}{2\pi} \left( jk - \frac{1}{\sqrt{|\hat{\mathbf{r}}|^2 + z^2}} \right) \frac{z}{|\hat{\mathbf{r}}|^2 + z^2} \quad . \end{aligned} \quad (1.11)$$

In Equation 1.11,  $f_z(\hat{\mathbf{r}})$  is called the impulse response of the Rayleigh-Sommerfeld free space propagation formulation [4, 11].

We call the scalar wave field a propagating field if the field does not include evanescent components. Hence,  $\mathcal{S}(\hat{\mathbf{k}})$  becomes always zero when  $|\hat{\mathbf{k}}| \geq k$  for such fields. In this case,  $\mathcal{F}_z(\hat{\mathbf{k}})$  can also be taken as zero for the values of  $|\hat{\mathbf{k}}|$  which are greater than or equal to  $k$ .

After presenting the scalar diffraction relation between parallel planes in this section, we are going to give the fundamental relations that should be satisfied by the electromagnetic fields in free space in the next section.

### 1.3.2 Electromagnetic Field Fundamentals

In order to develop the electromagnetic field relations that we use throughout the dissertation, we begin with Maxwell's equations for time harmonic fields in source-free and free space [3, 4, 6, 65, 69–71]:

$$\nabla \times \mathbf{E} = -j\omega\mu\mathbf{H} \quad , \quad (1.12)$$

$$\nabla \times \mathbf{H} = j\omega\epsilon\mathbf{E} \quad , \quad (1.13)$$

$$\nabla \cdot \mathbf{E} = 0 \quad , \quad (1.14)$$

$$\nabla \cdot \mathbf{H} = 0 \quad , \quad (1.15)$$

where  $\mathbf{E}$  and  $\mathbf{H}$  are the 3D electric and magnetic field vectors,  $\nabla \times$  and  $\nabla \cdot$  are the curl and divergence operations, and  $\epsilon$  and  $\mu$  are the electric permittivity and the magnetic permeability in free space [69]. Please note that, similar to the scalar wave equation given in Equation 1.1, Equations from 1.12 to 1.15 should be satisfied for all points in space and they are independent from the choice of the representation of the coordinate system. So, we initially omit the coordinate variables in these equations, as well.

Some relations between the field constants are [65, 69–71]

$$c = \frac{1}{\sqrt{\mu\epsilon}} \quad , \quad (1.16)$$

$$k = \omega^2 \mu \epsilon \quad , \quad (1.17)$$

$$\eta = \sqrt{\frac{\mu}{\epsilon}} \quad , \quad (1.18)$$

where  $\eta$  is the wave impedance of free space.

Vector valued functions,  $\mathbf{E}$  and  $\mathbf{H}$ , can represent a physically realizable electromagnetic field in source-free free space if they satisfy Maxwell's equations at each point in space. After some manipulations, the vector wave equations for electric and magnetic field vectors become [3, 4, 6, 65, 69–71]

$$\nabla^2 \mathbf{E} + k^2 \mathbf{E} = 0 \quad , \quad (1.19)$$

$$\nabla^2 \mathbf{H} + k^2 \mathbf{H} = 0 \quad , \quad (1.20)$$

where  $\nabla^2$  is the vector Laplacian operator [69]. These two equations are, again, independent from the choice of the coordinate representation.

Since we use the rectangular coordinate system throughout the dissertation, we write the electric and magnetic field vectors as  $\mathbf{E}(\mathbf{r}) = [E_x(\mathbf{r}) \ E_y(\mathbf{r}) \ E_z(\mathbf{r})]^T \in \mathbb{C}^3$  and  $\mathbf{H}(\mathbf{r}) = [H_x(\mathbf{r}) \ H_y(\mathbf{r}) \ H_z(\mathbf{r})]^T \in \mathbb{C}^3$ , respectively. If we insert the defined electric field and magnetic field vectors into the vector wave equations given in Equations 1.19 and 1.20, we obtain [3, 4, 6, 65, 69–71]

$$\nabla^2 E_x(\mathbf{r}) + k^2 E_x(\mathbf{r}) = 0 \quad , \quad (1.21)$$

$$\nabla^2 E_y(\mathbf{r}) + k^2 E_y(\mathbf{r}) = 0 \quad , \quad (1.22)$$

$$\nabla^2 E_z(\mathbf{r}) + k^2 E_z(\mathbf{r}) = 0 \quad , \quad (1.23)$$

$$\nabla^2 H_x(\mathbf{r}) + k^2 H_x(\mathbf{r}) = 0 \quad , \quad (1.24)$$

$$\nabla^2 H_y(\mathbf{r}) + k^2 H_y(\mathbf{r}) = 0 \quad , \quad (1.25)$$

$$\nabla^2 H_z(\mathbf{r}) + k^2 H_z(\mathbf{r}) = 0 \quad . \quad (1.26)$$

Equations from 1.21 to 1.26 can be seen as separate scalar wave functions, which can be substituted into Equation 1.1. Therefore, in order to find a physically

realizable set of scalar components of the electromagnetic field vectors, the same procedure as the one which is described in Section 1.3.1 can be followed. That is, we can write the electric and magnetic field vectors in the form of a Fourier relation as [4, 70–73],

$$\mathbf{E}(\mathbf{r}) = \frac{1}{4\pi^2} \int_{-\infty}^{\infty} \boldsymbol{\mathcal{E}}(\hat{\mathbf{k}}) \mathcal{F}_z(\hat{\mathbf{k}}) e^{j\hat{\mathbf{k}}^T \hat{\mathbf{r}}} d\hat{\mathbf{k}} \quad , \quad (1.27)$$

$$\mathbf{H}(\mathbf{r}) = \frac{1}{4\pi^2} \int_{-\infty}^{\infty} \boldsymbol{\mathcal{H}}(\hat{\mathbf{k}}) \mathcal{F}_z(\hat{\mathbf{k}}) e^{j\hat{\mathbf{k}}^T \hat{\mathbf{r}}} d\hat{\mathbf{k}} \quad , \quad (1.28)$$

where the 2D FT vectors,  $\boldsymbol{\mathcal{E}}(\hat{\mathbf{k}}) = [\mathcal{E}_x(\hat{\mathbf{k}}) \ \mathcal{E}_y(\hat{\mathbf{k}}) \ \mathcal{E}_z(\hat{\mathbf{k}})]^T$  and  $\boldsymbol{\mathcal{H}}(\hat{\mathbf{k}}) = [\mathcal{H}_x(\hat{\mathbf{k}}) \ \mathcal{H}_y(\hat{\mathbf{k}}) \ \mathcal{H}_z(\hat{\mathbf{k}})]^T$ , can be computed as,

$$\boldsymbol{\mathcal{E}}(\hat{\mathbf{k}}) = \int_{-\infty}^{\infty} \mathbf{E}(\hat{\mathbf{r}}, 0) e^{-j\hat{\mathbf{k}}^T \hat{\mathbf{r}}} d\hat{\mathbf{r}} \quad , \quad (1.29)$$

$$\boldsymbol{\mathcal{H}}(\hat{\mathbf{k}}) = \int_{-\infty}^{\infty} \mathbf{H}(\hat{\mathbf{r}}, 0) e^{-j\hat{\mathbf{k}}^T \hat{\mathbf{r}}} d\hat{\mathbf{r}} \quad . \quad (1.30)$$

Please note that, for the electromagnetic field that we deal with, we impose the same restrictions as the ones which we impose for the scalar fields. That is,  $(k_x, k_y)$  pairs are always real valued and  $k_z$  is in the form given in Equation 1.6.

Throughout the dissertation we use the following relations for the scalar components of the electromagnetic field vector in the Fourier domain [70, 72, 73]:

$$k_x \mathcal{E}_x(\hat{\mathbf{k}}) + k_y \mathcal{E}_y(\hat{\mathbf{k}}) + k_z \mathcal{E}_z(\hat{\mathbf{k}}) = 0 \quad , \quad (1.31)$$

$$k_x \mathcal{H}_x(\hat{\mathbf{k}}) + k_y \mathcal{H}_y(\hat{\mathbf{k}}) + k_z \mathcal{H}_z(\hat{\mathbf{k}}) = 0 \quad , \quad (1.32)$$

$$k\eta \mathcal{H}_x(\hat{\mathbf{k}}) - k_y \mathcal{E}_z(\hat{\mathbf{k}}) + k_z \mathcal{E}_y(\hat{\mathbf{k}}) = 0 \quad , \quad (1.33)$$

$$k\eta \mathcal{H}_y(\hat{\mathbf{k}}) - k_z \mathcal{E}_x(\hat{\mathbf{k}}) + k_x \mathcal{E}_z(\hat{\mathbf{k}}) = 0 \quad , \quad (1.34)$$

$$k\eta \mathcal{H}_z(\hat{\mathbf{k}}) - k_x \mathcal{E}_y(\hat{\mathbf{k}}) + k_y \mathcal{E}_x(\hat{\mathbf{k}}) = 0 \quad , \quad (1.35)$$

$$\eta^2 \left| \boldsymbol{\mathcal{H}}(\hat{\mathbf{k}}) \right|^2 - \left| \boldsymbol{\mathcal{E}}(\hat{\mathbf{k}}) \right|^2 = 0 \quad . \quad (1.36)$$

These relations can be obtained if the electric and magnetic field vectors, which are expressed as Equations 1.27 and 1.28, are replaced in Maxwell's equations. An explicit derivation of Equation 1.31 is given in Chapter 2.

Each scalar component of the electromagnetic field vector obeys the same formulation given for the scalar field as developed in Section 1.3.1. Therefore, the scalar field diffraction and the Rayleigh-Sommerfeld propagation formula can be used for the scalar components of the electromagnetic field, separately, as well. In this respect, under the imposed constraints, the scalar diffraction formulation completely characterizes the electromagnetic field diffraction. In other words, if all the scalar components of the electromagnetic field vector are known at  $z = 0$  plane, then, the diffraction pattern of the electromagnetic field can be found using the scalar operations which are given by Equations 1.9 and 1.7. However, although the scalar diffraction formulation can be used to find the electromagnetic field diffraction, a single scalar wave may not be adequate to represent the entire optical field, which is essentially a vector valued field. In the following chapters, we are going to first describe the validity of the conventional use of the scalar field theory on the representation of optical fields. We will also develop a constraint between the scalar components of the electromagnetic field such that the entire field can be represented by a single scalar wave under this constraint. Finally, we are going to demonstrate different scalar field representations for different purposes.

## 1.4 Organization of the Dissertation

In Chapter 2, we analyze the limitations of the conventional scalar approximation to describe the polarized optical fields for different circumstances. In that chapter, we first make the analysis from a theoretical perspective. Then, the effect of the display parameters of pixellated 3D displays on the validity of the conventional scalar approximation is discussed. Finally, a space-frequency decomposition based technique is proposed to analyze the success of the conventional scalar approximation in wide optical fields. In Chapter 3, we develop a constraint for

the electromagnetic fields such that the electromagnetic field having that constraint can be uniquely characterized by a single scalar wave field. In Chapter 4, we propose a mapping from a given scalar field to an electromagnetic field which will be produced by a display such that the power spectra of the scalar field and the resulting electromagnetic field become equal. The use of the power spectrum equalized model in a phase retrieval simulation is shown in that chapter, as well. In Chapter 5, we develop another scalar-to-vector field mapping such that the intended scalar results can be obtained in wide-viewing angle holographic displays. Finally in Chapter 6, we draw the conclusions.

## Chapter 2

# Conventional Scalar-to-Polarized Optical Field Transformation Technique and Its Limitations

A single scalar field cannot in general represent a vector-valued optical field. On the other hand, it is known that the scalar theory explains some optical phenomena such as interference, diffraction and holography [3, 4, 6, 12]. In this chapter, we present the limitations of the conventional scalar approximation in representing the optical wave field propagation in free space. The method that we employ is based on a signals and systems perspective derived from Maxwell's equations. We also develop a quantitative error measure which is used to measure the validity of the conventional scalar approximation. Based on this error measure, we present the effect of the display parameters on the use of the conventional scalar approximation in flat panel and pixelated 3D displays. Finally, we propose a space-frequency representation based error measure to analyze the local error in spatially wide extent optical fields. Sections 2.1, 2.2 and 2.3 are mainly based on our publications [74], [75] and [76], respectively.

## 2.1 Theoretical and Numerical Evaluation of the Validity of the Conventional Scalar Approximation in Optical Wave Fields

This section is mainly based on our publication [74]. We first describe the computation of the longitudinal,  $z$ , component of the electric field from  $x$  and  $y$  components as a 2D LSI model. Then, we discuss the validity of the conventional scalar approximation found in the literature based on this model. At the end of this section, we propose a numerical technique to measure the scalar approximation error when the field components cannot be analytically computed.

### 2.1.1 Systems Characterization for Electromagnetic Fields

As in Chapter 1, we first write the electric field as a 2D IFT relation

$$\mathbf{E}(\mathbf{r}) = \frac{1}{4\pi^2} \int_{-\infty}^{\infty} \boldsymbol{\varepsilon}(\hat{\mathbf{k}}) e^{j\mathbf{k}^T \mathbf{r}} d\hat{\mathbf{k}} \quad . \quad (2.1)$$

Here, we make the assumptions for the electromagnetic field that are described in Chapter 1. As a result of these assumptions,  $(k_x, k_y)$  pair becomes always real valued and  $k_z$  becomes

$$k_z = \begin{cases} \sqrt{k^2 - |\hat{\mathbf{k}}|^2} & \text{if } |\hat{\mathbf{k}}| < k \\ j\sqrt{|\hat{\mathbf{k}}|^2 - k^2} & \text{otherwise} \end{cases} \quad . \quad (2.2)$$

Since  $\mathbf{E}(\mathbf{r})$  should satisfy Gauss's law, it is possible to uniquely deduce the  $E_z$  component from the  $E_x$  and  $E_y$  components. In source-free space, Gauss's Law,

which is given by Equation 1.14, states that [69],

$$\begin{aligned}\nabla \cdot \mathbf{E}(\mathbf{r}) &= \frac{\partial E_x(\mathbf{r})}{\partial x} + \frac{\partial E_y(\mathbf{r})}{\partial y} + \frac{\partial E_z(\mathbf{r})}{\partial z} \\ &= \frac{j}{4\pi^2} \int_{-\infty}^{\infty} \mathbf{k}^T \boldsymbol{\mathcal{E}}(\hat{\mathbf{k}}) e^{j\mathbf{k}^T \mathbf{r}} d\hat{\mathbf{k}} \\ &= 0 \quad .\end{aligned}\tag{2.3}$$

In Equation 2.3,  $\nabla \cdot \mathbf{E}(\mathbf{r})$  is expressed as the linear combination of 2D complex sinusoidal basis functions  $e^{j\hat{\mathbf{k}}^T \hat{\mathbf{r}}}$  with the Fourier coefficients  $j\mathbf{k}^T \boldsymbol{\mathcal{E}}(\hat{\mathbf{k}}) e^{jk_z z}$ . Since the basis functions  $e^{j\hat{\mathbf{k}}^T \hat{\mathbf{r}}}$  constitute an orthogonal, and hence, linearly independent basis set, Equation 2.3 implies that,

$$\frac{j}{4\pi^2} \mathbf{k}^T \boldsymbol{\mathcal{E}}(\hat{\mathbf{k}}) e^{jk_z z} = 0 \quad .\tag{2.4}$$

After simplifications, Equation 2.4 turns out to be

$$\mathbf{k}^T \boldsymbol{\mathcal{E}}(\hat{\mathbf{k}}) = k_x \mathcal{E}_x(\hat{\mathbf{k}}) + k_y \mathcal{E}_y(\hat{\mathbf{k}}) + k_z \mathcal{E}_z(\hat{\mathbf{k}}) = 0 \quad .\tag{2.5}$$

Equation 2.5 states that the electric field coefficient and propagation direction vectors are orthogonal to each other. From Equations 2.2 and 2.5 we find,

$$\mathcal{E}_z(\hat{\mathbf{k}}) = -\frac{k_x \mathcal{E}_x(\hat{\mathbf{k}}) + k_y \mathcal{E}_y(\hat{\mathbf{k}})}{\sqrt{k^2 - |\hat{\mathbf{k}}|^2}} \quad .\tag{2.6}$$

Finally we obtain  $E_z(\mathbf{r})$  from  $E_x(\mathbf{r})$  and  $E_y(\mathbf{r})$  as

$$E_z(\mathbf{r}) = \frac{1}{4\pi^2} \int_{-\infty}^{\infty} \frac{-k_x \mathcal{E}_x(\hat{\mathbf{k}}) - k_y \mathcal{E}_y(\hat{\mathbf{k}})}{\sqrt{k^2 - |\hat{\mathbf{k}}|^2}} e^{j\mathbf{k}^T \mathbf{r}} dk_x dk_y \quad .\tag{2.7}$$

Equation 2.7 is also given in the literature and used for aperture antenna problems [70, 71, 73] and for vector beam solutions to Maxwell's equations [77–79]. Please note that, for the special case  $|\hat{\mathbf{k}}|^2 = k^2$ , we assume that  $\mathcal{E}_x(\hat{\mathbf{k}})$ ,  $\mathcal{E}_y(\hat{\mathbf{k}})$  and  $\mathcal{E}_z(\hat{\mathbf{k}})$  are 0.

The electric field given in Equation 2.1 can also be decomposed into propagating and evanescent components as

$$\mathbf{E}(\mathbf{r}) = \mathbf{E}_P(\mathbf{r}) + \mathbf{E}_{P'}(\mathbf{r}) \quad ,\tag{2.8}$$

where the subscripts  $P$  and  $P'$  denote the propagating and evanescent components, respectively. These components are

$$\mathbf{E}_P(\mathbf{r}) = \frac{1}{4\pi^2} \int_{-\infty}^{\infty} \mathcal{E}(\hat{\mathbf{k}}) \operatorname{rect}\left(\frac{|\hat{\mathbf{k}}|}{k}\right) e^{j\mathbf{k}^T \mathbf{r}} d\hat{\mathbf{k}} \quad , \quad (2.9)$$

$$\mathbf{E}_{P'}(\mathbf{r}) = \frac{1}{4\pi^2} \int_{-\infty}^{\infty} \mathcal{E}(\hat{\mathbf{k}}) \left[1 - \operatorname{rect}\left(\frac{|\hat{\mathbf{k}}|}{k}\right)\right] e^{j\mathbf{k}^T \mathbf{r}} d\hat{\mathbf{k}} \quad , \quad (2.10)$$

where

$$\operatorname{rect}(\chi) = \begin{cases} 1 & \text{if } \chi < 1 \\ 0 & \text{if } \chi > 1 \end{cases} \quad (2.11)$$

for  $0 \leq \chi < \infty$ . As it will be shown below, decomposing the field into the propagating and evanescent components as in Equation 2.8 simplifies the computation of the  $z$  component if the field is known to be propagating or evanescent.

We define the filter transfer functions  $\mathcal{G}_x(\hat{\mathbf{k}})$  and  $\mathcal{G}_y(\hat{\mathbf{k}})$  which multiply  $\mathcal{E}_x(\hat{\mathbf{k}})$  and  $\mathcal{E}_y(\hat{\mathbf{k}})$  in Equation 2.7, respectively, as

$$\mathcal{G}_x(\hat{\mathbf{k}}) = -\frac{k_x}{\sqrt{k^2 - |\hat{\mathbf{k}}|^2}} \quad \text{if } |\hat{\mathbf{k}}| \neq k \quad , \quad (2.12)$$

$$\mathcal{G}_y(\hat{\mathbf{k}}) = -\frac{k_y}{\sqrt{k^2 - |\hat{\mathbf{k}}|^2}} \quad \text{if } |\hat{\mathbf{k}}| \neq k \quad . \quad (2.13)$$

In the polar coordinates, these filters are

$$\mathcal{G}_x^{\text{polar}}(\kappa, \phi) = -\frac{\kappa \cos \phi}{\sqrt{k^2 - \kappa^2}} \quad \text{if } \kappa \neq k \quad , \quad (2.14)$$

$$\mathcal{G}_y^{\text{polar}}(\kappa, \phi) = -\frac{\kappa \sin \phi}{\sqrt{k^2 - \kappa^2}} \quad \text{if } \kappa \neq k \quad , \quad (2.15)$$

where  $k_x = \kappa \cos \phi$ ,  $k_y = \kappa \sin \phi$  for  $0 \leq \kappa < \infty$  and  $0 \leq \phi < 2\pi$ .

In order to find the 2D IFT of the filters, we introduce an auxiliary filter defined as

$$\mathcal{G}_0(\hat{\mathbf{k}}) = -\frac{1}{\sqrt{k^2 - |\hat{\mathbf{k}}|^2}} \quad \text{if } |\hat{\mathbf{k}}| \neq k \quad . \quad (2.16)$$

Due to the circular symmetry, the 2D IFT of  $\mathcal{G}_0(\hat{\mathbf{k}})$  becomes the inverse Hankel transform of order zero and can be written as [80],

$$\mathfrak{F}_{2D}^{-1}\{\mathcal{G}_0(\hat{\mathbf{k}})\} = g_0(\hat{\mathbf{r}}) = \frac{j}{2\pi} \frac{e^{jk|\hat{\mathbf{r}}|}}{|\hat{\mathbf{r}}|} \quad , \quad (2.17)$$

where  $\mathfrak{F}_{2D}^{-1}\{\cdot\}$  indicates the 2D IFT from  $\hat{\mathbf{k}}$  domain to  $\hat{\mathbf{r}}$  domain. Then,

$$\begin{aligned} g_x(\hat{\mathbf{r}}) &= \mathfrak{F}_{2D}^{-1}\{\mathcal{G}_x(\hat{\mathbf{k}})\} = \mathfrak{F}_{2D}^{-1}\{k_x \mathcal{G}_0(\hat{\mathbf{k}})\} = \\ &= \frac{1}{j} \frac{\partial g_0(\hat{\mathbf{r}})}{\partial x} = \frac{1}{2\pi} \frac{x}{|\hat{\mathbf{r}}|^2} e^{jk|\hat{\mathbf{r}}|} \left( jk - \frac{1}{|\hat{\mathbf{r}}|} \right) \quad . \end{aligned} \quad (2.18)$$

Similarly,

$$\begin{aligned} g_y(\hat{\mathbf{r}}) &= \mathfrak{F}_{2D}^{-1}\{\mathcal{G}_y(\hat{\mathbf{k}})\} = \mathfrak{F}_{2D}^{-1}\{k_y \mathcal{G}_0(\hat{\mathbf{k}})\} = \\ &= \frac{1}{j} \frac{\partial g_0(\hat{\mathbf{r}})}{\partial y} = \frac{1}{2\pi} \frac{y}{|\hat{\mathbf{r}}|^2} e^{jk|\hat{\mathbf{r}}|} \left( jk - \frac{1}{|\hat{\mathbf{r}}|} \right) \quad . \end{aligned} \quad (2.19)$$

In the polar coordinates, the impulse responses of the filters are

$$g_x^{polar}(\rho, \theta) = \frac{\cos \theta}{2\pi} \frac{e^{jk\rho}}{\rho} \left( jk - \frac{1}{\rho} \right) \quad , \quad (2.20)$$

$$g_y^{polar}(\rho, \theta) = \frac{\sin \theta}{2\pi} \frac{e^{jk\rho}}{\rho} \left( jk - \frac{1}{\rho} \right) \quad , \quad (2.21)$$

where  $x = \rho \cos \theta$  and  $y = \rho \sin \theta$  for  $0 \leq \rho < \infty$  and  $0 \leq \theta < 2\pi$ .

Please note that, the impulse responses in Equations 2.20 and 2.21 that we derive using the properties of the Fourier transform were also obtained by using the Green's function of the free space propagation in [6]. In this respect, this equivalence can be viewed as similar to the relation between the transfer function and the Green's function of the free space propagation that is developed by Sherman in [11] and by Bouwkamp in [5].

If the field is composed only of propagating waves, i.e.  $\mathbf{E}_{P'}(\mathbf{r}) = 0$ , then the transfer functions of the filters can be written as

$$\mathcal{G}_{x,p}(\hat{\mathbf{k}}) = \mathcal{G}_x(\hat{\mathbf{k}}) \text{rect}\left(\frac{|\hat{\mathbf{k}}|}{k}\right) , \quad (2.22)$$

$$\mathcal{G}_{y,p}(\hat{\mathbf{k}}) = \mathcal{G}_y(\hat{\mathbf{k}}) \text{rect}\left(\frac{|\hat{\mathbf{k}}|}{k}\right) , \quad (2.23)$$

and in polar coordinates as

$$\mathcal{G}_{x,p}^{polar}(\kappa, \phi) = \mathcal{G}_x^{polar}(\kappa, \phi) \text{rect}\left(\frac{\kappa}{k}\right) , \quad (2.24)$$

$$\mathcal{G}_{y,p}^{polar}(\kappa, \phi) = \mathcal{G}_y^{polar}(\kappa, \phi) \text{rect}\left(\frac{\kappa}{k}\right) . \quad (2.25)$$

The auxiliary filter for this case,  $\mathcal{G}_{0,p}(\hat{\mathbf{k}})$ , then becomes  $\mathcal{G}_0(\hat{\mathbf{k}}) \text{rect}\left(\frac{|\hat{\mathbf{k}}|}{k}\right)$  and its 2D IFT is [9, 80]

$$\mathfrak{F}_{2D}^{-1}\left\{\mathcal{G}_{0,p}(\hat{\mathbf{k}})\right\} = g_{0,p}(\hat{\mathbf{r}}) = -\frac{\sin(k|\hat{\mathbf{r}}|)}{2\pi|\hat{\mathbf{r}}|} . \quad (2.26)$$

Again using the derivative property of the FT, the impulse responses of the filters are obtained as

$$g_{x,p}(\hat{\mathbf{r}}) = \frac{j}{2\pi} \frac{x}{|\hat{\mathbf{r}}|^2} \left[ k \cos(k|\hat{\mathbf{r}}|) - \frac{1}{|\hat{\mathbf{r}}|} \sin(k|\hat{\mathbf{r}}|) \right] , \quad (2.27)$$

$$g_{y,p}(\hat{\mathbf{r}}) = \frac{j}{2\pi} \frac{y}{|\hat{\mathbf{r}}|^2} \left[ k \cos(k|\hat{\mathbf{r}}|) - \frac{1}{|\hat{\mathbf{r}}|} \sin(k|\hat{\mathbf{r}}|) \right] . \quad (2.28)$$

In the polar coordinates Equations 2.27 and 2.28 become

$$g_{x,p}^{polar}(\rho, \theta) = \frac{j}{2\pi} \frac{\cos\theta}{\rho} \left[ k \cos(k\rho) - \frac{1}{\rho} \sin(k\rho) \right] , \quad (2.29)$$

$$g_{y,p}^{polar}(\rho, \theta) = \frac{j}{2\pi} \frac{\sin\theta}{\rho} \left[ k \cos(k\rho) - \frac{1}{\rho} \sin(k\rho) \right] . \quad (2.30)$$

Please note that, since  $k_z$  is always real for propagating waves, the impulse response given for the propagating fields in Equation 2.26,  $g_{0,p}(\hat{\mathbf{r}})$ , is the real part of the impulse response given for a general field in Equation 2.17,  $g_0(\hat{\mathbf{r}})$ . In order to show this, we first define the filter corresponding to evanescent components as

$$\mathcal{G}_{0,p'}(\hat{\mathbf{k}}) = \mathcal{G}_0(\hat{\mathbf{k}}) \left[ 1 - \text{rect} \left( \frac{|\hat{\mathbf{k}}|}{k} \right) \right] . \quad (2.31)$$

Then,

$$\begin{aligned} \mathfrak{F}_{2D}^{-1} \left\{ \mathcal{G}_0(\hat{\mathbf{k}}) \right\} &= \mathfrak{F}_{2D}^{-1} \left\{ \mathcal{G}_{0,p}(\hat{\mathbf{k}}) + \mathcal{G}_{0,p'}(\hat{\mathbf{k}}) \right\} \\ &= \mathfrak{F}_{2D}^{-1} \left\{ \mathcal{G}_{0,p}(\hat{\mathbf{k}}) \right\} + \mathfrak{F}_{2D}^{-1} \left\{ \mathcal{G}_{0,p'}(\hat{\mathbf{k}}) \right\} \\ &= g_{0,p}(\hat{\mathbf{r}}) + g_{0,p'}(\hat{\mathbf{r}}) \\ &= g_0(\hat{\mathbf{r}}) . \end{aligned} \quad (2.32)$$

$\mathcal{G}_{0,p}(\hat{\mathbf{k}})$  is a real valued and even function of  $k_x$  and  $k_y$ . From the symmetry property of the FT, the 2D IFT of  $\mathcal{G}_{0,p}(\hat{\mathbf{k}})$  becomes an even and real function of  $x$  and  $y$ . Similarly  $\mathcal{G}_{0,p'}(\hat{\mathbf{k}})$  is a purely imaginary and even function and hence, its 2D IFT also becomes even and purely imaginary. Therefore,  $g_{0,p}(\hat{\mathbf{r}}) = \text{Re}\{g_0(\hat{\mathbf{r}})\}$ , where the  $\text{Re}\{\cdot\}$  operator gives the real part of its input. Then, since the derivative of a real valued function remains real valued,

$$\frac{1}{j} \frac{\partial g_{0,p}(\hat{\mathbf{r}})}{\partial x} = \frac{1}{j} \frac{\partial \text{Re}\{g_0(\hat{\mathbf{r}})\}}{\partial x} = j \text{Im} \left\{ \frac{1}{j} \frac{\partial g_0(\hat{\mathbf{r}})}{\partial x} \right\} , \quad (2.33)$$

where the  $\text{Im}\{\cdot\}$  operator gives the imaginary part of its input. So,  $g_{x,p}(\hat{\mathbf{r}}) = j \text{Im}\{g_x(\hat{\mathbf{r}})\}$ , and similarly  $g_{y,p}(\hat{\mathbf{r}}) = j \text{Im}\{g_y(\hat{\mathbf{r}})\}$ .

If the field does not have any propagating components, and therefore, is composed of only evanescent waves as implied by the constraints, i.e., if  $k_z$  is always purely imaginary, then by following a similar approach, it can be shown that

$$g_{x,p'}(\hat{\mathbf{r}}) = \text{Re}\{g_x(\hat{\mathbf{r}})\} \text{ and } g_{y,p'}(\hat{\mathbf{r}}) = \text{Re}\{g_y(\hat{\mathbf{r}})\} , \quad (2.34)$$

where  $g_{x,p'}(\hat{\mathbf{r}})$  and  $g_{y,p'}(\hat{\mathbf{r}})$  are the filter impulse responses for those fields which involve only those evanescent waves.

Although the impulse responses corresponding to the arbitrary monochromatic fields are complex valued, as given in Equations 2.18 and 2.19, if the field is known to be propagating or evanescent, then the impulse responses of the filters become purely imaginary or real, respectively. Therefore, such a constraint reduces the computational complexity in the computation of the  $z$  component from the  $x$  and  $y$  components.

The block diagram of the computation of  $E_z(\hat{\mathbf{r}}, 0)$  is shown in Figure 2.1. In the figure, propagation in free space is also included as a block. A finite portion of the imaginary part of the impulse response of the filters  $g_{x,p}(\hat{\mathbf{r}})$  and  $g_{y,p}(\hat{\mathbf{r}})$  are shown in Figure 2.2.

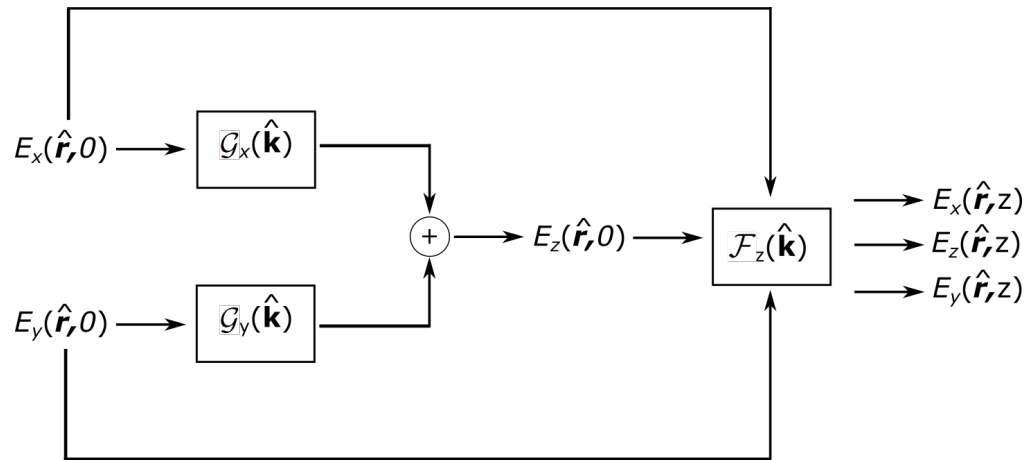
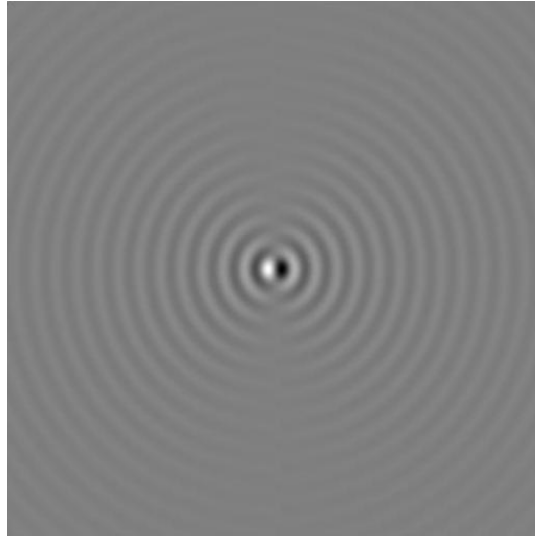
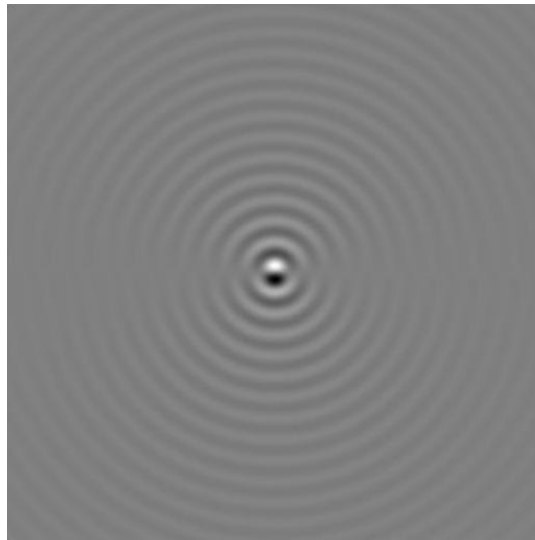


Figure 2.1: The computation steps of the  $z$  component of the electric field, including free space propagation, are shown as a block diagram. (©2016 Taylor & Francis. Reprinted with permission. Published in [74].)



(a)  $g_{x,p}(\hat{\mathbf{r}})$



(b)  $g_{y,p}(\hat{\mathbf{r}})$

Figure 2.2: For the propagating field case, a finite portion of the imaginary parts of the impulse responses of the filters are shown.  $(x, y) = (0, 0)$  corresponds to the center of the images; the horizontal axis is  $x$  and the vertical axis is  $y$ . (©2016 Taylor & Francis. Reprinted with permission. Published in [74].)

## 2.1.2 Properties of the Filters

In this section, we describe the frequency selectivity characteristics of the filters defined in Section 2.1.1 for the propagating case. By inspection, it can be seen that the 2D filters  $\mathcal{G}_{\{x,y\},p}(\hat{\mathbf{k}})$  are bandpass filters with a circular discontinuity at those values of  $k_x$  and  $k_y$  which satisfy  $|\hat{\mathbf{k}}| = k$ . However, within their passbands, they show highpass characteristics.

Firstly, for the sake of illustration, we plot the radial part of  $\mathcal{G}_{\{x,y\},p}^{polar}(\kappa, \phi)$ , which is given by  $\frac{\kappa}{\sqrt{k^2 - \kappa^2}} \text{rect}\left(\frac{\kappa}{k}\right)$  from Equations 2.24 and 2.25, with the normalized frequency variable  $v = \kappa/k$ , in Figure 2.3.

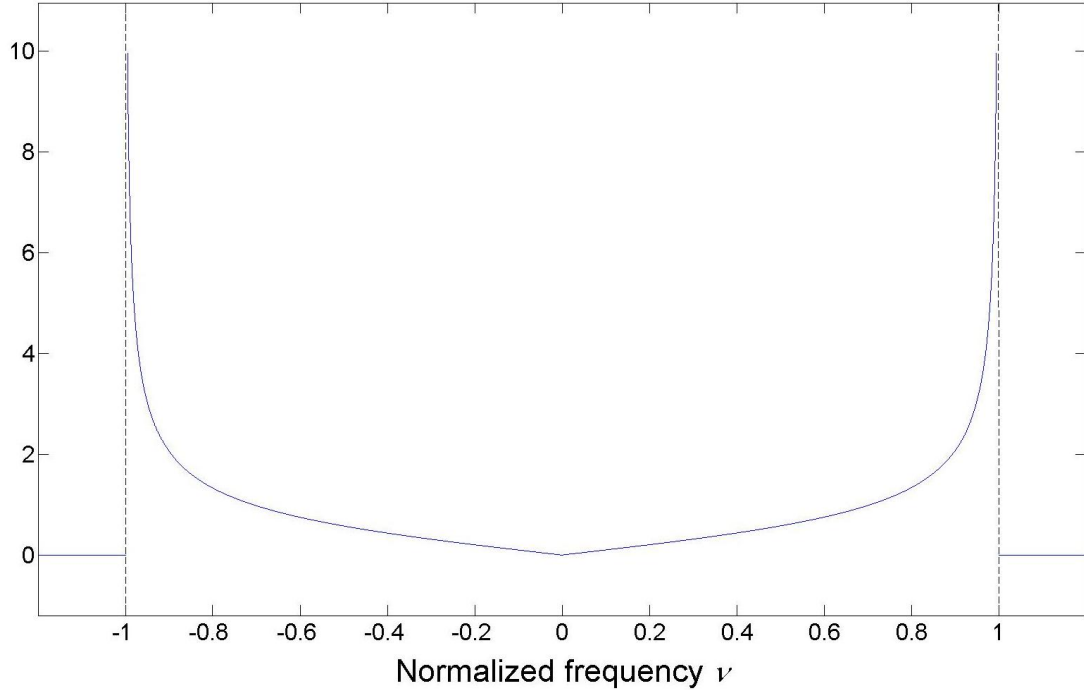


Figure 2.3: The radial variation of  $\mathcal{G}_{\{x,y\},p}^{polar}(\kappa, \phi)$  with the normalized frequency variable  $v = \kappa/k$  is shown. The frequency variable  $v$  is the normalized version of  $\kappa$  by  $k$ . (©2016 Taylor & Francis. Reprinted with permission. Published in [74].)

As it can be seen from Figure 2.3, the magnitude response of the filters increases rather slowly from the center in both positive and negative directions until  $|\nu| \approx 0.75$ . However, beyond these points the magnitude response of the filters increases sharply, and as  $\nu$  goes to  $-1$  from the right and  $+1$  from the left, the filter magnitude tends to infinity.

In Figure 2.4, the 2D magnitude response of both filters with the normalized frequency variables  $v_x$  and  $v_y$  are shown as 3D surface plots.

The characteristics of the filters observed in Figures 2.3 and 2.4 also help to show that a scalar wave field can be used as an approximation to the vector wave field under some conditions. For example, it is clear that if the field is restricted only to those small angles around zero (the paraxial approximation), then the magnitude of the filters will be small enough to justify neglected  $E_z$  component. Under this circumstance, the scalar field we are working with may be interpreted as either  $E_x$  or  $E_y$ , or any linear combination of those. Other valid approximations are also possible. For example, any narrowband of angles around a given direction will also yield an accurate enough scalar approximation together with a constant  $E_z$  component. In Section 2.1.3 we discuss this topic in more detail.

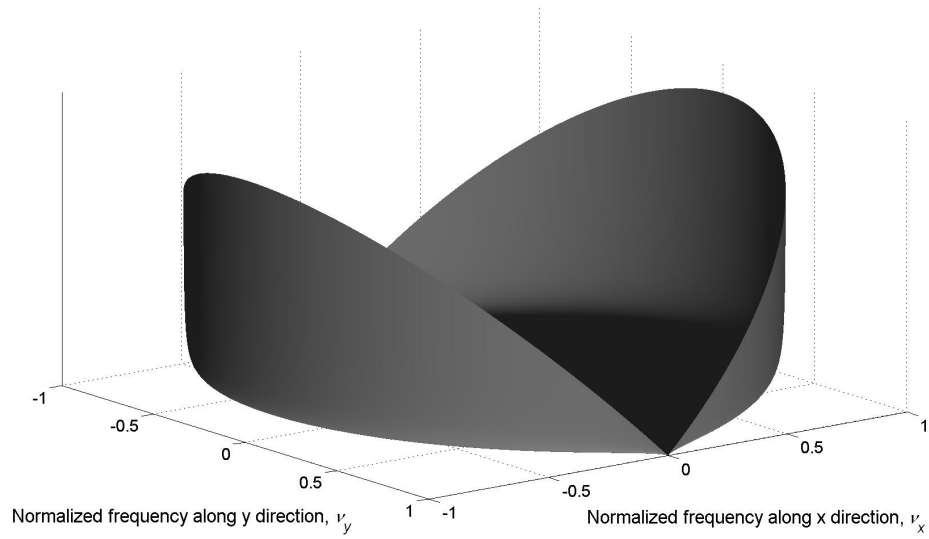
As an additional property, in Appendix A we prove that the integrals

$$\frac{1}{4\pi^2} \int_{-\infty}^{\infty} \left| \mathcal{G}_{x,p}(\hat{\mathbf{k}}) \right|^2 d\hat{\mathbf{k}} \quad (2.35)$$

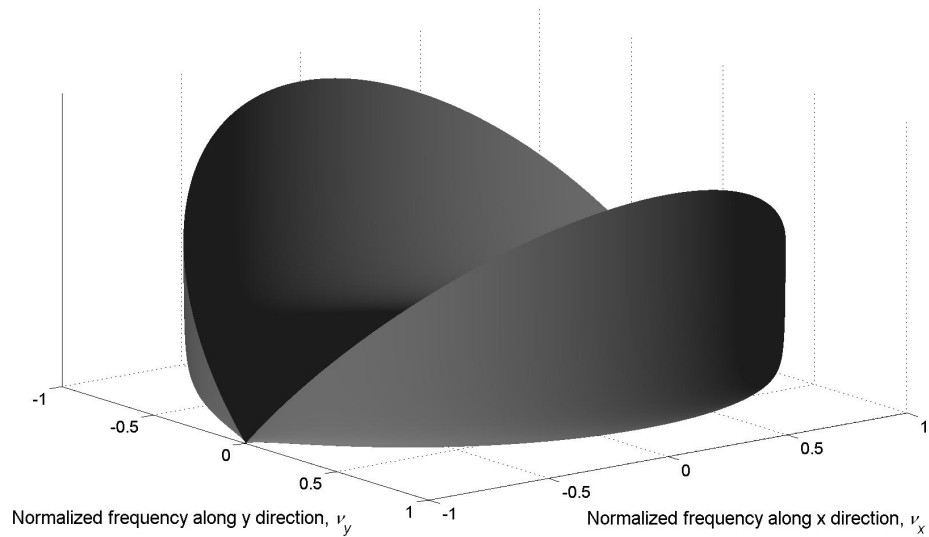
and

$$\frac{1}{4\pi^2} \int_{-\infty}^{\infty} \left| \mathcal{G}_{y,p}(\hat{\mathbf{k}}) \right|^2 d\hat{\mathbf{k}} \quad (2.36)$$

diverge. However, divergent integrals of the magnitude square of the transfer functions does not necessarily mean that the monochromatic field possesses infinite energy.



$$(a) \left| \mathcal{G}_{x,p}(\hat{\mathbf{k}}) \right|$$



$$(b) \left| \mathcal{G}_{y,p}(\hat{\mathbf{k}}) \right|$$

Figure 2.4: The magnitude response of the filters are shown as 3D surface plots, where  $v_x$  and  $v_y$  are the normalized frequency variables:  $v_x = k_x/k$  and  $v_y = k_y/k$ . (©2016 Taylor & Francis. Reprinted with permission. Published in [74].)

### 2.1.3 Vector versus Scalar Modeling of Optical Diffraction

In order to reduce the computational cost, vector fields may be mapped to scalar fields under some restrictions. In the following paragraphs, we describe such mappings found in the literature that we are aware of.

The most common approach is to solve for a scalar field and then map this scalar field to one of the transverse components of the vector electromagnetic field [4, 65, 81] and assume the longitudinal component to be zero. An immediate extension is to map the scalar field to the complex amplitude of the electric field along a fixed direction within the  $(x, y)$  plane; such a field satisfies the same Helmholtz's equation [4]. Such a mapping can be achieved as

$$\begin{bmatrix} E_x(\mathbf{r}) \\ E_y(\mathbf{r}) \end{bmatrix} = \frac{1}{\sqrt{1 + |C|^2}} \begin{bmatrix} S(\mathbf{r}) \\ CS(\mathbf{r}) \end{bmatrix}, \quad (2.37)$$

when the relation,  $E_y(\mathbf{r})/E_x(\mathbf{r}) = C \in \mathbb{C}$  holds for all  $\mathbf{r}$ . Here, the multiplier  $(1 + |C|^2)^{-1/2}$  is inserted to have an exact match between the scalar field and electric field intensity. When dealing with free space propagation, if the main propagation direction of the light beam is chosen to lie within a small cone around the  $z$  axis and the primary goal is to compute the intensity of the wave, then such a map from a scalar field to a vector electromagnetic field gives the intensity value with negligible error. If the paraxial condition is satisfied, the main contribution to the intensity of the vector wave comes from the dominant component which is orthogonal to the propagation direction. In [64], for example, the validity of such a scalar approximation was showed for a paraxial imaging setup. Since  $k_x$  and  $k_y$  for each plane wave component are small in the paraxial case, by the virtue of the highpass characteristics within the passbands of the filters  $\mathcal{G}_{\{x,y\},p}(\hat{\mathbf{k}})$ , the  $z$  component becomes small and its contribution to the intensity becomes negligible. Otherwise, if  $k_x$  or  $k_y$  is large, then the  $z$  component cannot be neglected and the scalar approximation becomes erroneous during the intensity computation.

Another approach is to map the complex amplitude of the scalar plane wave to a vector plane wave whose intensity is proportional to the intensity of the scalar wave [7, 12, 82]. With this approach, the intensity of a single vector plane wave

and the corresponding scalar plane wave can be exactly matched at each point in space as it is constant everywhere. Moreover, if a vector plane wave is linearly polarized, that wave can be described exactly by the corresponding scalar plane wave in terms of the magnitude and phase even if the wave is not paraxial. For example, for a given  $(k_x, k_z)$  pair, the vector wave  $(\hat{a}_x E_x + \hat{a}_z E_z) e^{j(k_x x + k_z z)}$  and the scalar wave  $\sqrt{|E_x|^2 + |E_z|^2} e^{j(k_x x + k_z z + \phi)}$ , give the same intensity value up to a constant multiplier at each point in space. Here  $\hat{a}_x$  and  $\hat{a}_z$  are the unit vectors pointing along the  $x$  and  $z$  directions,  $E_z = E_x H_{x,p}(k_x, k_y)$  is the  $z$  component of the field,  $|E_x|$  and  $|E_z|$  are the respective magnitudes, and  $\phi$  denotes the angular component of the complex number  $E_x$  (and hence describes the phase of the linearly polarized wave). However, if we cannot make the narrowband assumption, plane waves propagating along different directions will interfere, and consequently the total intensity of the field computed by the scalar theory will not be negligible. In other words, if the vector plane wave amplitude is mapped to the corresponding scalar plane wave amplitude and if the  $z$  component is large, then the computed intensity in the scalar domain highly deviates from the actual intensity computed according to the vector theory.

To sum up, the above two mappings from scalar-to-vector waves are valid for narrowband fields. That is, if the main propagation axis of the light beam is chosen as the  $z$  axis and if  $k_x$  and  $k_y$  are small, then the  $z$  component, which is the cause of the error in the scalar approximations, also becomes small. This narrowband requirement for the scalar field, for instance, imposes that the angle of the reference beam cannot deviate too much from the object beam in off-axis holography. In this respect, the ratio of the energy of the  $z$  component to the energy of the total electric field at the  $z = 0$  plane can be seen as an error measure of the scalar approximation. This measure can be formulated as

$$\frac{\int_{-\infty}^{\infty} \left| \mathcal{G}_{x,p}(\hat{\mathbf{k}}) \mathcal{E}_x(\hat{\mathbf{k}}) + \mathcal{G}_{y,p}(\hat{\mathbf{k}}) \mathcal{E}_y(\hat{\mathbf{k}}) \right|^2 d\hat{\mathbf{k}}}{\int_{-\infty}^{\infty} \left( \left| \mathcal{E}_x(\hat{\mathbf{k}}) \right|^2 + \left| \mathcal{E}_y(\hat{\mathbf{k}}) \right|^2 + \left| \mathcal{G}_{x,p}(\hat{\mathbf{k}}) \mathcal{E}_x(\hat{\mathbf{k}}) + \mathcal{G}_{y,p}(\hat{\mathbf{k}}) \mathcal{E}_y(\hat{\mathbf{k}}) \right|^2 \right) d\hat{\mathbf{k}}} \quad (2.38)$$

Since the total energy of the field at the transverse plane is preserved in the free space propagation, the error measure given in Equation 2.38 does not change at

different  $z = d$  planes.

A detailed treatment of the scalar representations of different paraxial and nonparaxial beam solutions of Maxwell's equations together with further references is given in [81]. The validity of the scalar and paraxial approximations for Gaussian beam are considered in [77, 83, 84].

Another, somewhat different approach is to consider the scalar field to be a physical quantity distinct from the electric or magnetic field components. For example, in [85–87], a scalar representation is developed by assuming the two independent components of the real magnetic vector potential as the real and imaginary parts of the complex scalar field. Then, the analytical form of the corresponding energy and momentum densities are computed based on the developed scalar representation.

## 2.1.4 Digital Simulator

In this section, we present a digital simulator to compute the longitudinal component of the electric field from its transversal components all at  $z = 0$  plane. So, there is no propagation involved in the simulator.

First of all, since the field components are assumed to be propagating, the spatial frequency content of the transversal field components are confined in a circular band whose radius is smaller than the wave number. The energy of the impulse response functions of the filters is found in Appendix A to be

$$-\frac{\kappa'^2}{8\pi} - \frac{k^2}{8\pi} \ln \left[ 1 - \left( \frac{\kappa'}{k} \right)^2 \right] , \quad (2.39)$$

where  $\kappa' < k$  is the radius of the imposed circular passband of the filters that can be taken as the larger one of the radius' of the passbands of the  $x$  and  $y$  components of the field. (Here we refer to the integral  $\int_{-\infty}^{\infty} |f(\xi)|^2 d\xi$  as the total energy of function  $f(\xi)$ , as commonly used in signal processing. This energy may or may not have any relation to the physical energy in different settings.)

Therefore, although the resulting bandwidth of the related signals is smaller than  $k$ , in order to satisfy the Shannon-Nyquist criteria under regular rectangular sampling scheme, we use  $\pi/k$  as the sampling period, since the passband of the field components may vary, but cannot be larger than or equal to  $k$ .

We form the  $x$  component of the discrete input field  $\hat{E}_x[n, m, 0]$ , from the continuous field  $E_x(x, y, 0)$  with the integer variables  $n$  and  $m$  as

$$\hat{E}_x[n, m, 0] = \begin{cases} E_x(nX_s, mY_s, 0) & \text{if } 0 \leq n \leq N-1, 0 \leq m \leq M-1 \\ 0 & \text{otherwise} \end{cases}, \quad (2.40)$$

where the discrete input field size is assumed to be  $M \times N$ . Then we convert this finite size input to the periodically replicated version as

$$\tilde{E}_x[n, m, 0] = \hat{E}_x[n_{\text{mod}N}, m_{\text{mod}M}] \quad . \quad (2.41)$$

Therefore, the finite size discrete input field is one period of the infinite size discrete periodic input field.  $\tilde{E}_x[n, m, 0]$  has only finite number of frequency components and can be written as [67],

$$\tilde{E}_x[n, m, 0] = \frac{1}{NM} \sum_{q=0}^{M-1} \sum_{p=0}^{N-1} \hat{\mathcal{E}}_x[p, q] e^{j2\pi(\frac{qm}{M} + \frac{pn}{N})} \quad . \quad (2.42)$$

So,

$$\hat{\mathcal{E}}_x[p, q] = DFT_{M \times N} \left\{ \hat{E}_x[n, m, 0] \right\} \quad , \quad (2.43)$$

where  $DFT_{M \times N} \{ \cdot \}$  stands for the 2D, size  $M \times N$  discrete Fourier transform (DFT) [67].

The discrete filter corresponding to the  $x$  component in the DFT domain,  $\hat{\mathcal{G}}_{x,p}[p, q]$ , is generated from the transfer function of the filter defined in Equation 2.22 as

$$\hat{\mathcal{G}}_{x,p}[p, q] \Big|_{\substack{q=\hat{q}_{\text{mod}M} \\ p=\hat{p}_{\text{mod}N}}} = \mathcal{G}_{x,p} \left( \frac{2k}{N} \hat{p}, \frac{2k}{M} \hat{q} \right) \quad , \quad (2.44)$$

where  $\hat{q} \in [-\lceil \frac{M-1}{2} \rceil, \lceil \frac{M}{2} - 1 \rceil]$ ,  $\hat{p} \in [-\lceil \frac{N-1}{2} \rceil, \lceil \frac{N}{2} - 1 \rceil]$ ,  $\lceil \cdot \rceil$  is the ceiling operator which rounds a decimal number to the nearest larger integer and  $k = 2\pi/\lambda$ ,

as usual. The generation procedure of the  $y$  component and the corresponding filter in the DFT domain,  $\hat{\mathcal{E}}_y [p, q]$  and  $\hat{\mathcal{G}}_{y,p} [p, q]$ , is the same as the procedure described above.

After computing the 2D DFT coefficients of the field components and the transfer functions of the filters, we compute the discrete system output as

$$\hat{E}_z [n, m, 0] = IDFT_{M \times N} \left\{ \hat{\mathcal{E}}_x [p, q] \hat{\mathcal{G}}_{x,p} [p, q] + \hat{\mathcal{E}}_y [p, q] \hat{\mathcal{G}}_{y,p} [p, q] \right\} \quad (2.45)$$

$$= IDFT_{M \times N} \left\{ \hat{\mathcal{E}}_z [p, q] \right\} \quad , \quad (2.46)$$

where  $IDFT_{M \times N} \{ \cdot \}$  stands for the 2D, size  $M \times N$  inverse DFT [67]. Similar to the input field components, the finite size discrete output field,  $\hat{E}_z [n, m, 0]$ , can be assumed as the one period of the periodic infinite size discrete field  $\tilde{E}_z [n, m, 0]$ .

As a result, if the continuous input fields include only the spatial frequency components  $2k\hat{p}/N$  and  $2k\hat{q}/M$  for  $\hat{p} \in \left[ -\left\lceil \frac{N-1}{2} \right\rceil, \left\lceil \frac{N}{2} - 1 \right\rceil \right]$  and  $\hat{q} \in \left[ -\left\lceil \frac{M-1}{2} \right\rceil, \left\lceil \frac{M}{2} - 1 \right\rceil \right]$  along  $k_x$  and  $k_y$  directions, respectively, then the simulator output gives the exact samples of the corresponding periodic continuous system output. Moreover, since the sampling period is chosen small enough, the corresponding output of the continuous system can be exactly found from the output of the discrete simulator. In other words, in an application which deals only with propagating waves, if  $M$  and  $N$  are chosen such that entire spatial frequency content of the periodic continuous field is covered in the discrete system, then the output of the digital simulator is useful to accurately simulate the continuous field.

We note that although here we use a regular rectangular sampling scheme, hexagonal sampling can also be used in an application which requires maximally efficient memory use and less computational complexity, since it is more efficient for signals with a circular band area [88].

We present a simulation where a test pattern that is commonly used to reveal the 2D frequency response of a 2D system is used as the input: The  $x$  and  $y$  components of the input are chosen to be the same as  $E_x [n, m, 0] = E_y [n, m, 0] = \cos \left[ \frac{\pi}{N} (m^2 + n^2) \right]$  as shown in Figure 2.5. Please note that for this 2D chirp signal

the parameter  $N$  specifies both the size and the rate of change of instantaneous frequency of the discrete field. When  $N = M$  and  $N$  is an even number, the 2D DFT of this function becomes  $N \sin \left[ \frac{\pi}{N} (q^2 + p^2) \right]$  [89]. As the instantaneous frequency of this chirp function linearly increases in the interval  $m \in [0, M/2]$  and  $n \in [0, N/2]$ , we expect to observe the approximate frequency and orientation selectivity characteristics of the system shown in Figure 2.1, when  $N$  is sufficiently large. In our simulation, we choose  $N = 16384 = 2^{14}$ . As seen from the output shown in Figure 2.6, the system frequency response is observed as expected for this test input.

Figure 2.6 reveals the orientation characteristics of the system. When  $k_x$  and  $k_y$  have the same sign, the filters add coherently and the response of the filters becomes large, and when they have different signs, the filters cancel each other out and the response of the system becomes weak. As a consequence of the discussion in Section 2.1.3, it can be said that, if the field components were, for example, this chirp signal, the conventional scalar theory would fail in the spatial positions in which the magnitude of the  $z$  component is high.

Please note that, the longitudinal component can also be zero whenever the equality  $\mathcal{E}_x(\hat{\mathbf{k}})k_x + \mathcal{E}_y(\hat{\mathbf{k}})k_y = 0$  is satisfied. This condition states that the polarization vector at a spatial frequency  $\hat{\mathbf{k}}$  lies on the  $x$ - $y$  plane. If the longitudinal component is desired to be identically zero, this can be achieved for any  $\hat{\mathbf{k}}$  by rotating the polarization vector around the propagation direction vector and keeping on the  $x$ - $y$  plane. In our simulation, the response of the system is small not only on the points near the low-frequencies, but also the frequencies in which the regions that correspond to  $k_x = -k_y$ . Therefore, in these spatial points, the error in the conventional scalar theory would be less, even if the field components include high-frequency components.

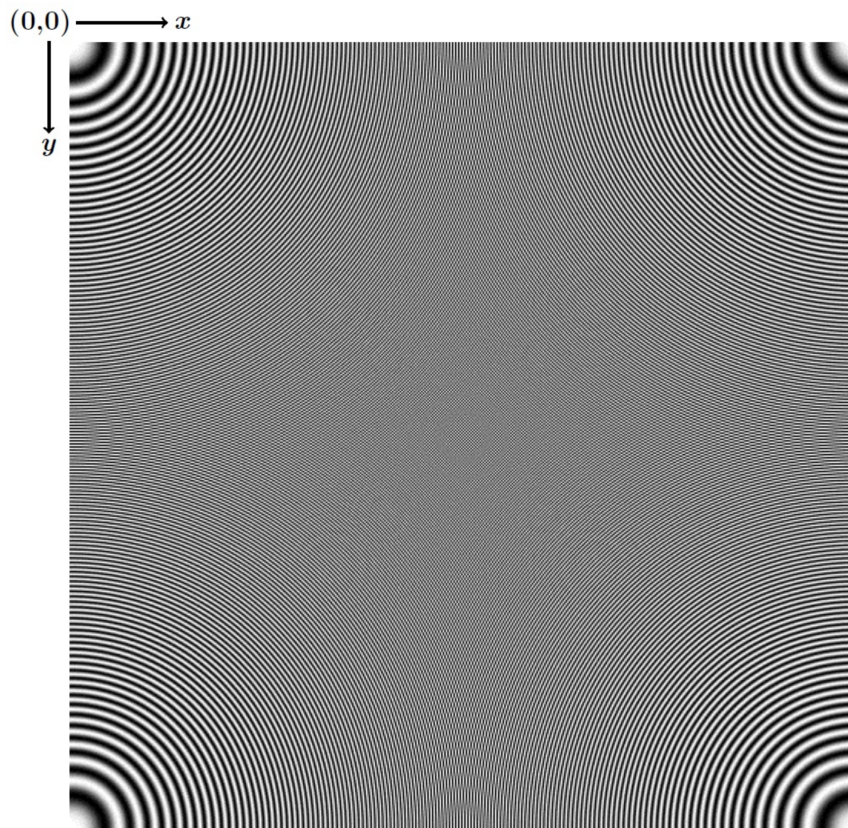


Figure 2.5: One period of the  $x$  and  $y$  components, which are the same, of the input field for the simulation is shown. (©2016 Taylor & Francis. Reprinted with permission. Published in [74].)

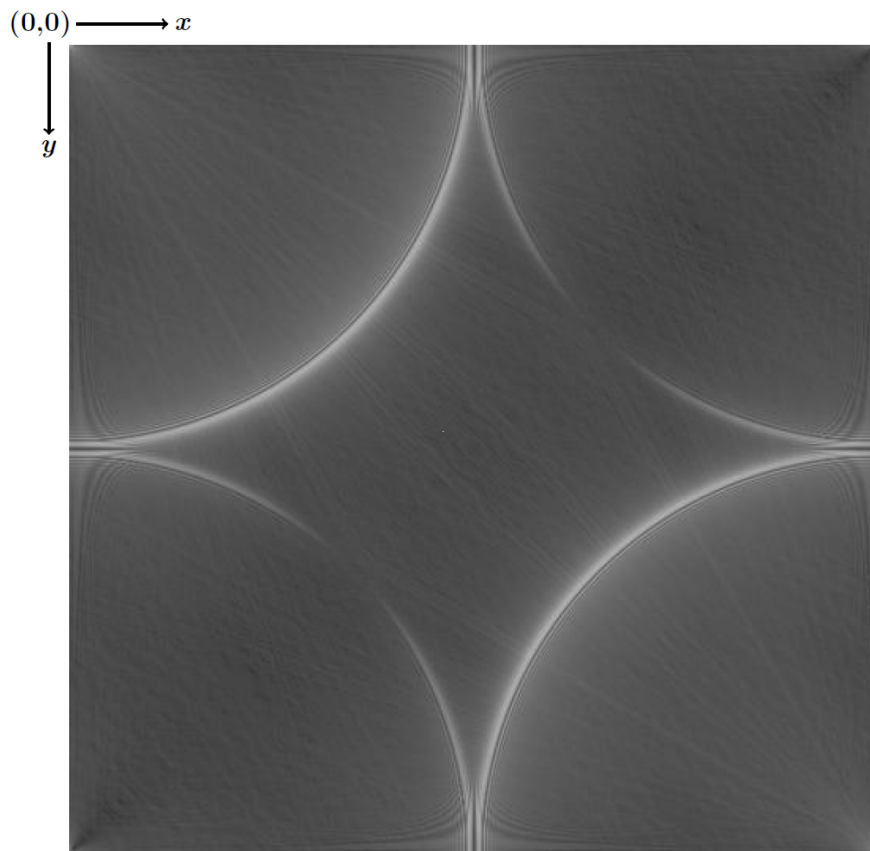


Figure 2.6: For  $N = 2^{14}$ , the magnitude of the  $z$  component corresponding to the input fields  $E_x[n, m, 0] = E_y[n, m, 0] = \cos\left[\frac{\pi}{N}(n^2 + m^2)\right]$  is shown at a logarithmic scale for better illustration. (©2016 Taylor & Francis. Reprinted with permission. Published in [74].)

This discrete simulator can be used when the continuous system inputs are such that the output cannot be calculated analytically. An evaluation of the amount of error, when the scalar approximation is used, is possible by using the provided simulator. In the following section, by using the discrete simulator described in this section and the error measure defined in Equation 2.38, we are going to discuss the effect of the display parameters on the validity of the use of the conventional scalar-to-vector field mapping, that is given by Equation 2.37

## 2.2 Effect of the Flat Panel and Pixelated 3D Display Parameters on the Use of the Conventional Scalar Approximation

In 3DTV applications, small pixel size for 3D displays is desired for large viewing angles [31]. However, in the previous section, we showed that, for the large propagation angles, the conventional scalar approximation, which is given by Equation 2.37, becomes invalid. As a result of this relation, a trade-off between the pixel size and the use of the conventional scalar approximation arises. In this section, which is mainly based on our publication [75], we present some simulations to discuss this trade-off.

### 2.2.1 Computation of the Longitudinal Component of Electric Field in Pixelated Flat Panel Displays

Here, we assume that the pixel configuration is regular rectangular and the phase and amplitude variations on the surface of the active region of a pixel are constant. At the  $z = 0$  plane, where the display is located, we write the continuous  $x$  and  $y$  components of the electric field generated by a single pixel as

$$\hat{E}_{\{x,y\}} [n, m] \text{rect}_2 \left( \frac{x - nP}{\Delta} \right) \text{rect}_2 \left( \frac{y - mP}{\Delta} \right) \quad , \quad (2.47)$$

where  $\hat{E}_{\{x,y\}}[n, m] \in \mathbb{C}$  denote either the  $x$  or  $y$  component of the electric field produced at the pixel whose location is determined by the integers  $m$  and  $n$ ,  $P \in \mathbb{R}^+$  is the pixel period,  $\Delta \in (0, P)$  is the width of the active region of the pixel. We define the  $\text{rect}_2(\cdot)$  function as

$$\text{rect}_2(u) = \begin{cases} 1 & \text{if } |u| \leq \frac{1}{2} \\ 0 & \text{otherwise} \end{cases}, \quad (2.48)$$

for  $u \in \mathbb{R}$ . The ratio  $A_r = \Delta/P$  is called the fill factor or the aperture ratio.

Then, the sum of the  $x$  and  $y$  components of the field produced at the display exit can be written as

$$E_{\{x,y\}}(\hat{\mathbf{r}}) = \sum_{m=0}^{M-1} \sum_{n=0}^{N-1} \hat{E}_{\{x,y\}}[n, m] \text{rect}_2\left(\frac{x - nP}{\Delta}\right) \text{rect}_2\left(\frac{y - mP}{\Delta}\right), \quad (2.49)$$

where  $N$  and  $M$  are the number of columns and rows of the display, respectively and so, the display size is  $M \times N$  pixels. We assume that the top-left corner pixel of the display corresponds to pixel index  $n = m = 0$ .

By using the 2D FT definition given by Equation 1.9, the 2D FTs of the  $x$  and  $y$  components at the  $z = 0$  plane that are given in Equation 2.49 become

$$\mathcal{E}_{\{x,y\}}(\hat{\mathbf{k}}) = \frac{4 \sin\left(\frac{k_x \Delta}{2}\right) \sin\left(\frac{k_y \Delta}{2}\right)}{k_x k_y} \mathcal{D}_{\{x,y\}}^{P,N,M}(\hat{\mathbf{k}}), \quad (2.50)$$

where

$$\mathcal{D}_{\{x,y\}}^{P,N,M}(\hat{\mathbf{k}}) = \sum_{m=0}^{M-1} \sum_{n=0}^{N-1} \hat{E}_{x,y}[n, m] e^{-jP(k_x n + k_y m)}. \quad (2.51)$$

Please note that, the only parameter of the display that does not have an effect on  $\mathcal{D}_{\{x,y\}}^{P,N,M}(\hat{\mathbf{k}})$  is the width of the active region,  $\Delta$ . It can be verified that  $\mathcal{D}_{\{x,y\}}^{P,N,M}(\hat{\mathbf{k}})$  are periodic by  $2\pi/P$  radians per unit length along both  $k_x$  and  $k_y$  directions. Moreover, since we assume that the field components are always zero when  $\hat{\mathbf{k}} = k$ ,  $\mathcal{D}_{\{x,y\}}^{P,N,M}(\hat{\mathbf{k}})$  becomes zero in this case, as well.

We assume that the pixelation process occurs in free space which is an isotropic medium. With this assumption and by using Equation 2.6, the 2D FT of the  $z$

component,  $\mathcal{E}_z(\hat{\mathbf{k}})$ , over the display surface can be found as

$$\mathcal{E}_z(\hat{\mathbf{k}}) = -\frac{\Delta^2}{k_z} \operatorname{sinc}\left(\frac{k_x \Delta}{2\pi}\right) \operatorname{sinc}\left(\frac{k_y \Delta}{2\pi}\right) \left(k_x \mathcal{D}_x^{P,N,M}(\hat{\mathbf{k}}) + k_y \mathcal{D}_y^{P,N,M}(\hat{\mathbf{k}})\right) \quad , \quad (2.52)$$

where

$$\operatorname{sinc}(u) = \frac{\sin(\pi u)}{\pi u} \quad (2.53)$$

for  $u \in \mathbb{R}$ .

The 2D FT of the  $z$  component of the electric field over all types of flat panel and pixelated display surfaces can be computed using Equation 2.52. Different configurations may impose some restrictions on the  $x$  and  $y$  components,  $\hat{E}_{\{x,y\}}[n, m]$ . For example, a phase only spatial light modulator (SLM) may require  $\hat{E}_x[n, m] = 0$  and  $|\hat{E}_y[n, m]| = c$  for all  $n$  and  $m$ , where  $c$  is a constant [61, 62]. Or a twisted nematic (TN) liquid crystal display (LCD) without analyzing polarizer requires  $|\hat{E}_x[n, m]|^2 + |\hat{E}_y[n, m]|^2 = c$ , where  $c$  is again constant [60]. Moreover, in a TN-LCD without the analyzing polarizer, as a direct consequence of the linear polarization, the phases of the  $x$  and  $y$  components at each pixel are either equal or  $\pi$  radians apart depending on the liquid crystal configuration.

## 2.2.2 Distribution of the Magnitude of the Longitudinal Component over the Frequency Plane

Here, we investigate the effect of the display parameters on the magnitude of the  $z$  component at different spatial frequencies. Since in some of the display applications, the field is assumed to be linearly polarized, we assume that the  $x$  component of the field is zero; so,  $\hat{E}_x[n, m] = 0$  for all  $m$  and  $n$ . In this case, the magnitude of  $\mathcal{E}_z(\hat{\mathbf{k}})$  given by Equation 2.52 becomes

$$\left|\mathcal{E}_z(\hat{\mathbf{k}})\right| = \left|\frac{2\Delta}{k_z} \operatorname{sinc}\left(\frac{k_x \Delta}{2\pi}\right) \operatorname{sinc}\left(\frac{k_y \Delta}{2\pi}\right) \mathcal{D}_y^{P,N,M}(\hat{\mathbf{k}})\right| \quad . \quad (2.54)$$

Firstly, it can be verified that, the rate of change of  $1/k_z$  with respect to  $k_x$  and  $k_y$  is much larger than the rate of change of  $\text{sinc}\left(\frac{k_x\Delta}{2\pi}\right)\sin\left(\frac{k_y\Delta}{2}\right)$  term in the high-frequency regions and much smaller in the low-frequency regions. Therefore, the resulting pattern of the  $z$  component due to Equation 2.54 is mainly caused by  $\mathcal{D}_y^{P,N,M}(\hat{\mathbf{k}})/k_z$  term in the high-frequency regions and  $\mathcal{D}_y^{P,N,M}(\hat{\mathbf{k}})\text{sinc}\left(\frac{k_x\Delta}{2\pi}\right)\sin\left(\frac{k_y\Delta}{2}\right)$  term in the low-frequency regions. Moreover, if  $P$  and  $\Delta$  values are comparable and the rate of change of  $\mathcal{D}_y^{P,N,M}(\hat{\mathbf{k}})$  is much smaller than the rate of change of  $\text{sinc}\left(\frac{k_x\Delta}{2\pi}\right)$ , due to the decaying characteristics of the sinc term, the periodic structure of  $\mathcal{D}_y^{P,N,M}(\hat{\mathbf{k}})$  along the  $k_x$  direction may not be seen in  $|\mathcal{E}_z(\hat{\mathbf{k}})|$  in the low-frequency regions. As opposed to this, if the rate of change of  $\mathcal{D}_y^{P,N,M}(\hat{\mathbf{k}})$  is much larger than the rate of change of the sinc term, then, the sinc pattern may not be seen in the low-frequency regions. The rate of change relation between  $\mathcal{D}_y^{P,N,M}(\hat{\mathbf{k}})$  and  $1/k_z$  is also similar in the high-frequency regions.

In the digital simulation, we assume that  $\hat{E}_y[n, m]$  is  $e^{j\phi[n, m]}$ , where  $\phi[n, m]$  is generated randomly for each  $m$  and  $n$  from an independent and uniform distribution between 0 and  $2\pi$  with 8-bit precision. The reason of this choice is to excite the system at all frequency locations, as the power spectral density of the generated  $\hat{E}_y[n, m]$  is flat. We choose  $M = 1080$  and  $N = 1920$ . In summary, our analysis covers a  $y$ -polarized display with a size of  $1080 \times 1920$  pixels in a phase-only operation. Using the generated  $\hat{E}_y[n, m]$  and assuming  $\lambda = 500 \text{ nm}$ , we compute  $|\mathcal{D}_y^{P,N,M}(\hat{\mathbf{k}})|$  in a  $512 \times 512$  frequency grid for  $k_x, k_y \in [-k, k]$  and for two pixel period values,  $P = 8 \text{ }\mu\text{m}$  and  $P = 20 \text{ }\mu\text{m}$ . Note that, since we assume that the pixel count is always the same, different pixel periods yield different display sizes in terms of width and height. Finally, we compute three different  $\mathcal{E}_z(\hat{\mathbf{k}})$ s using Equation 2.54 for the pairs  $(P, \Delta) = (8, 7)$ ,  $(8, 2)$  and  $(20, 2)$ , where all the units are in  $\mu\text{m}$ .

In Figures 2.7a, 2.7b and 2.7c, the computed  $|\mathcal{E}_z(\hat{\mathbf{k}})|$ 's are shown in log scale for better illustration. Since  $\mathcal{E}_z(\hat{\mathbf{k}})$  can be seen as the multiplication of  $\mathcal{E}_y(\hat{\mathbf{k}})$ , which has some higher order lobes due to Equation 2.50, and  $-k_y/k_z$ , these

higher order lobes along the vertical direction appears in  $\left| \mathcal{E}_z(\hat{\mathbf{k}}) \right|$  pattern, as well. However, although it is not shown here, it can be said that these higher order lobes are not so strong in  $\left| \mathcal{E}_y(\hat{\mathbf{k}}) \right|$  pattern. The width of these lobes along both the horizontal and vertical directions mainly depend on  $\Delta$  rather than  $P$ . Also the size of the lobes gets larger as  $\Delta$  gets smaller. In all three cases, in most of the high-frequency regions, the magnitude of the  $z$  component increases sharply by virtue of the  $1/k_z$  multiplier. Also, although it is not clear from the figures due to the log scale illustration, these high-frequency regions are the locations with the largest magnitude by far. Finally, if the display was  $x$ -polarized instead of a  $y$ -polarized one, then, the spectrums of the  $z$  component would be  $90^\circ$  rotated versions of the ones shown in Figure 2.7 since the  $x$  component would be multiplied by  $-k_x/k_z$  instead of  $-k_y/k_z$ .

In  $(P, \Delta) = (20, 2)$  case, since  $P$  is much larger than  $\Delta$ , it is possible to observe an approximate periodic structure in the low-frequency region along both  $k_x$  and  $k_y$  directions. In this respect, in Figures 2.8a and 2.8b, we present one-dimensional (1D) horizontal and vertical cross-sections of  $\mathcal{E}_z(\hat{\mathbf{k}})$  for  $k_y = k/8$  and  $k_x = 0$ , respectively. It can be seen from Figure 2.8a that, in the low-frequency region, only two periods of  $\left| \mathcal{D}_y^{P,N,M}(\hat{\mathbf{k}}) \right|$  do not vanish and the rest of the signal decays due to the sinc term. In Figure 2.8b, on the other hand, due to the sine term,  $\left| \mathcal{E}_z(\hat{\mathbf{k}}) \right|$  shows a quasi-periodic structure and increases in the high-frequency regions due to the  $1/k_z$  term.

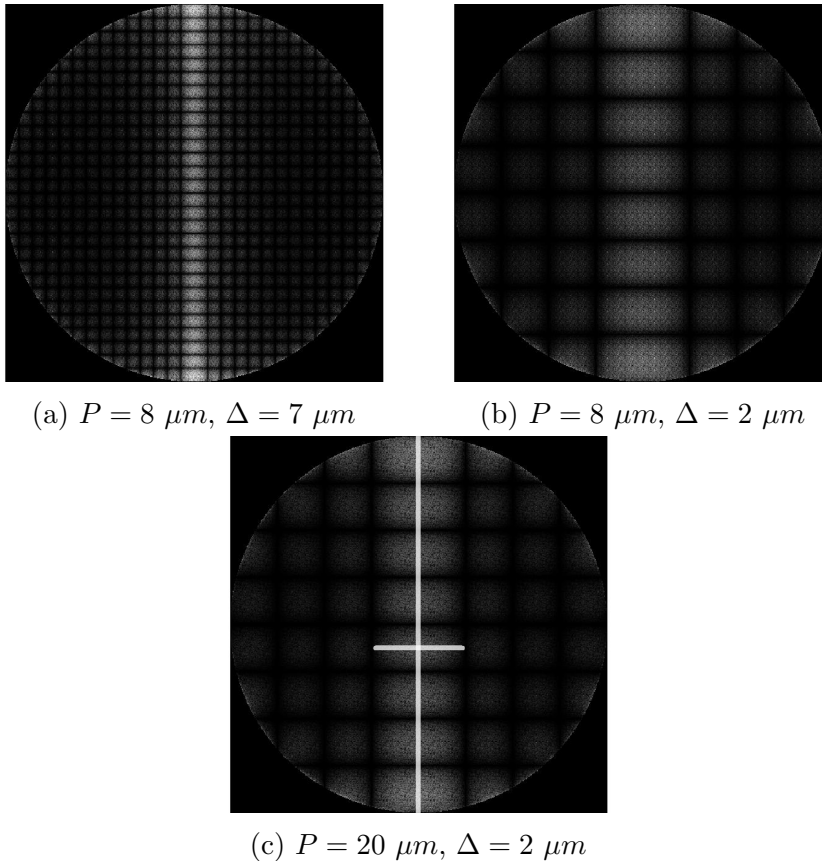
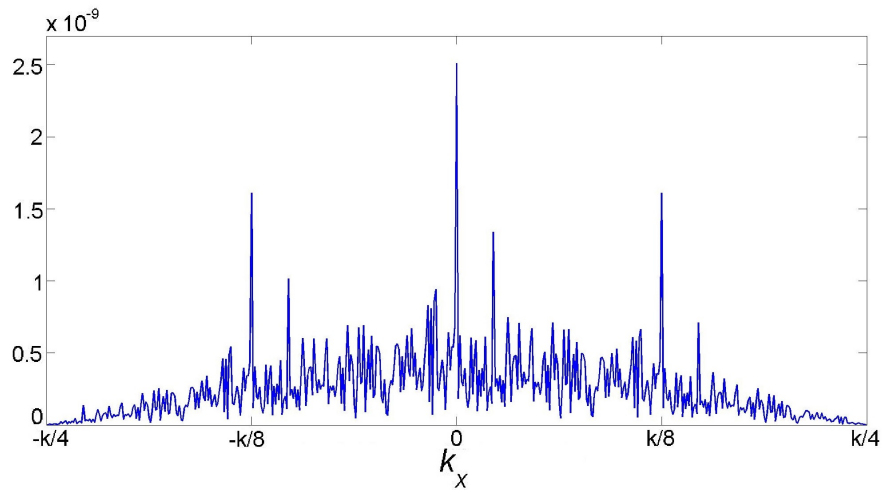
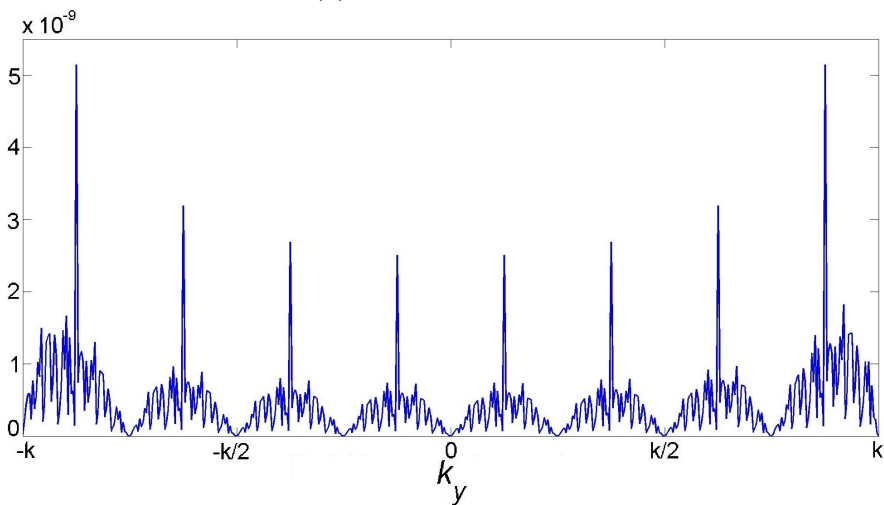


Figure 2.7: The  $|\mathcal{E}_z(\hat{\mathbf{k}})|$  of Equation 2.54 are shown as gray scale images in three cases. In the figures, the frequency axes are along the spatial frequency variables  $k_x$  and  $k_y$  that correspond to the horizontal and vertical axes, respectively and  $k_x, k_y \in [-k, k)$ . The centers of the images correspond to  $(k_x, k_y) = (0, 0)$  point. The frequency increases along the horizontal axis from left to right, and along the vertical axis from top to bottom. The images are shown in log scale for better illustration. The horizontal and vertical lines in Figure 2.7c indicate the locations of 1D cross-sections shown in Figure 2.8. (©2016 IEEE. Reprinted with permission. Published in [75].)



(a) Horizontal profile



(b) Vertical profile

Figure 2.8: Horizontal and vertical profiles of Figure 2.7c at  $k_y = k/8$  and  $k_x = 0$  are shown. (©2016 IEEE. Reprinted with permission. Published in [75].)

### 2.2.3 Validity of the Conventional Scalar Approximation as a Function of the Pixel Size

In order to compute the amount of error in the conventional scalar approximation,  $\epsilon$ , we use Equation 2.38 as the error measure. Please note that, we use Equation 2.37 for the conventional scalar-to-vector field mapping. For a propagating field written on the display, the error can be written as

$$\epsilon = \frac{\int_P \text{sinc}^2\left(\frac{k_x \Delta}{2\pi}\right) \text{sinc}^2\left(\frac{k_y \Delta}{2\pi}\right) \left| \mathcal{D}_s^{P,N,M}(\hat{\mathbf{k}}) \right|^2 \left| \frac{k_x + Ck_y}{k_z} \right|^2 d\hat{\mathbf{k}}}{\int_P \text{sinc}^2\left(\frac{k_x \Delta}{2\pi}\right) \text{sinc}^2\left(\frac{k_y \Delta}{2\pi}\right) \left| \mathcal{D}_s^{P,N,M}(\hat{\mathbf{k}}) \right|^2 \left( 1 + |C|^2 + \left| \frac{k_x + Ck_y}{k_z} \right|^2 \right) d\hat{\mathbf{k}}}, \quad (2.55)$$

where,

$$\mathcal{D}_s^{P,N,M}(\hat{\mathbf{k}}) = \sum_{m=0}^{M-1} \sum_{n=0}^{N-1} \hat{S}[n, m] e^{-jP(k_x n + k_y m)}, \quad (2.56)$$

for a given scalar field,  $\hat{S}[n, m] \in \mathbb{C}$ . Also, the subscript of the integral symbols,  $P$ , indicates that the integration is computed in the propagating region.

In a single pixel analysis, in which  $\mathcal{D}_s^{P,N,M}(\hat{\mathbf{k}})$  becomes constant for all  $k_x$  and  $k_y$  values, it can be shown that, the result of Equation 2.55 is independent from the value of  $C$ . Moreover, the terms within the integrands can be written as a function of  $\Delta/\lambda$ . In Figure 2.9, we show the percent error on the scalar theory for a single pixel,  $\epsilon$ , as a function of  $\Delta/\lambda$  which is assumed to vary between 1.5 and 25 for  $\lambda = 500 \text{ nm}$ . We compute the integrals in Equation 2.55 by using a numeric method. In the figure, although the error decreases as  $\Delta/\lambda$  increases in general trend, this decrease is not monotonic and there are some local oscillations, especially for the small values of  $\Delta/\lambda$ . For example, when  $1.5 \leq \Delta/\lambda \leq 5$ , the error oscillates between 43% and 5%. At these locations, smaller errors can be obtained even if  $\Delta/\lambda$  decreases. For example, when  $\Delta/\lambda$  is 2.5, the introduced error is 27%. However, when  $\Delta/\lambda$  is 2, the introduced error is 12%. For the large values of  $\Delta/\lambda$ , on the other hand, there is almost no oscillation and when  $\Delta/\lambda > 15$ , the error percentage is at most 3%.

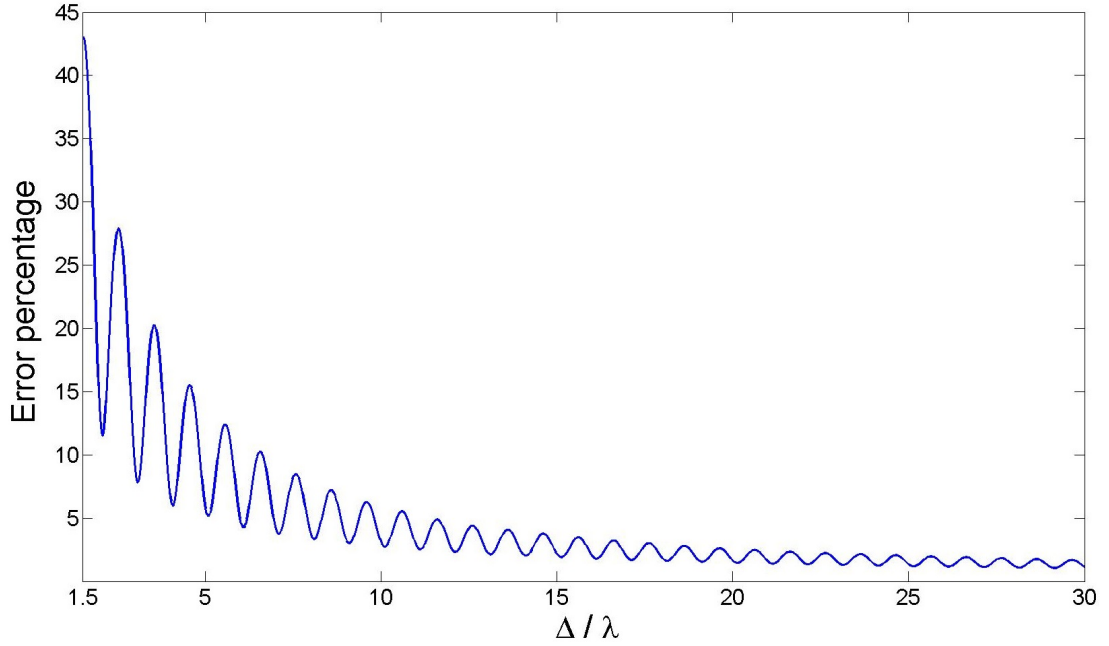


Figure 2.9: The error in the scalar approximation,  $\epsilon$ , is shown for a single pixel as a function of the normalized width of the active region with respect to the wavelength, which is assumed as  $\lambda = 500 \text{ nm}$ . (©2016 IEEE. Reprinted with permission. Published in [75].)

As opposed to the single pixel analysis, if  $\mathcal{D}_s^{P,N,M}(\hat{\mathbf{k}})$  shows an unequal distribution over the frequency domain, then the error on the scalar theory may depend on the value of  $C$ . In order to show this, we consider two cases, that are  $C = 0$  and  $C = \infty$ , which correspond to  $x$  and  $y$ -polarized fields, respectively. In these cases, in the computation of the energy of the  $z$  component, as shown in Equation 2.55,  $\mathcal{D}_s^{P,N,M}(\hat{\mathbf{k}})$  is multiplied by  $k_x^2$  and  $k_y^2$ , respectively. If, for example,  $\mathcal{D}_s^{P,N,M}(\hat{\mathbf{k}})$  is large for the large values of  $k_x$ , then the error in the  $C = 0$  case becomes larger than the  $C = \infty$  case. As a result, if the display configuration is such that the output is linearly polarized along the  $x$  direction, then the scalar theory becomes more erroneous for the scalar fields whose main propagation direction skew toward the  $x$  direction. The inverse is also valid. Moreover, this fact can be generalized for arbitrary directions as follows: If the propagation direction of the scalar wave is dominant along a certain direction at the  $x$ - $y$  plane, then the scalar theory becomes more accurate if the direction of the linear polarization of the outgoing wave is vertical to the dominant direction of the scalar wave.

After having analyzed the use of the conventional scalar approximation in the flat panel and pixelated 3D displays, in the following section, we derive a method for the local analysis of the error in wide optical fields.

## **2.3 Analysis of Local Error in Wide Optical Fields due to the Conventional Scalar Approximation**

In this section, which is mainly based on our publication [76], a space-frequency decomposition based method in spatially wide optical fields is presented, in order to compute the error which arises due to the use of the conventional scalar approximation.

### **2.3.1 Importance of the Location of an Optical Sensor in Wide Optical Fields**

In the literature, it is usually assumed that an optical sensor, which can be, for example, a human eye or camera, interacts with all the optical field on the hypothetical plane on which the sensor is located. For example, the paraxial imaging formulation using a thin lens is formulated based on this assumption, where all the plane wave components which falls within the diffraction limit of the imaging device are assumed to be captured by the optical sensor [4]. This assumption holds true if the object to be displayed or imaged has a narrow extent in space, such as, microscopic applications. On the other hand, if the optical field has a large extent in space, then the optical field may show different space-frequency characteristics and the location of the optical sensor becomes important. For example, if two distinct 3D objects are simultaneously displayed by a 3D display, then, an optical sensor may capture the optical field diffracted from either or both of the objects, depending on the location of the sensor.

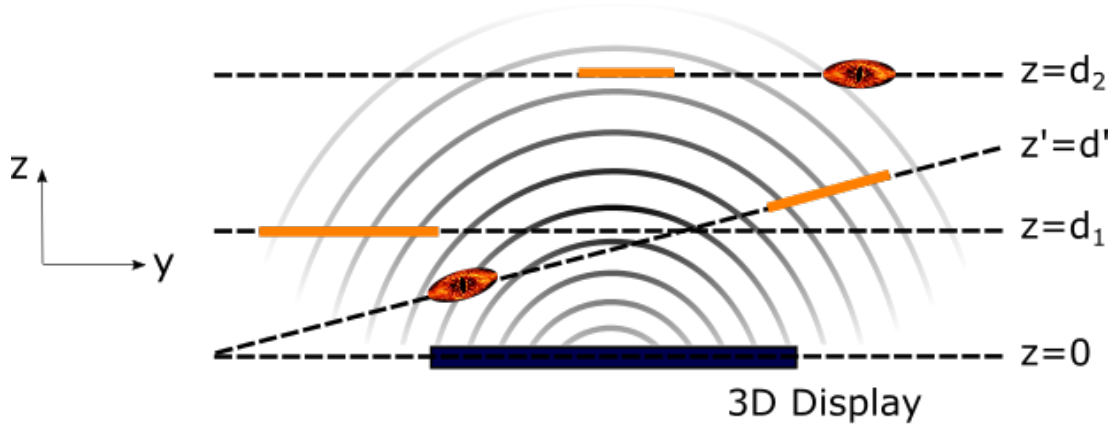


Figure 2.10: A holographic display setup is shown in a 2D space. The display is located at the  $z = 0$  plane and different optical sensors, which are shown in different geometries, are located at different parallel and tilted planes. (©2017 IEEE. Reprinted with permission. Published in [76].)

In Figure 2.10, we show an example of a holographic setup to present the importance of the location of the sensors. For the sake of a simple illustration, the setup is depicted over a 2D  $y$ - $z$  plane, where the display is located at the  $z = 0$  plane. Different optical sensors, which are shown either in elliptical geometry or as flat lines, are located at different parallel or tilted planes. As it is shown in this setup, two different sensors which are located at the same plane receive different optical field diffracted from the display.

Within the scope of this discussion, in this section, we present a space-frequency decomposition based analysis method for the use of the conventional scalar approximation, which is given by Equation 2.37, for wide optical fields. To compute the local error, we choose the 2D short-space Fourier transform (STFT) as the analysis tool. The reason of this choice is, since the basis functions, which are the modulated and shifted Gaussian functions, have the minimum space-bandwidth product, the space-frequency resolution is large [8]. Also, the spatial extent of these basis functions can be adjusted as desired in a simple manner.

### 2.3.2 Computation of Local Error in Parallel and Tilted Planes

We define the 2D STFT of a 2D scalar function,  $U(\hat{\mathbf{r}})$ , as [90]

$$\mathcal{U}_{\sigma, \hat{\mathbf{r}}_0}(\hat{\mathbf{k}}) = \int_{-\infty}^{\infty} U(\hat{\mathbf{r}}) g_{\sigma}(\hat{\mathbf{r}} - \hat{\mathbf{r}}_0) e^{-j\hat{\mathbf{k}}^T \hat{\mathbf{r}}} d\hat{\mathbf{r}} \quad , \quad (2.57)$$

where,  $\hat{\mathbf{r}}_0 = [x_0 \ y_0]^T$  is the center of the analyzed region and

$$g_{\sigma}(\hat{\mathbf{r}}) = \frac{1}{2\pi\sigma^2} e^{-\frac{|\hat{\mathbf{r}}|^2}{2\sigma^2}} \quad (2.58)$$

is the 2D Gaussian function. As  $\sigma$  gets larger, the spatial extent of the Gaussian function gets larger, as well [90]. However, due to the uncertainty relation, for the large values of  $\sigma$ , the bandwidth of the Gaussian function becomes small. In Equation 2.57,  $\sigma$  and  $\hat{\mathbf{r}}_0$  can be associated with the width and the center locations of the optical sensors which are shown in Figure 2.10. Equation 2.57 can also be seen as the 2D FT of  $U(\hat{\mathbf{r}})$  multiplied by the modulated and shifted Gauss function.

In order to compute the local error at a  $z$  plane, which is assumed to be located parallel to the display, we first multiply the electric field components by the 2D shifted Gaussian function as

$$E_{i, \sigma, \hat{\mathbf{r}}_0}(\hat{\mathbf{r}}, z) = E_i(\hat{\mathbf{r}}, z) g_{\sigma}(\hat{\mathbf{r}} - \hat{\mathbf{r}}_0) \quad , \quad (2.59)$$

where  $i \in \{x, y, z\}$ . Then, 2D STFT of  $E_i(\hat{\mathbf{r}}, z)$  can be written as

$$\begin{aligned} \mathfrak{F}_{2D} \left\{ E_{i, \sigma, \hat{\mathbf{r}}_0}(\hat{\mathbf{r}}, z) \right\} &= \mathcal{E}_{i, \sigma, \hat{\mathbf{r}}_0}(\hat{\mathbf{k}}, z) \\ &= \frac{1}{4\pi^2} \left( \mathcal{E}_i(\hat{\mathbf{k}}) e^{jz\sqrt{k^2 - |\hat{\mathbf{k}}|^2}} \right) ** \left( G_{\sigma}(\hat{\mathbf{k}}) e^{-j\hat{\mathbf{k}}^T \hat{\mathbf{r}}_0} \right) \quad , \quad (2.60) \end{aligned}$$

where  $\mathfrak{F}_{2D} \{\cdot\}$  represents the 2D FT from  $\hat{\mathbf{k}}$  domain to  $\hat{\mathbf{r}}$  domain and

$$G_{\sigma}(\hat{\mathbf{k}}) = e^{-\frac{\sigma^2 |\hat{\mathbf{k}}|^2}{2}} \quad (2.61)$$

is the 2D FT of  $g_\sigma(\hat{\mathbf{r}})$ , which is given by Equation 2.58 [90]. Finally, by using the error measure given by Equation 2.38, the local error at a  $z$  plane can be computed as

$$\epsilon_{z,\sigma,\hat{\mathbf{r}}_0} = \frac{\int_{-\infty}^{\infty} \left| \mathcal{E}_{z,\sigma,\hat{\mathbf{r}}_0}(\hat{\mathbf{k}}, z) \right|^2 d\hat{\mathbf{k}}}{\int_{-\infty}^{\infty} \left( \left| \mathcal{E}_{x,\sigma,\hat{\mathbf{r}}_0}(\hat{\mathbf{k}}, z) \right|^2 + \left| \mathcal{E}_{y,\sigma,\hat{\mathbf{r}}_0}(\hat{\mathbf{k}}, z) \right|^2 + \left| \mathcal{E}_{z,\sigma,\hat{\mathbf{r}}_0}(\hat{\mathbf{k}}, z) \right|^2 \right) d\hat{\mathbf{k}}} . \quad (2.62)$$

As a result, by computing  $\epsilon_{z,\sigma,\hat{\mathbf{r}}_0}$  for different values of  $z$ ,  $\sigma$  and  $\hat{\mathbf{r}}_0$ , the local error at different parallel planes and different regions can be analyzed.

Next, in order to compute the local error at a tilted plane, we first define a  $3 \times 3$  rotation matrix  $\mathbf{R}$  such that

$$\mathbf{R}\mathbf{r} = \mathbf{r}' = [x' \ y' \ z']^T , \quad (2.63)$$

where  $\mathbf{R}$  is assumed to be suitably chosen such that the optical sensor is located at a  $z'$  plane and in the form

$$\mathbf{R} = \begin{bmatrix} r_{11} & r_{12} & r_{13} \\ r_{21} & r_{22} & r_{23} \\ r_{31} & r_{32} & r_{33} \end{bmatrix} . \quad (2.64)$$

Since each component of the electric field obeys the scalar field diffraction rules, the field components at a tilted  $z'$  plane can be computed using the methods developed for the scalar fields [91–96]. These field components in the rotated components can be written as

$$\mathbf{E}(\mathbf{R}^T \mathbf{r}') = \frac{1}{4\pi^2} \int_P \boldsymbol{\mathcal{E}}(\hat{\mathbf{R}}^T \mathbf{k}') e^{j\mathbf{k}'^T \mathbf{r}' \frac{r_{13}k_{x'} + r_{23}k_{y'} + r_{33}k_{z'}}{k_{z'}}} d\hat{\mathbf{k}}' , \quad (2.65)$$

where  $\mathbf{R}\mathbf{k} = \mathbf{k}' = [k_{x'} \ k_{y'} \ k_{z'}]^T$ ,  $\hat{\mathbf{k}}' = [k_{x'} \ k_{y'}]^T$ ,

$$\hat{\mathbf{R}} = \begin{bmatrix} r_{11} & r_{12} \\ r_{21} & r_{22} \\ r_{31} & r_{32} \end{bmatrix} \quad (2.66)$$

and the subscript  $P$  indicates that the integration is taken only for the propagating fields. Please note that, in Equation 5.21,  $x$ ,  $y$  and  $z$  components of the

electric field are separately computed in the rotated coordinates. Apart from this computation, since we assume that the scalar field is directly associated with the  $x$  or  $y$  component of the electric field, the components of the electric field vector whose basis functions are decomposed along  $\mathbf{r}'$  direction are not computed. In other words,  $\mathbf{E}(\mathbf{R}^T \mathbf{r}')$  indicates the electric field vector at point  $\mathbf{r}'$  but decomposed along  $\mathbf{r}$  directions. Further explanations about the representation of the electric field vector in the rotated coordinates can also be found in Chapter 5.

Finally, in order to compute the local error at a tilted  $z'$  plane, the procedure given for the calculation of error for the parallel planes can be used by replacing  $\mathcal{E}_{i,\sigma,\hat{\mathbf{r}}_0}(\hat{\mathbf{k}}, z)$  by the 2D STFTs  $\mathbf{E}(\mathbf{R}^T \mathbf{r}')$  in Equation 2.62.

### 2.3.3 Simulation Results

In this section, we present a digital simulation result which reveals the local error in the conventional scalar approximation. For the discretization and digital filtering operations, we use the method described in Section 2.1.4. Also, for illustration purposes, we perform the simulations in a 2D space, where the  $y$  axis in the space and the  $y$  component of the electric field are ignored. However, extension of the analysis to the 3D space is straightforward. In the simulation, we do not specify a parameter to indicate a  $z$  or  $z'$  plane, either, since the analysis method is generic for all such planes.

We choose a 1D chirp signal as our test pattern, as this signal covers all the frequency band at its different location [89]. So, we generate the  $x$  component of the electric field, that is also assumed as the scalar field, as

$$\hat{E}_x[n_x] = e^{j\frac{\pi}{N}n_x^2} \quad , \quad (2.67)$$

where  $n_x \in [0, N - 1]$  is the discrete index and we choose  $N = 2048$ . The digital Gaussian function is defined as

$$\hat{g}_{\hat{\sigma}}[n_x - n_0] = e^{-\frac{(n_x - n_0)^2}{2\hat{\sigma}^2}} \quad , \quad (2.68)$$

where  $\hat{\sigma}$  is chosen as 32 in the simulation and  $n_0$  is chosen in the range  $[0, N - 1]$ . In Figure 2.11, we show the real part of the chosen  $\hat{E}_x [n_x]$ , the magnitude of the resulting  $z$  component and the chosen digital Gaussian function for  $n_0 = 1024$ .

The collections of the STFTs of the electric field components are computed in the discrete domain as

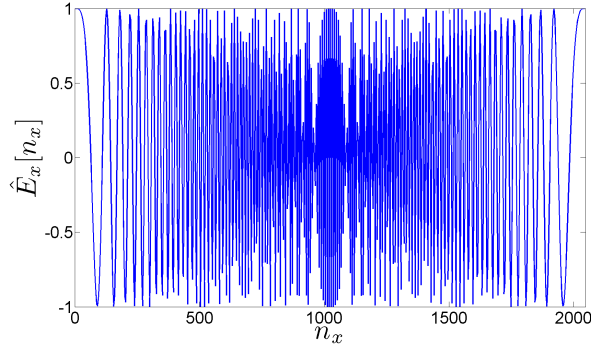
$$\hat{\mathcal{E}}_{i,\hat{\sigma},n_0} [p_x] = DFT_N \left\{ \hat{E}_i [n_x] \hat{g}_{\hat{\sigma}} [n_x - n_0] \right\} \quad , \quad (2.69)$$

where  $DFT_N \{ \cdot \}$  represents the  $N$ -point discrete Fourier transform (DFT) [67]. Here  $p_x \in [0, N - 1]$  indicates the discrete frequency points. So the normalized frequency corresponding to a given  $p_x$  becomes  $2\pi p_x / N$  rad/sample. Finally, the resulting error for a given  $n_0$  can be computed as

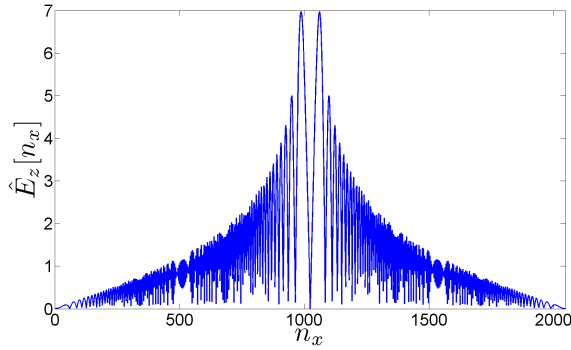
$$\hat{\epsilon}_{n_0} = \frac{\sum_{p_x=0}^{N-1} \left| \hat{\mathcal{E}}_{z,\hat{\sigma},n_0} [p_x] \right|^2}{\sum_{p_x=0}^{N-1} \left( \left| \hat{\mathcal{E}}_{x,\hat{\sigma},n_0} [p_x] \right|^2 + \left| \hat{\mathcal{E}}_{z,\hat{\sigma},n_0} [p_x] \right|^2 \right)} \quad . \quad (2.70)$$

The simulation results are shown in Figure 2.12. As it can be seen from Figure 2.12a, the frequency content of the  $x$  component sweeps all over the frequency range as  $n_0$  increases. Figure 2.12b shows that the frequency content of the  $x$  component is also present in the  $z$  component in the regions which are not suppressed by the highpass filter  $k_x/k_z$ . In addition to the frequency components which are found in the  $x$  component, the  $z$  component has another frequency content in the regions except for the points near  $n_0 = 0$  and  $n_0 = 2047$ , where this content form a horizontal line in Figure 2.12b. The reason of this frequency content is that the highpass filter  $k_x/k_z$  has a very large response when  $k_x$  is large; this can also be seen from Figure 2.4a. Therefore, even if the  $x$  component has a few amount of high-frequency content, this frequency components can be excessively amplified by the highpass filter. In this respect, even if a high-frequency content is not visible in the  $x$  component in Figure 2.12a, these small-amplitude components are excessively amplified by the highpass filter and appear in the  $z$  component.

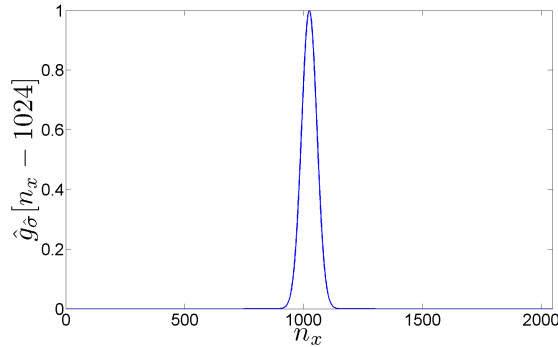
In Figure 2.12c, we also show the error percentage which is computed using Equation 2.70 for different regions. According to this figure, the error in the



(a) The real part of the chosen scalar field, which is given by Equation 2.67



(b) The magnitude of the resulting  $z$  component due to the chosen scalar field



(c) The chosen digital Gaussian function for  $n_0 = 1024$

Figure 2.11: The chosen signals which are used in the simulation are shown. For the sake of brevity, the simulations are performed for one-dimensional signals and the  $y$  component of the electric field is assumed to be zero. Figure 2.11a presents the real part of the chosen scalar field which is also associated with the  $x$  component of the electric field. Figure 2.11b presents the magnitude of the resulting  $z$  component of the electric field, that is also the source of error in the scalar approximation. Figure 2.11c shows the chosen digital Gaussian function with  $\hat{\sigma} = 32$ . (©2017 IEEE. Reprinted with permission. Published in [76].)

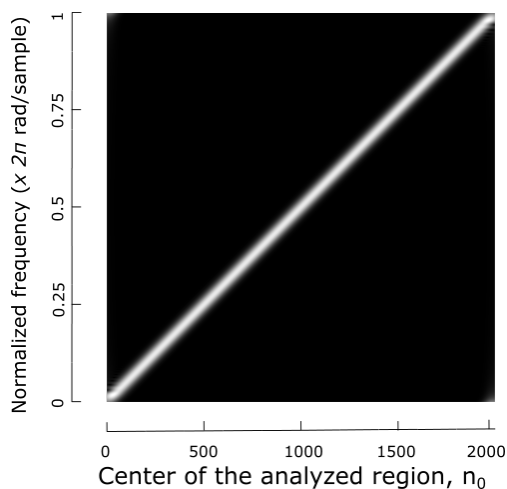
scalar approximation gets larger as the high-frequency content of the analyzed region gets larger. Moreover, the amount of error becomes close to 100% near  $n_0 = 1024$ , where the highest frequency component is located. As a result, based on the discussions made in this chapter, it can be said that the simulation results matches with the expected results.

## 2.4 Summary

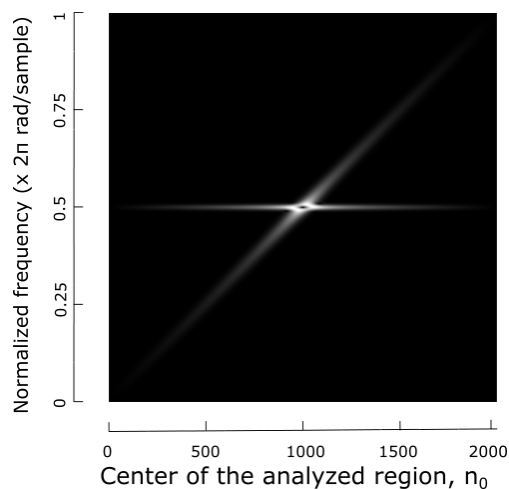
As a summary of this chapter, we first discussed the validity of the conventional scalar approximation to wide-angle optical field propagation in free space. It is shown using the transfer functions of the filters,  $\mathcal{G}_{\{x,y\}}(\hat{\mathbf{k}})$ , which are shown in Figures 2.3 and 2.4, in large angles, the magnitude of the  $z$  component, and hence the error in the conventional scalar approximation increases. As the propagation direction vector of a plane wave becomes close to the wave number  $k$ , this increase becomes more abrupt and the  $z$  component becomes the dominant term of the electric field.

Based on this development, we have shown the relation between the parameters of a pixelated display and the validity of the conventional scalar-to-vector field mapping. Although small pixel size is desired for large viewing angle display applications, however, as the pixel size decreases, the error in the conventional scalar approximation increases, as shown by Figure 2.9. Therefore, a trade-off between the pixel size and the error in the conventional scalar approximation arises.

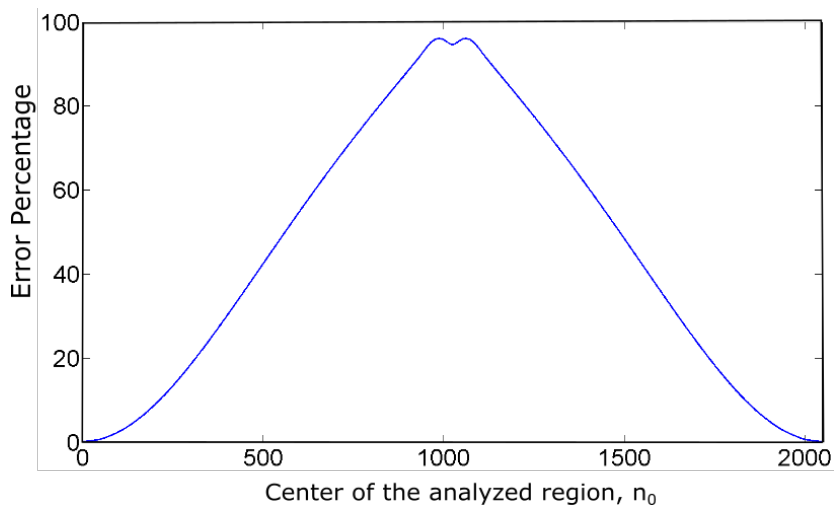
Finally, we have developed an analysis tool for the local error in spatially wide extent optical fields. The local analysis of error becomes important for a relatively small optical sensor which is able to capture some local features of a wide extent optical fields. The tool is based on space-frequency decomposition of the optical field on a parallel or tilted plane with respect to a display. The analysis on a 1D chirp signal showed that, the local error may increase up to 100% at the regions where the local frequency is close to the wave number  $k$ , which is also consistent



(a) The space-frequency analysis of the  $x$  component



(b) The space-frequency analysis of the  $z$  component



(c) Local error percentage

Figure 2.12: Simulation results are shown. Figure 2.12a presents the space-frequency analysis of the  $x$  component of the electric field, that is given by Equation 2.67 and its real part is shown in Figure 2.11a. Figure 2.12b presents the space-frequency analysis of the  $z$  component of the electric field, whose magnitude is shown in Figure 2.11b. Figure 2.12c shows the local error, which is calculated by Equation 2.70, in the scalar approximation for the tested signals. (©2017 IEEE. Reprinted with permission. Published in [76].)

with the transfer functions as shown by Figures 2.3 and 2.4.

Before developing some other scalar-to-vector field mappings which can be used to represent larger set of electromagnetic fields in the subsequent chapters, we are going to present a general constraint for the electromagnetic fields such that they can be fully represented by a single scalar wave in the next chapter.

## Chapter 3

# Set of Electromagnetic Fields that can be Fully Represented by a Scalar Wave Field

In this chapter, which depends on our publication [97], we develop a general constraint for the electromagnetic fields such that the set of electromagnetic fields which are generated under this constraint can be fully represented and characterized by a scalar wave field, where the scalar wave field obeys the diffraction and propagation formulas given in Chapter 1. The conventional scalar-to-vector field mapping, whose limitations are discussed in Chapter 2, remains a special case of this general framework. Before developing the constraint, we first present the computation of the magnetic field components from the transverse components of the electric field.

### 3.1 Systems Formulation of the Computation of the Magnetic Field from the Transverse Components of the Electric Field

In Chapter 2, computation of the  $z$  component of the electric field from the  $x$  and  $y$  components are presented; the model is based on a signals and systems perspective. In addition to this, in this section, we first formulate the computation of the magnetic field vector components from the  $x$  and  $y$  components of the electric field, again from a signals and systems point of view. So, the 2D inputs to the systems are  $E_x(\hat{\mathbf{r}}, z)$  and  $E_y(\hat{\mathbf{r}}, z)$ , where  $\hat{\mathbf{r}} = [x \ y]^T$ , and the outputs are the components of the magnetic field vector at the given  $z$  plane. The inputs are fed to different systems for each output, as shown below.

By using the relations given in Equations 1.33, 1.34 and 1.35, the 2D FT of the components of the magnetic field vector,  $\mathcal{H}(\hat{\mathbf{k}})$ , where  $\hat{\mathbf{k}} = [k_x \ k_y]^T$ , can be computed as [70, 72, 73]

$$\mathcal{H}_x(\hat{\mathbf{k}}) = \frac{\mathcal{E}_z(\hat{\mathbf{k}}) k_y - \mathcal{E}_y(\hat{\mathbf{k}}) k_z}{k\eta} \quad , \quad (3.1)$$

$$\mathcal{H}_y(\hat{\mathbf{k}}) = \frac{\mathcal{E}_x(\hat{\mathbf{k}}) k_z - \mathcal{E}_z(\hat{\mathbf{k}}) k_x}{k\eta} \quad , \quad (3.2)$$

$$\mathcal{H}_z(\hat{\mathbf{k}}) = \frac{\mathcal{E}_y(\hat{\mathbf{k}}) k_x - \mathcal{E}_x(\hat{\mathbf{k}}) k_y}{k\eta} \quad , \quad (3.3)$$

where  $\eta$  is the wave impedance of the medium and approximately equals to  $120\pi$  ohms in free space [70]. By using the filters  $\mathcal{G}_x(\hat{\mathbf{k}})$  and  $\mathcal{G}_y(\hat{\mathbf{k}})$ , which are defined in Equations 2.12 and 2.13, Equations 3.1, 3.2 and 3.3 can be written as

$$\begin{aligned} \mathcal{H}_x(\hat{\mathbf{k}}) &= \frac{[\mathcal{E}_x(\hat{\mathbf{k}}) \mathcal{G}_x(\hat{\mathbf{k}}) + \mathcal{E}_y(\hat{\mathbf{k}}) \mathcal{G}_y(\hat{\mathbf{k}})] k_y - \mathcal{E}_y(\hat{\mathbf{k}}) k_z}{k\eta} \\ &= \begin{cases} \mathcal{E}_x(\hat{\mathbf{k}}) \frac{-k_x k_y}{k\eta\sqrt{k^2 - |\hat{\mathbf{k}}|^2}} + \mathcal{E}_y(\hat{\mathbf{k}}) \frac{-k^2 + k_x^2}{k\eta\sqrt{k^2 - |\hat{\mathbf{k}}|^2}} & \text{if } |\hat{\mathbf{k}}| \neq k \\ 0 & \text{otherwise} \end{cases} \\ &= \mathcal{E}_x(\hat{\mathbf{k}}) \mathcal{G}_{xx}(\hat{\mathbf{k}}) + \mathcal{E}_y(\hat{\mathbf{k}}) \mathcal{G}_{xy}(\hat{\mathbf{k}}) \quad , \end{aligned} \quad (3.4)$$

$$\begin{aligned}
\mathcal{H}_y(\hat{\mathbf{k}}) &= \frac{\mathcal{E}_x(\hat{\mathbf{k}})k_z - [\mathcal{E}_x(\hat{\mathbf{k}})\mathcal{G}_x(\hat{\mathbf{k}}) + \mathcal{E}_y(\hat{\mathbf{k}})\mathcal{G}_y(\hat{\mathbf{k}})]k_x}{k\eta} \\
&= \begin{cases} \mathcal{E}_x(\hat{\mathbf{k}})\frac{k^2-k_y^2}{k\eta\sqrt{k^2-|\hat{\mathbf{k}}|^2}} + \mathcal{E}_y(\hat{\mathbf{k}})\frac{k_xk_y}{k\eta\sqrt{k^2-|\hat{\mathbf{k}}|^2}} & \text{if } |\hat{\mathbf{k}}| \neq k \\ 0 & \text{otherwise} \end{cases} \\
&= \mathcal{E}_x(\hat{\mathbf{k}})\mathcal{G}_{yx}(\hat{\mathbf{k}}) + \mathcal{E}_y(\hat{\mathbf{k}})\mathcal{G}_{yy}(\hat{\mathbf{k}}) \quad , \quad (3.5)
\end{aligned}$$

$$\begin{aligned}
\mathcal{H}_z(\hat{\mathbf{k}}) &= \mathcal{E}_x(\hat{\mathbf{k}})\frac{-k_y}{k\eta} + \mathcal{E}_y(\hat{\mathbf{k}})\frac{k_x}{k\eta} \\
&= \mathcal{E}_x(\hat{\mathbf{k}})\mathcal{G}_{zx}(\hat{\mathbf{k}}) + \mathcal{E}_y(\hat{\mathbf{k}})\mathcal{G}_{zy}(\hat{\mathbf{k}}) \quad . \quad (3.6)
\end{aligned}$$

Therefore, Equations 3.4, 3.5 and 3.6 represent two-input-single-output LSI systems with the transfer functions indicated in the above equations as  $\mathcal{G}_{xx}(\hat{\mathbf{k}})$ ,  $\mathcal{G}_{xy}(\hat{\mathbf{k}})$ ,  $\mathcal{G}_{yx}(\hat{\mathbf{k}})$ ,  $\mathcal{G}_{yy}(\hat{\mathbf{k}})$ ,  $\mathcal{G}_{zx}(\hat{\mathbf{k}})$  and  $\mathcal{G}_{zy}(\hat{\mathbf{k}})$ .

In order to compute the components of the magnetic field vector from  $E_x(\hat{\mathbf{r}}, z)$  and  $E_y(\hat{\mathbf{r}}, z)$  in the space domain, we calculate the impulse responses of the transfer functions as

$$g_{ij}(\hat{\mathbf{r}}) = \mathfrak{F}_{2D}^{-1}\{\mathcal{G}_{ij}(\hat{\mathbf{k}})\} \text{ for all } i \in \{x, y\} \text{ and } j \in \{x, y\} \quad , \quad (3.7)$$

where  $\mathfrak{F}_{2D}^{-1}\{\cdot\}$  denotes the 2D IFT. For this purpose, we utilize Equations 2.18, 2.19 and the derivative property of the FT. So,

$$g_{xx}(\hat{\mathbf{r}}) = -g_{yy}(\hat{\mathbf{r}}) = \frac{1}{jk\eta}\frac{\partial g_y(\hat{\mathbf{r}})}{\partial x} = \frac{1}{jk\eta}\frac{\partial g_x(\hat{\mathbf{r}})}{\partial y} \quad , \quad (3.8)$$

$$g_{xy}(\hat{\mathbf{r}}) = -\frac{k}{\eta}g_0(\hat{\mathbf{r}}) + \frac{j}{k\eta}\frac{\partial g_x(\hat{\mathbf{r}})}{\partial x} \quad , \quad (3.9)$$

$$g_{yx}(\hat{\mathbf{r}}) = \frac{k}{\eta}g_0(\hat{\mathbf{r}}) - \frac{j}{k\eta}\frac{\partial g_y(\hat{\mathbf{r}})}{\partial y} \quad . \quad (3.10)$$

Therefore, from the convolution and derivative properties of the FT, the components of the magnetic field vector in space domain can be written as

$$H_x(\hat{\mathbf{r}}, z) = E_x(\hat{\mathbf{r}}, z) ** g_{xx}(\hat{\mathbf{r}}) + E_y(\hat{\mathbf{r}}, z) ** g_{xy}(\hat{\mathbf{r}}) \quad , \quad (3.11)$$

$$H_y(\hat{\mathbf{r}}, z) = E_x(\hat{\mathbf{r}}, z) ** g_{yx}(\hat{\mathbf{r}}) + E_y(\hat{\mathbf{r}}, z) ** g_{yy}(\hat{\mathbf{r}}) \quad , \quad (3.12)$$

$$H_z(\hat{\mathbf{r}}, z) = \frac{j}{k\eta}\frac{\partial E_x(\hat{\mathbf{r}}, z)}{\partial y} - \frac{j}{k\eta}\frac{\partial E_y(\hat{\mathbf{r}}, z)}{\partial x} \quad . \quad (3.13)$$

Please note that, if the field is known to be consisting of only propagating components, then,  $g_0(\hat{\mathbf{r}})$ ,  $g_x(\hat{\mathbf{r}})$  and  $g_y(\hat{\mathbf{r}})$  can be replaced by  $g_{0,p}(\hat{\mathbf{r}})$ ,  $g_{x,p}(\hat{\mathbf{r}})$  and  $g_{y,p}(\hat{\mathbf{r}})$  in Equations 3.8, 3.9 and 3.10. In case there are evanescent modes, such modes in the 3D field are restricted to those with real valued  $\hat{\mathbf{k}}$  as implied by the choice in Equation 2.1.

To sum up, in free space, if the  $x$  and  $y$  components of the electric field are known over an arbitrary  $z$  plane, then all the field components at 3D space can be found through LSI systems. So, the free space propagation of all of the electromagnetic field components, computation of the  $z$  component of the electric field and the computations of the  $x$ ,  $y$  and  $z$  components of the magnetic field from the  $x$  and  $y$  components of the electric field can be performed through convolutions in space, or through multiplications in the Fourier domains. In this respect, in the following section, we impose a constraint between the  $x$  and  $y$  components of the electric field such that, under this restriction, entire electromagnetic field can be fully represented.

## 3.2 A General Constraint on the Scalar Representation of Electromagnetic Fields

In this section, we first introduce a new complex valued 3D scalar function,  $S(\mathbf{r})$ , to represent a constrained electromagnetic field. We assume that  $S(\hat{\mathbf{r}}, z)$  can be computed from  $S(\hat{\mathbf{r}}, 0)$  as

$$S(\hat{\mathbf{r}}, z) = S(\hat{\mathbf{r}}, 0) **f_z(\hat{\mathbf{r}}) \quad . \quad (3.14)$$

So,  $S(\mathbf{r})$  obeys the scalar wave equation and the same free space propagation rule also applies to the scalar field  $S(\mathbf{r})$ , which is valid for the components of the electric and magnetic field vectors. Then we assume that the  $x$  and  $y$  components of the electric field at  $z = 0$  plane can be found through some invertible transforms

from the scalar field  $S(\hat{\mathbf{r}}, 0)$ . That is

$$E_x(\hat{\mathbf{r}}, 0) = \mathfrak{T}_x \left\{ S(\hat{\mathbf{r}}, 0) \right\} \quad , \quad (3.15)$$

$$E_y(\hat{\mathbf{r}}, 0) = \mathfrak{T}_y \left\{ S(\hat{\mathbf{r}}, 0) \right\} \quad , \quad (3.16)$$

where  $\mathfrak{T}_x : \mathbb{C} \rightarrow \mathbb{C}$  and  $\mathfrak{T}_y : \mathbb{C} \rightarrow \mathbb{C}$  are some one-to-one predetermined operators together with their inverse transforms  $\mathfrak{T}_x^{-1}$  and  $\mathfrak{T}_y^{-1}$ . So  $E_x(\hat{\mathbf{r}}, 0)$  and  $E_y(\hat{\mathbf{r}}, 0)$  are assumed to be related through

$$E_x(\hat{\mathbf{r}}, 0) = \mathfrak{T}_x \left\{ \mathfrak{T}_y^{-1} \left\{ E_y(\hat{\mathbf{r}}, 0) \right\} \right\} \quad , \quad (3.17)$$

$$E_y(\hat{\mathbf{r}}, 0) = \mathfrak{T}_y \left\{ \mathfrak{T}_x^{-1} \left\{ E_x(\hat{\mathbf{r}}, 0) \right\} \right\} \quad . \quad (3.18)$$

These imposed relations create the constraint on the electromagnetic fields that we deal with.

If the transforms  $\mathfrak{T}_{\{x,y\}}$  are commutative with the free space propagation, that is,

$$\mathfrak{T}_{\{x,y\}} \left\{ S(\hat{\mathbf{r}}, 0) \right\} ** f_z(\hat{\mathbf{r}}) = \mathfrak{T}_{\{x,y\}} \left\{ S(\hat{\mathbf{r}}, 0) ** f_z(\hat{\mathbf{r}}) \right\} \quad , \quad (3.19)$$

for all  $z$ , then,  $E_{\{x,y\}}(\hat{\mathbf{r}}, z)$  can be computed from  $S(\hat{\mathbf{r}}, z)$  at all  $z$  planes by using the same transforms,  $\mathfrak{T}_{\{x,y\}}$ . Moreover, if  $\mathfrak{T}_{\{x,y\}}$  commute with the operations which are used to find  $E_z(\hat{\mathbf{r}}, z)$  and  $\mathbf{H}(\hat{\mathbf{r}}, z)$  from  $E_{\{x,y\}}(\hat{\mathbf{r}}, z)$ , then  $E_z(\hat{\mathbf{r}}, z)$  and  $\mathbf{H}(\hat{\mathbf{r}}, z)$  can be computed using  $\mathfrak{T}_{\{x,y\}}$  and  $S(\hat{\mathbf{r}}, z)$  at any  $z$  plane as

$$E_z(\hat{\mathbf{r}}, z) = \mathfrak{T}_x \left\{ S(\hat{\mathbf{r}}, z) ** g_x(\hat{\mathbf{r}}) \right\} + \mathfrak{T}_y \left\{ S(\hat{\mathbf{r}}, z) ** g_y(\hat{\mathbf{r}}) \right\} \quad , \quad (3.20)$$

$$H_x(\hat{\mathbf{r}}, z) = \mathfrak{T}_x \left\{ S(\hat{\mathbf{r}}, z) ** g_{xx}(\hat{\mathbf{r}}) \right\} + \mathfrak{T}_y \left\{ S(\hat{\mathbf{r}}, z) ** g_{xy}(\hat{\mathbf{r}}) \right\} \quad , \quad (3.21)$$

$$H_y(\hat{\mathbf{r}}, z) = \mathfrak{T}_x \left\{ S(\hat{\mathbf{r}}, z) ** g_{yx}(\hat{\mathbf{r}}) \right\} + \mathfrak{T}_y \left\{ S(\hat{\mathbf{r}}, z) ** g_{yy}(\hat{\mathbf{r}}) \right\} \quad , \quad (3.22)$$

$$H_z(\hat{\mathbf{r}}, z) = \mathfrak{T}_x \left\{ \frac{j}{k\eta} \frac{\partial S(\hat{\mathbf{r}}, z)}{\partial y} \right\} - \mathfrak{T}_y \left\{ \frac{j}{k\eta} \frac{\partial S(\hat{\mathbf{r}}, z)}{\partial x} \right\} \quad . \quad (3.23)$$

In this respect,  $\mathfrak{T}_{\{x,y\}}$  can be used at an arbitrary  $z$  plane in the computation of all components of the electromagnetic field. So, specifying just  $S(\hat{\mathbf{r}}, 0)$  becomes sufficient to find the entire electromagnetic field in 3D space. Furthermore, if the scalar field,  $S(\mathbf{r})$ , is given over a curved surface in free space, the scalar field, and so the electromagnetic field, in 3D space can be found using the methods found in the literature that are developed for the scalar optical fields [98–101].

Now, we choose  $\mathfrak{T}_{\{x,y\}}$  as 2D LSI transforms so that Equations 3.19, 3.20, 3.21, 3.22, and 3.23 are always satisfied. So,  $\mathfrak{T}_x$  and  $\mathfrak{T}_y$  can be associated by the impulse responses,  $t_x(\hat{\mathbf{r}})$  and  $t_y(\hat{\mathbf{r}})$ , respectively, and the transforms can be written as a convolution operation; that is,

$$E_x(\hat{\mathbf{r}}, 0) = S(\hat{\mathbf{r}}, 0) ** t_x(\hat{\mathbf{r}}) \quad , \quad (3.24)$$

$$E_y(\hat{\mathbf{r}}, 0) = S(\hat{\mathbf{r}}, 0) ** t_y(\hat{\mathbf{r}}) \quad . \quad (3.25)$$

Therefore, since the convolution operation is commutative, if  $\mathfrak{T}_{\{x,y\}}$  are 2D LSI transforms, then it is guaranteed that these transforms can be used to find all the components of the electric field in 3D space from a single scalar function  $S(\hat{\mathbf{r}}, 0)$ . In the Fourier domain, the same transform turns out to be

$$\mathcal{E}_x(\hat{\mathbf{k}}) = \mathcal{S}(\hat{\mathbf{k}}) \mathcal{T}_x(\hat{\mathbf{k}}) \quad , \quad (3.26)$$

$$\mathcal{E}_y(\hat{\mathbf{k}}) = \mathcal{S}(\hat{\mathbf{k}}) \mathcal{T}_y(\hat{\mathbf{k}}) \quad , \quad (3.27)$$

where  $\mathcal{T}_{\{x,y\}}(\hat{\mathbf{k}})$  are the corresponding transfer functions and the 2D IFTs of  $t_{\{x,y\}}(\hat{\mathbf{r}})$ .

As it is mentioned in Section 2.1.3, there are some interpretations and works for the mapping of the scalar wave field to the electromagnetic wave field in free space in the literature. In [4], it is stated that a single scalar wave field may represent all the scalar components of electromagnetic vector wave field as each scalar component obeys the same wave equation; however, this is too restrictive. In [65], it is stated that the Kirchoff diffraction formula for the scalar field is valid in the paraxial region by assuming that there is a single transverse component of the electric field; as we have already discussed, paraxial approximation is valid in too restrictive special cases. Here in this section it is shown that if  $E_x(\hat{\mathbf{r}}, 0)$  and  $E_y(\hat{\mathbf{r}}, 0)$  are related to each other through

$$E_x(\hat{\mathbf{r}}, 0) = t_x(\hat{\mathbf{r}}) ** (t_y^{-1}(\hat{\mathbf{r}}) ** E_y(\hat{\mathbf{r}}, 0)) \quad (3.28)$$

or equivalently

$$E_y(\hat{\mathbf{r}}, 0) = t_y(\hat{\mathbf{r}}) ** (t_x^{-1}(\hat{\mathbf{r}}) ** E_x(\hat{\mathbf{r}}, 0)) \quad , \quad (3.29)$$

for some invertible  $t_{\{x,y\}}(\hat{\mathbf{r}})$ , where  $t_{\{x,y\}}^{-1}(\hat{\mathbf{r}})$  represent the corresponding inverse system impulse responses, then a single scalar field characterizes the entire electromagnetic field. The constraints as expressed by Equations 3.28 and 3.29 extend the scalar wave representation of electromagnetic field propagation in free space to cover much wider situations beyond that is implied by [4] and [65].

The impulse responses,  $t_{\{x,y\}}(\hat{\mathbf{r}})$ , or the corresponding transfer functions,  $\mathcal{T}_{\{x,y\}}(\hat{\mathbf{k}})$ , can be chosen based on the needs of an application. In the following chapter, we develop another scalar-to-vector wave field mapping by using some appropriate  $\mathcal{T}_{\{x,y\}}(\hat{\mathbf{k}})$ s so that the power spectra of the scalar field and the corresponding electromagnetic field are equal for wide-angle fields.

# Chapter 4

## Power Spectrum Equalizing Scalar-to-Polarized Optical Field Transformation Technique

In this chapter, we develop a new scalar-to-vector field mapping based on the constraints given in Chapter 3. As a result of the developed mapping, the power spectra of a given scalar field and the generated electromagnetic field become equal in wide-angle fields. The applications of this mapping in wide-angle displays and its advantages over the conventional mapping are presented as computer simulation results, as well. Sections 4.1 and 4.2 of this chapter are mainly based on our publications [97] and [102], respectively.

### 4.1 Inverse Filtering for Power Spectrum Equalization

We define the power spectrum of an electric field as

$$|\mathcal{E}(\hat{\mathbf{k}})|^2 = |\mathcal{E}_x(\hat{\mathbf{k}})|^2 + |\mathcal{E}_y(\hat{\mathbf{k}})|^2 + |\mathcal{E}_z(\hat{\mathbf{k}})|^2 . \quad (4.1)$$

In Equation 1.36, the equality between the magnetic field and the electric field power spectra is given as

$$\eta^2 \left| \mathcal{H}(\hat{\mathbf{k}}) \right|^2 = \left| \mathcal{E}(\hat{\mathbf{k}}) \right|^2 . \quad (4.2)$$

The power spectrum of an electric field can also be interpreted as the power spectrum of the electromagnetic field.

In terms of the assumed scalar field  $\mathcal{S}(\hat{\mathbf{k}})$  and the transfer functions,  $\mathcal{T}_x(\hat{\mathbf{k}}) = \mathfrak{F}_{2D}\{t_x(\hat{\mathbf{r}})\}$  and  $\mathcal{T}_y(\hat{\mathbf{k}}) = \mathfrak{F}_{2D}\{t_y(\hat{\mathbf{r}})\}$ , which are introduced in Equations 3.26 and 3.27, respectively, Equation 4.1 becomes

$$\begin{aligned} \left| \mathcal{E}(\hat{\mathbf{k}}) \right|^2 &= \left| \mathcal{S}(\hat{\mathbf{k}}) \mathcal{T}_x(\hat{\mathbf{k}}) \right|^2 + \left| \mathcal{S}(\hat{\mathbf{k}}) \mathcal{T}_y(\hat{\mathbf{k}}) \right|^2 \\ &+ \left| \mathcal{S}(\hat{\mathbf{k}}) \left( \mathcal{T}_x(\hat{\mathbf{k}}) \mathcal{G}_x(\hat{\mathbf{k}}) + \mathcal{T}_y(\hat{\mathbf{k}}) \mathcal{G}_y(\hat{\mathbf{k}}) \right) \right|^2 . \end{aligned} \quad (4.3)$$

Since our aim is to satisfy  $\left| \mathcal{E}(\hat{\mathbf{k}}) \right|^2 = \left| \mathcal{S}(\hat{\mathbf{k}}) \right|^2$ , the required condition for this purpose becomes

$$1 = \left| \mathcal{T}_x(\hat{\mathbf{k}}) \right|^2 + \left| \mathcal{T}_y(\hat{\mathbf{k}}) \right|^2 + \left| \mathcal{T}_x(\hat{\mathbf{k}}) \mathcal{G}_x(\hat{\mathbf{k}}) + \mathcal{T}_y(\hat{\mathbf{k}}) \mathcal{G}_y(\hat{\mathbf{k}}) \right|^2 . \quad (4.4)$$

Therefore, if  $\mathcal{T}_{\{x,y\}}(\hat{\mathbf{k}})$  are chosen such that Equation 4.4 is satisfied, the power spectra of the scalar field and the corresponding electric field become equal. In this respect, when the magnitude square of the Fourier transform of an electric field can be recorded by an optical system, the proposed scalar-to-vector wave field mapping gives the exact results: the power spectrum of the scalar field and the power spectrum of the corresponding electric field exactly match. For example, it is known that an imaging system which uses a thin lens can record the intensity of the Fourier transform of the input scalar field under some paraxial approximations [4]. If the thin lens is not located along the axis of the imaging system, the intensity image will be significantly incorrect when the conventional scalar-to-vector field mapping is used. However, no error will occur if the filters  $\mathcal{T}_{\{x,y\}}(\hat{\mathbf{k}})$  that satisfy Equation 4.4 are used during the scalar-to-vector field mapping.

As an example, in addition to the equalized power spectrum, if the longitudinal component of the electric field is desired to be set to zero at each point in space,

then,  $\mathcal{T}_{\{x,y\}}(\hat{\mathbf{k}})$  should be chosen as

$$\mathcal{T}_x(\hat{\mathbf{k}}) = \frac{k_y e^{j\theta(\hat{\mathbf{k}})}}{|\hat{\mathbf{k}}|} \quad , \quad (4.5)$$

$$\mathcal{T}_y(\hat{\mathbf{k}}) = -\frac{k_x e^{j\theta(\hat{\mathbf{k}})}}{|\hat{\mathbf{k}}|} \quad , \quad (4.6)$$

where  $\theta(\hat{\mathbf{k}})$  is an arbitrary phase function.

The power spectrum equalization method is used in the literature in image restoration algorithms [103–106], where a blindly convolved and noise added image is tried to be recovered from the measurements. Since  $E_z(\mathbf{r})$  is computed using the filters  $g_{\{x,y\}}(\hat{\mathbf{r}})$  from  $E_{\{x,y\}}(\mathbf{r})$ ,  $\mathcal{T}_{\{x,y\}}(\hat{\mathbf{k}})$  can be seen as the inverse filters which compensate the excessively large magnitudes of  $\mathcal{G}_{\{x,y\}}(\hat{\mathbf{k}})$  that occur at large frequencies [74]. Since the measured quantity of the optical field can be the electric field intensity, that is defined as

$$|\mathbf{E}(\mathbf{r})|^2 = |E_x(\mathbf{r})|^2 + |E_y(\mathbf{r})|^2 + |E_z(\mathbf{r})|^2 \quad , \quad (4.7)$$

by applying these inverse filters, it can be expected in  $|\mathbf{E}(\mathbf{r})|^2$  that the excessively amplified high-frequency components due to the  $\mathcal{G}_{\{x,y\}}(\hat{\mathbf{k}})$  are compensated by  $\mathcal{T}_{\{x,y\}}(\hat{\mathbf{k}})$ .

After presenting the general constraints that the filters  $\mathcal{T}_{\{x,y\}}(\hat{\mathbf{k}})$  should obey for equalized power spectra, now we specify the filters and proceed to the analysis for simple polarization fields; that is,  $E_y(\mathbf{r})/E_x(\mathbf{r}) = C \in \mathbb{C}$  for all  $\mathbf{r}$ . If  $C$  equals one, for example, the field is diagonally linearly polarized, or if  $C = j$ , the field is right-hand circularly polarized. As the special cases,  $C$  can be zero or  $\infty$  corresponding to  $x$ -polarized or  $y$ -polarized fields, respectively. The reason for this simple polarization restriction that we choose for the electric fields is, not to create a difference between the power spectra of the  $x$  and  $y$  components of the electric fields. So, the relation between the scalar field and the electric field components becomes simple. Also, this polarization assumption is convenient for many displays and spatial light modulators (SLM) that produce such electromagnetic fields with a simple polarization feature [31–34, 60, 62]. Please note that,

although the assumption that we made on the polarization constraint is the same as the one made in the conventional scalar fields [3, 64, 65], here we assume that the field that we deal with is a wide-angle field so that the longitudinal component cannot be neglected.

In this formulation,  $\mathcal{T}_y(\hat{\mathbf{k}})/\mathcal{T}_x(\hat{\mathbf{k}})$  becomes equal to  $C$ , as well. When  $C \neq \infty$ , using Equation 4.4,  $|\mathcal{T}_x(\hat{\mathbf{k}})|^2$  becomes

$$\begin{aligned} |\mathcal{T}_x(\hat{\mathbf{k}})|^2 &= \begin{cases} \frac{1}{|C|^2+1+|\mathcal{G}_x(\hat{\mathbf{k}})+C\mathcal{G}_y(\hat{\mathbf{k}})|^2} & \text{if } |\hat{\mathbf{k}}| \neq k \\ 0 & \text{otherwise} \end{cases} \\ &= \begin{cases} \frac{k^2-|\hat{\mathbf{k}}|^2}{(k^2-|\hat{\mathbf{k}}|^2)(|C|^2+1)+|k_x+Ck_y|^2} & \text{if } |\hat{\mathbf{k}}| \neq k \\ 0 & \text{otherwise} \end{cases} \end{aligned} \quad (4.8)$$

Therefore,  $\mathcal{T}_x(\hat{\mathbf{k}})$  takes the form

$$\begin{aligned} \mathcal{T}_x(\hat{\mathbf{k}}) &= \begin{cases} \frac{e^{j\theta(\hat{\mathbf{k}})}}{\sqrt{|C|^2+1+|\mathcal{G}_x(\hat{\mathbf{k}})+C\mathcal{G}_y(\hat{\mathbf{k}})|^2}} & \text{if } |\hat{\mathbf{k}}| \neq k \\ 0 & \text{otherwise} \end{cases} \\ &= \begin{cases} \frac{e^{j\theta(\hat{\mathbf{k}})}\sqrt{k^2-|\hat{\mathbf{k}}|^2}}{\sqrt{(k^2-|\hat{\mathbf{k}}|^2)(|C|^2+1)+|k_x+Ck_y|^2}} & \text{if } |\hat{\mathbf{k}}| \neq k \\ 0 & \text{otherwise} \end{cases} \end{aligned} \quad (4.9)$$

Please note that, different choices of the phase factor,  $\theta(\hat{\mathbf{k}})$ , do not violate Equation 4.4. If, for example, the phase of the scalar field and the transverse components of the electric field are desired to be the same, then it can be chosen as zero. Or, if the phase of the scalar field and the  $z$  component is desired to be the same, then it can be chosen as

$$\theta(\hat{\mathbf{k}}) = -\angle\left(\mathcal{G}_x(\hat{\mathbf{k}}) + C\mathcal{G}_y(\hat{\mathbf{k}})\right) \quad (4.10)$$

Equating the phases of the scalar field and the  $z$  component can be useful if the field consists only of plane waves whose propagation angles are large. In this case, as it will be shown below, since  $\mathcal{T}_x(\hat{\mathbf{k}})$  is a lowpass filter, the dominant term in the electric field becomes the  $z$  component. In this respect, the phase patterns of

the scalar field and the dominant term of the electric field can be made equal by choosing  $\theta(\hat{\mathbf{k}})$  as given by Equation 4.10.

When  $C \neq \infty$ ,  $\mathcal{T}_y(\hat{\mathbf{k}})$  can be found as  $C\mathcal{T}_x(\hat{\mathbf{k}})$  using Equation 4.9. If  $C = \infty$ , then  $\mathcal{T}_x(\hat{\mathbf{k}})$  becomes zero and  $\mathcal{T}_y(\hat{\mathbf{k}})$  can be computed as

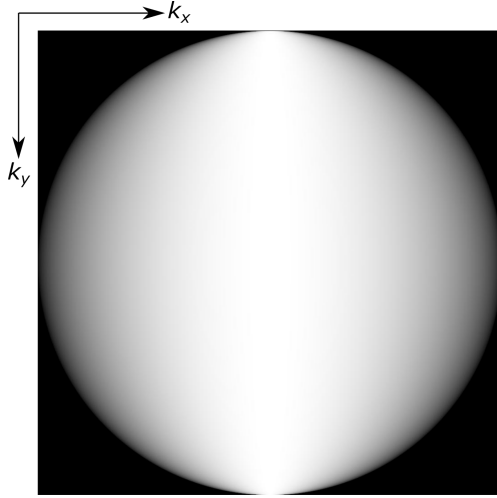
$$\begin{aligned}\mathcal{T}_y(\hat{\mathbf{k}}) &= \begin{cases} \frac{e^{j\theta(\hat{\mathbf{k}})}}{\sqrt{1+|\mathcal{G}_y(\hat{\mathbf{k}})|^2}} & \text{if } |\hat{\mathbf{k}}| \neq k \\ 0 & \text{otherwise} \end{cases} . \\ &= \begin{cases} \frac{e^{j\theta(\hat{\mathbf{k}})}\sqrt{k^2-|\hat{\mathbf{k}}|^2}}{\sqrt{k^2-k_x^2}} & \text{if } |\hat{\mathbf{k}}| \neq k \\ 0 & \text{otherwise} \end{cases} .\end{aligned}\quad (4.11)$$

In this case,  $\theta(\hat{\mathbf{k}})$  can be chosen as

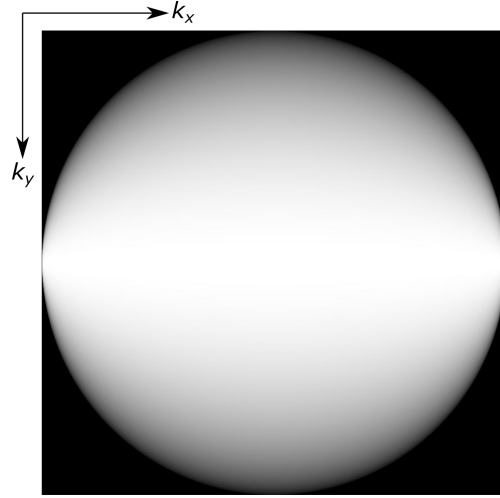
$$\theta(\hat{\mathbf{k}}) = -\angle\mathcal{G}_y(\hat{\mathbf{k}}) \quad , \quad (4.12)$$

if the phases of the scalar field and the  $z$  component are desired to be the same.

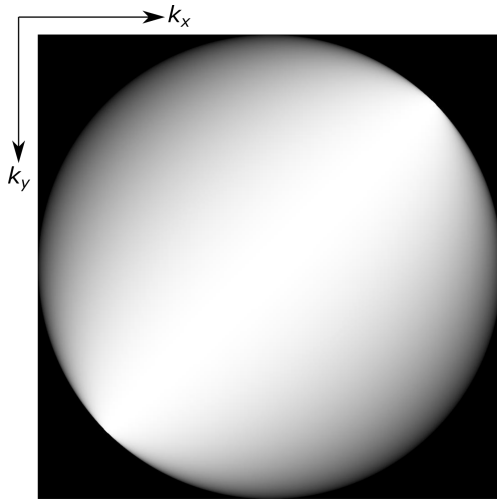
In Figure 4.1, we show the magnitude responses of different  $\mathcal{T}_x(\hat{\mathbf{k}})$  and  $\mathcal{T}_y(\hat{\mathbf{k}})$  pairs based on Equations 4.9 and 4.11 for the propagating fields as grayscale images. From the figures it can be said that all these transfer functions have a lowpass nature. In the linearly polarized cases, shown in Figures 4.1a, 4.1b and 4.1c, the magnitude responses of the corresponding transfer functions are the rotated version of each other. So, it can be shown that, if the electric field has a different linear polarization, i.e.  $C \in \mathbb{R}$ , then, the corresponding transfer functions will be another rotated version where the amount of rotation is determined by  $C$ . Also, in the circularly polarized case, the filter magnitude responses show a circularly symmetric pattern, so it can be said that the orientation characteristics of the scalar wave field is preserved in the resulting  $x$  and  $y$  components of the electric field.



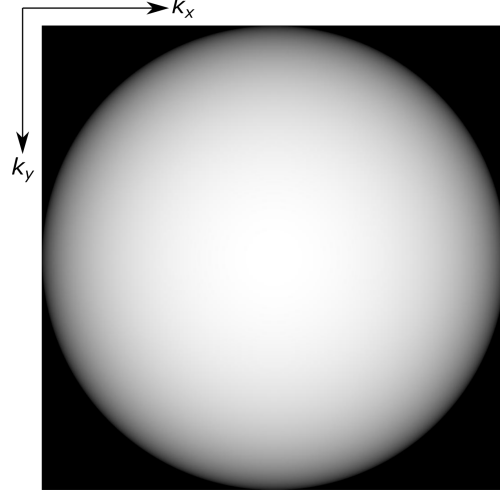
(a) The magnitude of  $\mathcal{T}_x(\hat{\mathbf{k}})$  is shown as the result of Equation 4.9 for the propagating fields when the field is  $x$ -polarized.



(b) The magnitude of  $\mathcal{T}_y(\hat{\mathbf{k}})$  is shown as the result of Equation 4.11 for the propagating fields when the field is  $y$ -polarized.



(c) The magnitude of  $\mathcal{T}_x(\hat{\mathbf{k}}) = \mathcal{T}_y(\hat{\mathbf{k}})$  is shown as the result of Equation 4.9 for the propagating fields when the field is diagonally linearly polarized.



(d) The magnitude of  $\mathcal{T}_x(\hat{\mathbf{k}}) = \pm j \mathcal{T}_y(\hat{\mathbf{k}})$  is shown as the result of Equation 4.9 for the propagating fields when the field is circularly polarized.

Figure 4.1: The magnitude of the corresponding transfer functions which satisfy Equation 4.4 are shown for different polarizations in propagating fields. The centers of the images correspond to  $(k_x, k_y) = (0, 0)$ . (©2018 Springer Nature. Reprinted with permission. Published in [97].)

At the end of the scalar-to-vector wave field mapping, the resulting electric field components in the Fourier domain become

$$\mathcal{E}_x(\hat{\mathbf{k}}) = \begin{cases} \mathcal{S}(\hat{\mathbf{k}}) \mathcal{T}_x(\hat{\mathbf{k}}) & \text{if } C \neq \infty \\ 0 & \text{if } C = \infty \end{cases}, \quad (4.13)$$

$$\mathcal{E}_y(\hat{\mathbf{k}}) = \begin{cases} C\mathcal{S}(\hat{\mathbf{k}}) \mathcal{T}_x(\hat{\mathbf{k}}) & \text{if } C \neq \infty \\ \mathcal{S}(\hat{\mathbf{k}}) \mathcal{T}_y(\hat{\mathbf{k}}) & \text{if } C = \infty \end{cases}, \quad (4.14)$$

$$\mathcal{E}_z(\hat{\mathbf{k}}) = \begin{cases} \mathcal{S}(\hat{\mathbf{k}}) \mathcal{T}_x(\hat{\mathbf{k}}) (\mathcal{G}_x(\hat{\mathbf{k}}) + C\mathcal{G}_y(\hat{\mathbf{k}})) & \text{if } C \neq \infty \\ \mathcal{S}(\hat{\mathbf{k}}) \mathcal{T}_y(\hat{\mathbf{k}}) \mathcal{G}_y(\hat{\mathbf{k}}) & \text{if } C = \infty \end{cases}. \quad (4.15)$$

As a final note to this section, a direct consequence of equalizing the power spectra of the scalar and vector fields in the space domain can be written as

$$\begin{aligned} S(\hat{\mathbf{r}}, z) ** S^*(-\hat{\mathbf{r}}, z) &= E_x(\hat{\mathbf{r}}, z) ** E_x^*(-\hat{\mathbf{r}}, z) + E_y(\hat{\mathbf{r}}, z) ** E_y^*(-\hat{\mathbf{r}}, z) \\ &\quad + E_z(\hat{\mathbf{r}}, z) ** E_z^*(-\hat{\mathbf{r}}, z) \quad . \end{aligned} \quad (4.16)$$

One of the results that can be obtained from Equation 4.16 is

$$\int_{-\infty}^{\infty} |\mathbf{E}(\hat{\mathbf{r}}, z)|^2 d\hat{\mathbf{r}} = \int_{-\infty}^{\infty} |S(\hat{\mathbf{r}}, z)|^2 d\hat{\mathbf{r}} \quad , \quad (4.17)$$

for all  $z$ . Equation 4.17 states that the total powers of the scalar field and the corresponding electric field are always equal at all  $z$  planes. Therefore, it can be said that the spatially average difference between  $|\mathbf{E}(\hat{\mathbf{r}}, z)|^2$  and  $|S(\hat{\mathbf{r}}, z)|^2$  is always zero.

### 4.1.1 Simulation Results

In this section, we present some discrete simulation results in order to compare the performances of the conventional and proposed scalar-to-vector wave field mappings. That is, in the generation of a given scalar field intensity at a  $z$  plane, we show that the proposed technique eliminates some undesired artifacts

arising due to the conventional mapping and ends up with the correct intensity results. In the simulations, we assume that a scalar wave field in space domain is given and the magnitude square of that field is desired to be generated as the electric field intensity pattern. In the conventional case, the scalar wave field is mapped to  $E_{\{x,y\}}(\hat{\mathbf{r}}, 0)$  according to Equation 2.37. For the proposed scalar case, on the other hand,  $E_{\{x,y\}}(\hat{\mathbf{r}}, 0)$  are computed using Equations 4.13 and 4.14 from the given scalar field and the transfer functions,  $\mathcal{T}_{\{x,y\}}(\hat{\mathbf{k}})$ , that are given by Equations 4.9 and 4.11. In both the conventional and proposed scalar fields,  $E_z(\hat{\mathbf{r}}, 0)$  is computed using the  $x$  and  $y$  components of the electric field and the transfer functions,  $\mathcal{G}_{\{x,y\}}(\hat{\mathbf{k}})$ , as given by Equations 2.22 and 2.23

Here we first summarize the steps of the conversion from continuous domain to discrete domain, where the details of this procedure are given in Section 2.1.4. Since we assume that there is no plane wave components when  $|\hat{\mathbf{k}}| \geq k$  in the electromagnetic wave field that we deal with, by choosing the sampling period along both  $x$  and  $y$  directions, which are  $X_s$  and  $Y_s$  respectively, greater than  $\pi/k$ , one can satisfy the Shannon-Nyquist sampling theorem requirements [67]. However, since our aim is to present results which mimic continuous fields, for better illustration, we choose different sampling periods for different simulations.

We assume that the field components take the form  $R(nX_s, mY_s, 0) \equiv \hat{R}[n, m]$ , where  $n$  and  $m$  are integers. Please note that, since all the computations are done for  $z = 0$  plane, we omit this coordinate axis in our notation for the discrete fields. Here  $R(\hat{\mathbf{r}}, 0)$  may represent  $S(\hat{\mathbf{r}}, 0)$  or one of the components of  $\mathbf{E}(\hat{\mathbf{r}}, 0)$ . Please note that we assume that  $\hat{R}[n, m]$  is periodic by  $N \in \mathbb{Z}^+$  and  $M \in \mathbb{Z}^+$  along  $n$  and  $m$  directions, respectively.

We do the field computations in the frequency domain. For this purpose, we use 2D size  $M \times N$  discrete Fourier transform (DFT) and its inverse (IDFT) are

defined as [67],

$$\begin{aligned} DFT_{M \times N} \left\{ \hat{R}[n, m] \right\} &= \hat{\mathcal{R}}[p, q] = \sum_{n=0}^{N-1} \sum_{m=0}^{M-1} \hat{R}[n, m] e^{-j2\pi \left( \frac{pn}{N} + \frac{qm}{M} \right)} \quad , \\ IDFT_{M \times N} \left\{ \hat{\mathcal{R}}[p, q] \right\} &= \hat{R}[n, m] = \frac{1}{NM} \sum_{p=0}^{N-1} \sum_{q=0}^{M-1} \hat{\mathcal{R}}[p, q] e^{j2\pi \left( \frac{pn}{N} + \frac{qm}{M} \right)} \quad , \end{aligned} \quad (4.18)$$

for  $p \in [0, N - 1]$  and  $q \in [0, M - 1]$ .

The transfer functions of the filters in the discrete domain are obtained by first periodically replicating and then sampling the transfer functions of the filters in the continuous domain. That is, we first generate a periodic transfer function,  $\tilde{\mathcal{B}}(\hat{\mathbf{k}})$ , whose one period can be written as,

$$\tilde{\mathcal{B}}(\hat{\mathbf{k}}) = \mathcal{B}(\hat{\mathbf{k}}) \quad (4.19)$$

for  $-\pi/X_s \leq k_x < \pi/X_s$  and  $-\pi/Y_s \leq k_y < \pi/Y_s$ . Here  $\mathcal{B}(\hat{\mathbf{k}})$  may represent  $\mathcal{G}_{\{x,y\}}(\hat{\mathbf{k}})$  or  $\mathcal{T}_{\{x,y\}}(\hat{\mathbf{k}})$ . Then, we obtain the discrete filters as,

$$\hat{\mathcal{B}}[p, q] \Big|_{\substack{p=\hat{p}_{\text{mod}N} \\ q=\hat{q}_{\text{mod}M}}} = \tilde{\mathcal{B}}\left(\frac{2\pi}{NX_s}\hat{p}, \frac{2\pi}{MY_s}\hat{q}\right) \quad , \quad (4.20)$$

where  $\hat{p} \in [-\lceil \frac{N-1}{2} \rceil, \lceil \frac{N}{2} - 1 \rceil]$ ,  $\hat{q} \in [-\lceil \frac{M-1}{2} \rceil, \lceil \frac{M}{2} - 1 \rceil]$ ,  $\lceil \cdot \rceil$  is the ceiling operator which rounds a decimal number to the nearest larger integer.

In the simulations, we begin with a given scalar field  $\hat{S}[n, m]$  and the magnitude square of that scalar field,  $\hat{P}[n, m] = \left| \hat{S}[n, m] \right|^2$ , as the desired electric field intensity pattern. Then, in the conventional scalar mapping, the electric field components are found in the DFT domain as

$$\hat{\mathcal{E}}_{x,con}[p, q] = \frac{1}{\sqrt{1 + |C|^2}} \hat{S}[p, q] \quad , \quad (4.21)$$

$$\hat{\mathcal{E}}_{y,con}[p, q] = \frac{C}{\sqrt{1 + |C|^2}} \hat{S}[p, q] \quad , \quad (4.22)$$

where  $\hat{\mathcal{S}}[p, q] = DFT_{M \times N} \left\{ \hat{S}[n, m] \right\}$ . For the proposed scalar mapping, the field

components are found as

$$\hat{\mathcal{E}}_{x,pro} [p, q] = \begin{cases} \hat{\mathcal{T}}_x [p, q] \hat{\mathcal{S}} [p, q] & \text{if } C \neq \infty \\ 0 & \text{otherwise,} \end{cases} \quad (4.23)$$

$$\hat{\mathcal{E}}_{y,pro} [p, q] = \begin{cases} C \hat{\mathcal{T}}_x [p, q] \hat{\mathcal{S}} [p, q] & \text{if } C \neq \infty \\ \hat{\mathcal{T}}_y [p, q] \hat{\mathcal{S}} [p, q] & \text{otherwise,} \end{cases} \quad (4.24)$$

where  $\hat{\mathcal{T}}_{\{x,y\}} [p, q]$  are computed from  $\mathcal{T}_{\{x,y\}} (\hat{\mathbf{k}})$  by using Equation 4.20. Please note that,  $\mathcal{T}_x (\hat{\mathbf{k}})$  and  $\mathcal{T}_y (\hat{\mathbf{k}})$  are given by Equations 4.9 and 4.11, respectively. Next, the corresponding  $z$  components are computed in the DFT domain as

$$\hat{\mathcal{E}}_{z,con} [p, q] = \hat{\mathcal{G}}_x [p, q] \hat{\mathcal{E}}_{x,con} [p, q] + \hat{\mathcal{G}}_y [p, q] \hat{\mathcal{E}}_{y,con} [p, q] \quad , \quad (4.25)$$

$$\hat{\mathcal{E}}_{z,pro} [p, q] = \hat{\mathcal{G}}_x [p, q] \hat{\mathcal{E}}_{x,pro} [p, q] + \hat{\mathcal{G}}_y [p, q] \hat{\mathcal{E}}_{y,pro} [p, q] \quad , \quad (4.26)$$

where  $\hat{\mathcal{G}}_{\{x,y\}} [p, q]$  are again computed from  $\mathcal{G}_{\{x,y\}} (\hat{\mathbf{k}})$  by using Equation 4.20. Finally, the discrete intensities generated as a result of the conventional and proposed scalar mappings are computed as

$$\hat{P}_{con} [n, m] = \left| IDFT_{M \times N} \left\{ \hat{\mathcal{E}}_{con} [p, q] \right\} \right|^2 \quad , \quad (4.27)$$

$$\hat{P}_{pro} [n, m] = \left| IDFT_{M \times N} \left\{ \hat{\mathcal{E}}_{pro} [p, q] \right\} \right|^2 \quad , \quad (4.28)$$

where  $\hat{\mathcal{E}}_{con} [p, q] = \left[ \hat{\mathcal{E}}_{x,con} [p, q] \quad \hat{\mathcal{E}}_{y,con} [p, q] \quad \hat{\mathcal{E}}_{z,con} [p, q] \right]^T$  and  $\hat{\mathcal{E}}_{pro} [p, q] = \left[ \hat{\mathcal{E}}_{x,pro} [p, q] \quad \hat{\mathcal{E}}_{y,pro} [p, q] \quad \hat{\mathcal{E}}_{z,pro} [p, q] \right]^T$ . The 2D IDFT operations in Equations 4.27 and 4.28 are applied to each component of  $\hat{\mathcal{E}}_{con} [p, q]$  and  $\hat{\mathcal{E}}_{pro} [p, q]$ , separately.

Finally, we compare the three intensity patterns. These are the desired intensity pattern  $\hat{P} [n, m]$ , the pattern generated as the result of conventional scalar-to-vector field mapping,  $\hat{P}_{con} [n, m]$ , and the pattern generated as the result of proposed scalar-to-vector field mapping,  $\hat{P}_{pro} [n, m]$ .

In order to test the effect of the inverse filtering approach, in the first simulation, we choose  $X_s = Y_s = \lambda/2$ , which is the Nyquist rate for the propagating

fields, and a 2D chirp signal as the scalar field for  $N = M = 1024$  as,

$$\hat{S}[n, m] = IDFT_{M \times N} \left\{ DFT_{M \times N} \left\{ \cos \left( \frac{\pi}{N} \left[ \left( n - \frac{N}{2} \right)^2 + \left( m - \frac{M}{2} \right)^2 \right] \right) \right\} Q[p, q] \right\} \quad (4.29)$$

with its magnitude square

$$\hat{P}[n, m] = \left| \hat{S}[n, m] \right|^2, \quad (4.30)$$

where  $Q[p, q]$  matrix,

$$Q[p, q] \Big|_{\substack{p=\hat{p}_{\text{mod}N} \\ q=\hat{q}_{\text{mod}M}}} = \begin{cases} 1 & \text{if } \hat{p}^2/N^2 + \hat{q}^2/M^2 < 1/4 \\ 0 & \text{otherwise} \end{cases}. \quad (4.31)$$

is introduced to remove the evanescent components. Please note that, we choose this test pattern, because its instantaneous normalized frequency includes the full frequency range  $[-\pi, \pi)$  with equal strength. Hence, we are able to test the success of the inverse filter in the reconstruction of all the possible frequency components. The magnitude of the 2D DFT of this field is [89]

$$\left| \hat{\mathcal{S}}[p, q] \right| = N \left| \sin \left( \frac{\pi}{N} (p^2 + q^2) \right) \right| Q[p, q]. \quad (4.32)$$

In Figure 4.2, these patterns given by Equations 4.29, 4.30 and 4.32 are shown. Please note that, in Figure 4.2c the shifted version of  $\left| \hat{\mathcal{S}}[p, q] \right|$  is shown. As a consequence of the shift, the centers of the images correspond to zero frequency and the normalized frequency range extends from  $-N/2$  to  $N/2 - 1$ .

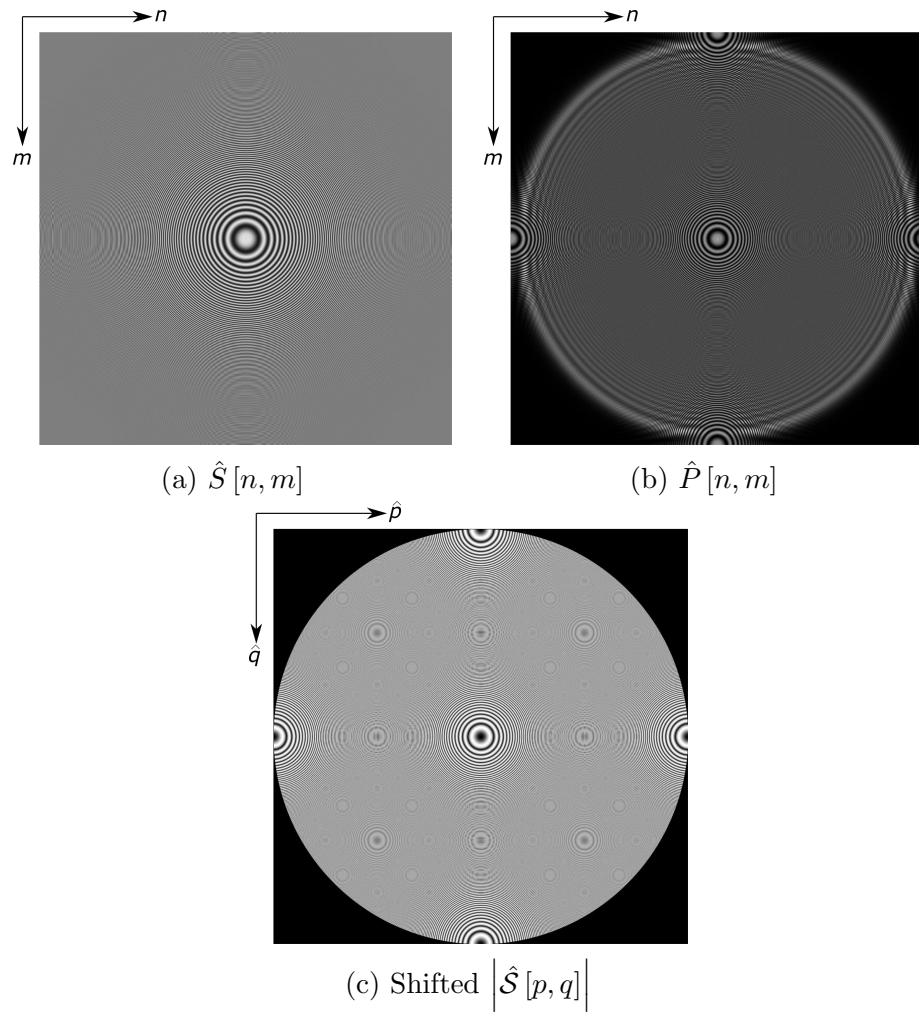
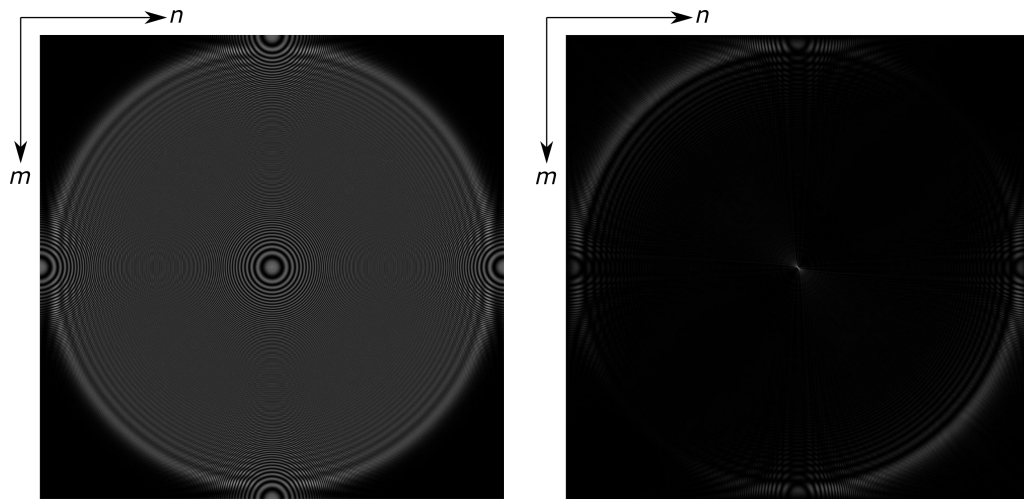


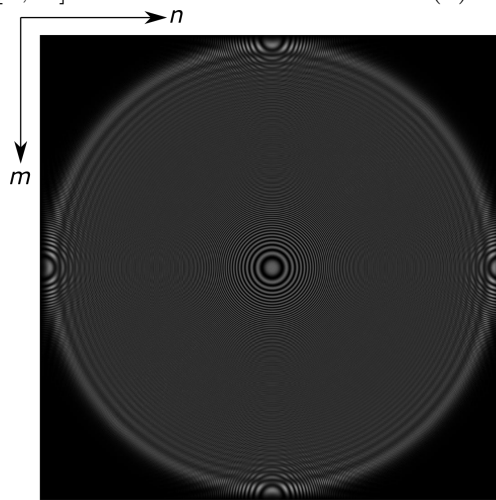
Figure 4.2: The test patterns, which are given by Equations 4.29, 4.30 and 4.32, are shown.  $n$  and  $\hat{p}$  increase from left to right and  $m$  and  $\hat{q}$  increase from top to bottom. The top-left of the images shown in Figures 4.2a and 4.2b correspond to  $(n, m) = (0, 0)$  and the center of the image shown in Figure 4.2c corresponds to  $(\hat{p}, \hat{q}) = (0, 0)$ . (©2018 Springer Nature. Reprinted with permission. Published in [97].)

The reconstructed intensity patterns for the first simulation are shown in Figures 4.3 and 4.4 for  $C = 1$  and  $C = -j$ , respectively. Although it is desirable to show  $\hat{P}[n, m]$ ,  $\hat{P}_{con}[n, m]$  and  $\hat{P}_{pro}[n, m]$  using the same gray scale range for comparison,  $\hat{P}[n, m]$  and  $\hat{P}_{pro}[n, m]$  become invisible due to the dominant high-frequency regions of  $\hat{P}_{con}[n, m]$  when the same grayscale is used; in other words, the conventional method gives a result that is grossly incorrect. So, for the illustration purposes, before jointly scaling the results in gray levels, we linearly shrank the contrast of the grayscale image to get  $\tilde{P}_{con}[n, m]$  from  $\hat{P}_{con}[n, m]$ .  $\hat{P}[n, m]$ ,  $\tilde{P}_{con}[n, m]$ ,  $\hat{P}_{pro}[n, m]$  are shown in Figures 4.3a, 4.3b, 4.3c for  $C = 1$  and in Figures 4.4a, 4.4b, 4.4c for  $C = -j$ . Since it is more informative, we also provide the reconstructed patterns for the conventional case in logarithmic scale in Figures 4.3e and 4.4e. From these figures, it can be said that the intensity pattern that is desired to be reconstructed is completely lost if the conventional procedure is used. Also, the value of  $C$  affects the resulting conventional mapping intensity patterns. In the diagonal linearly polarized case, shown in Figures 4.3b and 4.3e, the reconstructed intensity pattern due to the conventional mapping shows an unequal distribution in high-frequency regions. Such a result occurs due to the constructive and destructive superposition of  $\hat{\mathcal{G}}_x[p, q]$  and  $\hat{\mathcal{G}}_y[p, q]$  in the high-frequency regions. In the left-hand circularly polarized case, shown in Figures 4.4b and 4.4e, these constructive and destructive superpositions end up with a circularly symmetric distribution. On the other hand, due to the proposed mapping, the reconstructed intensity patterns, shown in Figures 4.3c and 4.4c for the jointly scaled cases and in Figures 4.3d and 4.4d for the independently gray-scaled cases, preserve the original intensity pattern. Therefore, the inverse filters  $\hat{\mathcal{T}}_{\{x,y\}}[p, q]$  again compensate the highpass effect of  $\hat{\mathcal{G}}_{\{x,y\}}[p, q]$  for this simulation, as well. Also, for the proposed mapping, there is not much difference between the reconstructed intensity patterns for  $C = j$  and  $C = 1$  cases. Therefore, it can be said that, different values of  $C$  do not affect the resulting intensity pattern and the effect of  $C$  on the reconstructed intensity pattern disappear, through the inverse filters, in these simulations.



(a)  $\hat{P}[n, m]$

(b)  $\tilde{P}_{con}[n, m]$



(c)  $\hat{P}_{pro}[n, m]$

(Continues to the next page)

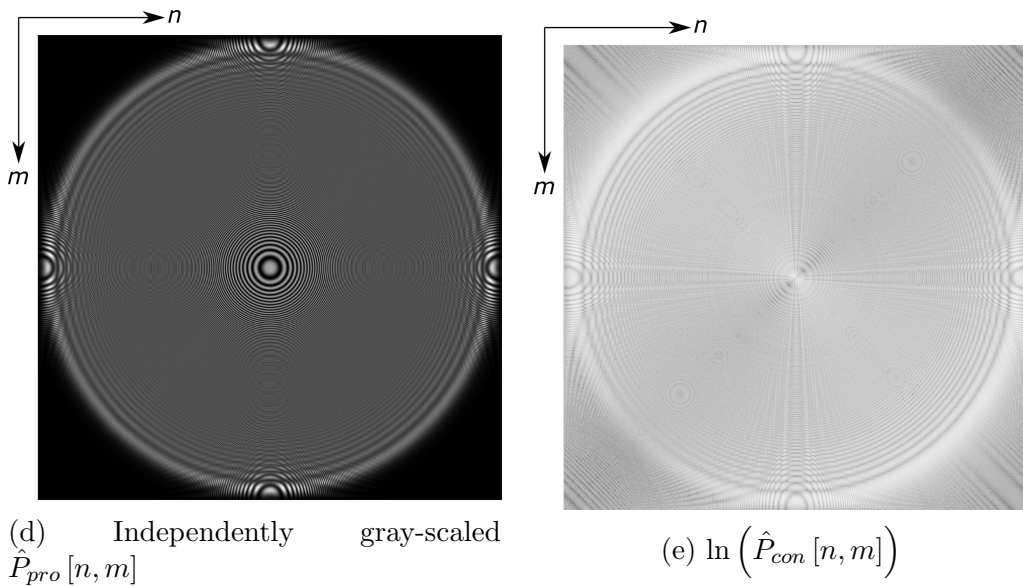
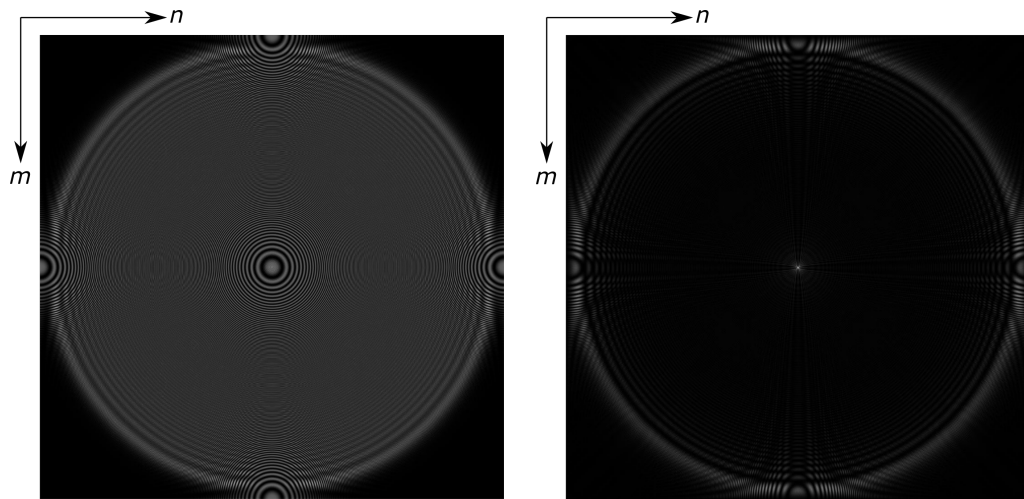
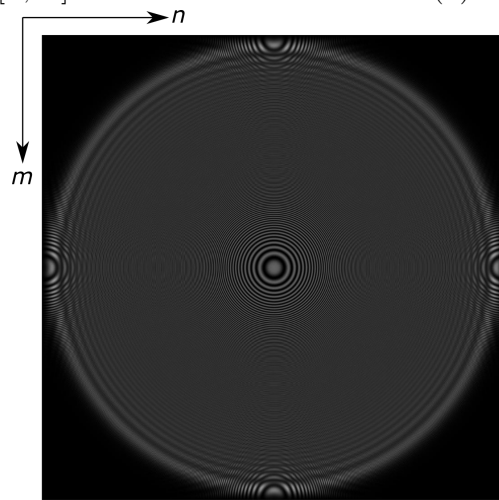


Figure 4.3: (Continues from the previous page) The reconstructed intensity patterns for the first simulation are shown for  $C = 1$ , i.e. diagonally polarized field. The original intensity pattern is shown in Figure 4.3a. The resulting intensity patterns due to the conventional and proposed mappings are shown in Figures 4.3b, and 4.3c, respectively. Before jointly mapping the patterns to the grayscale range, the contrast of  $\hat{P}_{con}[n, m]$  is linearly shrank. Figure 4.3d shows the independently gray-scaled version of Figure 4.3c. Figure 4.3e shows  $\hat{P}_{con}[n, m]$  in the log-scale. The top-left corner of the images correspond to  $(n, m) = (0, 0)$ . (©2018 Springer Nature. Reprinted with permission. Published in [97].)



(a)  $\hat{P}[n, m]$

(b)  $\tilde{P}_{con}[n, m]$



(c)  $\hat{P}_{pro}[n, m]$

(Continues to the next page)

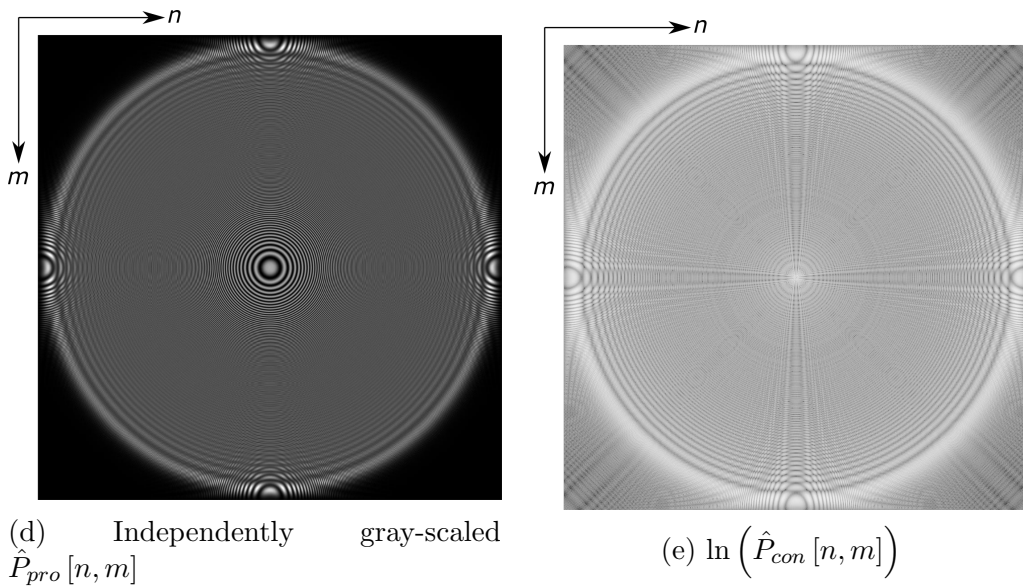
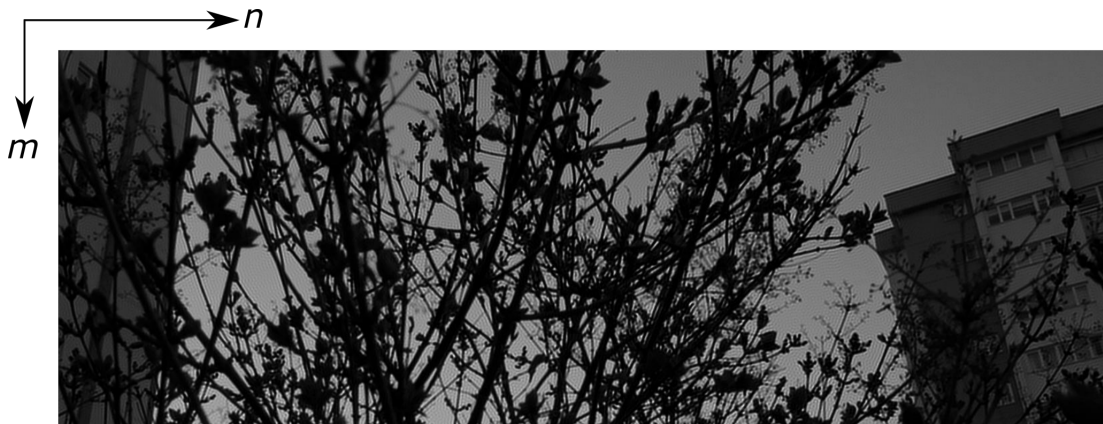


Figure 4.4: (Continues from the previous page) The reconstructed intensity patterns for the first simulation are shown for  $C = -j$ , i.e. left-hand circularly polarized field. The original intensity pattern is shown in Figure 4.4a. The resulting intensity patterns due to the conventional and proposed mappings are shown in Figures 4.4b and 4.4c, respectively. Before jointly mapping the patterns to the grayscale range, the contrast of  $\hat{P}_{con}[n, m]$  is linearly shrank. Figure 4.4d shows the independently gray-scaled version of Figure 4.4c. Figure 4.4e shows  $\hat{P}_{con}[n, m]$  in the log-scale. The top-left corner of the images correspond to  $(n, m) = (0, 0)$ . (©2018 Springer Nature. Reprinted with permission. Published in [97].)

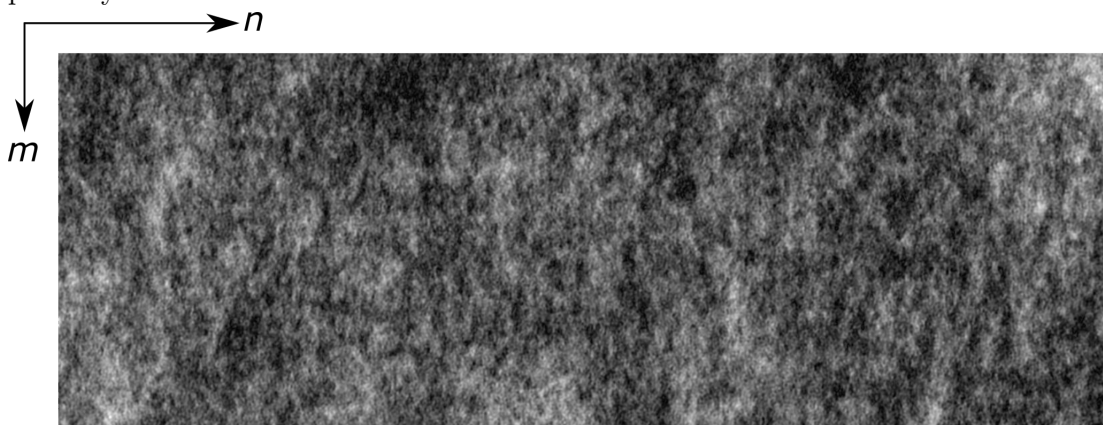
In the second simulation, we test the proposed algorithm for a realistic intensity pattern, as shown in Figure 4.5a. We assume that the scalar field that generates this intensity pattern is zero-phase; so, the scalar field can be found by computing the square root of the given intensity pattern. In this simulation, there are two main differences from the previous simulation. The first one is, the chosen intensity pattern is assumed to be generated using a holographic reconstruction technique. For this purpose, we assume that a SLM which is capable of producing a full complex light field is located at  $z = 0$  plane. Then, the given intensity pattern is desired to be generated by the optical field propagated from this SLM to the image plane located at  $z = 20$  cm away from the SLM plane. Both the size of the intensity pattern and the dimensions of the discrete SLM are taken in this example as  $560 \times 1566$ . The second difference in this simulation is that the sampling rate which is used to convert the analog signals to the discrete signals. When the sampling rate is chosen as  $X_s = Y_s = \lambda/2$ , the spatial continuous frequency  $k$  corresponds to the normalized frequency  $\pi$  rad/sample in the discrete domain. Since such a frequency component ends up with a fast change in the resulting image, the deteriorations due to the conventional mapping cannot be obtained clearly. Moreover, since the rate of change of  $\mathcal{G}_{\{x,y\}}(\hat{\mathbf{k}})$  is large at around  $|\hat{\mathbf{k}}| = k$ , which can be seen from Figure 2.3, the simulation results become significantly dependent on the chosen numerical parameters. That is, the sampling rate and the chosen display size determine whether the frequency components where  $\mathcal{G}_{\{x,y\}}(\hat{\mathbf{k}})$  are large are included in the discrete domain or not. So, in order to show the deteriorations as a relatively low-frequency signal and to include the frequency components where  $\mathcal{G}_{\{x,y\}}(\hat{\mathbf{k}})$  are large, we choose  $X_s = Y_s = \lambda/4.75$  as the sampling rate. As will be shown below, at this sampling rate, the actual continuous field will be simulated according to the expected behavior of the filters and the deterioration due to the conventional mapping will be severe. Please note that, with this sampling rate and the size of the intensity patterns, the actual dimension of the SLM becomes in the order of  $100 \mu\text{m}$ , that is quite small for a realistic application. However, here our aim is to simulate the proposed and conventional mappings over a familiar intensity pattern, that can be encountered frequently in nature, rather than making a computer simulation of a realistic optical setup. We do the simulation for a single polarization case

such that the SLM does not produce the  $y$  component, i.e.  $C = 0$ . Moreover, in order to simulate the free space propagation, we use Rayleigh-Sommerfeld diffraction formula in the 2D DFT domain [91,93] with the wavelength  $\lambda = 500$  nm. As a result, in the conventional mapping, the initial complex valued scalar field is written onto the SLM without making a modification and in the proposed mapping, that scalar field is written onto the SLM after applying the inverse filter.

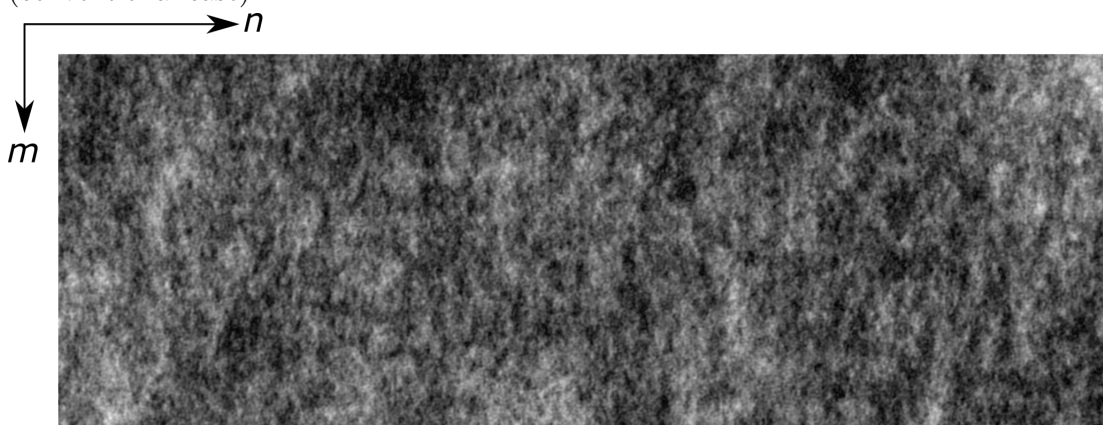
In Figures 4.5b and 4.5c, the magnitudes of the written complex valued scalar fields onto the SLM are shown for the conventional and proposed mappings, respectively, where it is difficult to observe a difference. However, the resulting intensity patterns, reconstructed at the image plane, show a significant difference as shown in Figure 4.6. In Figures 4.6a, 4.6b and 4.6c, the original intensity pattern and the resulting intensity patterns due to the conventional and proposed mappings are shown, respectively. Please note that these three patterns are mapped to the grayscale images using the same scale. Moreover, in Figure 4.6d, the resulting intensity pattern due to the proposed mapping is shown in full grayscale range. Please note that, since the computations are performed in the DFT domain, the shown patterns represent one period of their periodically replicated versions. In the conventional case, the artifacts due to the amplified frequencies can be seen clearly. Due to the branches of the tree and the edges of the buildings, a variation along the horizontal direction, and hence, nonzero frequency components for  $|k_x| \approx k$  occur. As a result of these high frequencies, some periodic patterns from left to right emerges in the conventional case due to the excessive amplification, as shown in Figure 4.6b. However, these artifacts disappear in the intensity patterns when the proposed scalar mapping method is used. Although, there are still some minor differences between the original pattern and the intensity pattern obtained by the proposed method, they look quite similar and the artifacts due to the conventional mapping are clearly eliminated. Therefore, it can be said that the inverse filters compensate the deteriorations which occur when the conventional methods are used.



(a) The intensity pattern that is desired to be holographically generated at the image plane by the SLM

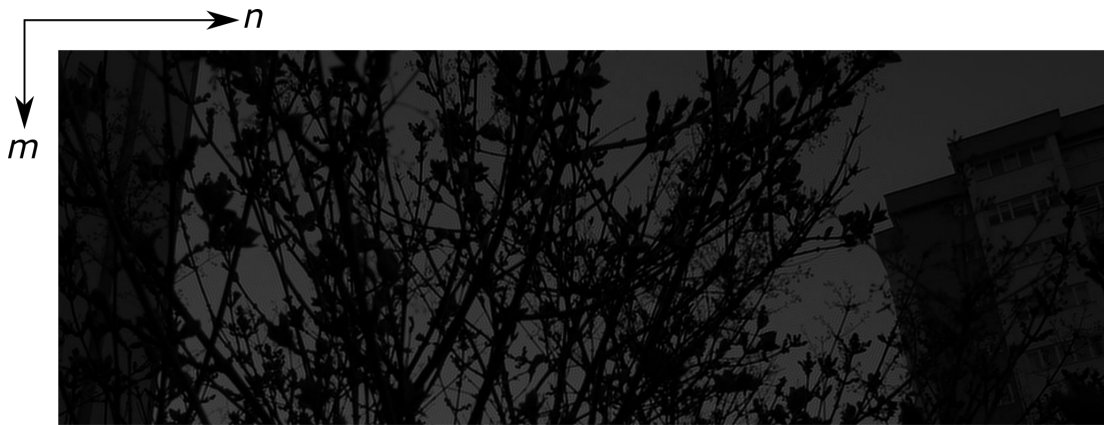


(b) The magnitude of the complex valued scalar field that is written onto the SLM (conventional case)



(c) The magnitude of the complex valued scalar field written onto the SLM (proposed case)

Figure 4.5: The test patterns for the second simulation are shown. The image plane is assumed to be located  $20\text{ cm}$  away from the SLM. Wavelength is  $500\text{ nm}$ . The top-left corner of the images correspond to  $(n, m) = (0, 0)$ . (©2018 Springer Nature. Reprinted with permission. Published in [97].)



(a)  $\hat{P}[n, m]$



(b)  $\hat{P}_{con}[n, m]$

(Continues to the next page)



(c)  $\hat{P}_{pro}[n, m]$



(d) Independently gray-scaled  $\hat{P}_{pro}[n, m]$

Figure 4.6: (Continues from the previous page) The reconstructed intensity patterns are shown for  $C = 0$ , i.e.  $x$ -polarized field. The original intensity pattern shown in Figure 4.5a, and the intensity patterns as the result of the conventional and proposed mappings are shown in Figures 4.6a, 4.6b, and 4.6c, respectively. The patterns shown in these three figures are mapped to gray level images using the same scale. Figure 4.6d shows the independently gray-scaled version of Figure 4.6c. The top-left corner of the images correspond to  $(n, m) = (0, 0)$ . (©2018 Springer Nature. Reprinted with permission. Published in [97].)

## 4.2 Use of the Power Spectrum Equalized Model in a Phase Retrieval Problem

The aim of the phase retrieval algorithms which have been developed for both scalar and vector valued problems is to find a suitable phase pattern such that the resulting complex valued field meets some intensity criterion. In the literature, this criterion generally turns out to be the optical intensity specified over multiple parallel planes for monochromatic scalar optical fields [13–15, 17]. As a result of these algorithms, the computed scalar field may end up with a wide-angle field so the propagation directions of the plane wave components may lie in a large cone. As it is discussed in Chapter 2, the conventional scalar-to-vector field mapping may end up with a large error in the optical intensity due to the neglected longitudinal component. Therefore, in addition to the presented simulation results in previous section, we test the developed power spectrum equalized scalar model in such a phase retrieval problem in this section, which is based on our publication [102].

Please note that, there are some reported research results related to the phase retrieval problem under the scope of the antenna based problems where the longitudinal component of the electric field is taken into account [107–109]. In these algorithms, the intensity criterion is given in terms of the magnitude squares of the scalar components of the vector field. On the other hand, in this section, the intensity is the magnitude square of the electric field vector which is given over multiple parallel planes.

As an overview of the simulations, we first find a scalar field which meets the given intensity criterion using one of the phase retrieval algorithms developed for scalar fields. Then that scalar field is mapped to the vector electric field using Equations 4.13 and 4.14 for the proposed model, and using Equation 2.37 for the conventional model. At the end of these mappings, we compare the scalar field intensity pattern to the generated electric field intensity patterns over the planes where the phase retrieval algorithm is performed. The computations in the discrete domain are carried out using the procedure given in Section 4.1.1.

For the simulation, we take the discrete scalar field at  $z = 0$  plane as a Gaussian function with a random phase,

$$\hat{S}_0[n, m] = e^{-\frac{(n-N/2)^2 + (m-N/2)^2}{2\sigma^2}} e^{j\phi(n, m)} \quad , \quad (4.33)$$

where,  $n \in [0, N - 1]$  and  $m \in [0, N - 1]$  with  $N = 512$ ,  $\sigma = 64$  and  $\phi(n, m)$  is a random number generated from the uniform distribution  $[0, \pi/2]$  indepently for each  $n$  and  $m$ . We compute the field at  $z = d$  plane,  $\hat{S}_d[n, m]$ , for  $d = 20$  cm by using the transfer function of the Rayleigh-Sommerfeld propagation formula in 2D discrete Fourier transform (DFT) domain. We also choose the wavelength of the field as  $500$  nm. So,  $\hat{S}_d[n, m]$  becomes

$$\hat{S}_d[n, m] = IDFT_{N \times N} \left\{ DFT_{N \times N} \{ \hat{S}_0[n, m] \} \hat{F}_z[p, q] \right\} \quad , \quad (4.34)$$

where

$$\hat{F}_z[p, q] \Big|_{\substack{p=\hat{p}_{\text{mod}N} \\ q=\hat{q}_{\text{mod}M}}} = \begin{cases} e^{j2\pi d \sqrt{\frac{1}{\lambda^2} - \frac{\hat{p}^2}{N^2 X_s^2} - \frac{\hat{q}^2}{M^2 Y_s^2}}} & \text{if } \frac{\hat{p}^2}{N^2 X_s^2} + \frac{\hat{q}^2}{M^2 Y_s^2} < \frac{1}{\lambda^2} \\ 0 & \text{otherwise} \end{cases} \quad (4.35)$$

is the transfer function of the Rayleigh-Sommerfeld propagation formula in the 2D DFT domain and  $X_s = Y_s = \lambda/2$ .

The corresponding scalar optical intensities,  $|\hat{S}_0[n, m]|^2 = \hat{P}_0[n, m]$  and  $|\hat{S}_d[n, m]|^2 = \hat{P}_d[n, m]$  which are desired to be generated as the electric field intensities, can be seen in Figures 4.7a and 4.7b, respectively.

Next, by using the Gerchberg-Saxton algorithm [17] and  $\hat{F}_z[p, q]$ , we compute another scalar field pair,  $\tilde{S}_0[n, m]$  and  $\tilde{S}_d[n, m]$ , such that  $|\tilde{S}_0[n, m]|^2 \approx \hat{P}_0[n, m]$  and  $|\tilde{S}_d[n, m]|^2 \approx \hat{P}_d[n, m]$ . As the initial guess for  $\tilde{S}_0[n, m]$  in the Gerchberg-Saxton algorithm, we again assume that its phase is generated from the uniform distribution  $[0, \pi/2]$  indepently. After finding appropriate  $\tilde{S}_0[n, m]$  and  $\tilde{S}_d[n, m]$ , we map them to the  $x$  and  $y$  components of the electric field for  $C = j$ , which corresponds to right hand circularly polarized field, using the conventional method, as described by Equations 4.21 and 4.22, and using the proposed method, as described by Equations 4.23 and 4.24.

Then, the corresponding  $z$  components are computed from the  $x$  and  $y$  components in the discrete domain, as described by Equation 4.25 for the conventional method and by Equation 4.26 for the proposed method.

Finally, for  $z = 0$  and  $z = d$ , we compute the resulting intensities  $\hat{P}_{z,con}[n, m]$  and  $\hat{P}_{z,pro}[n, m]$  that correspond to the conventional and proposed scalar-to-vector mappings, respectively, using Equations 4.27 and 4.28. In Figures 4.7c and 4.7d, the intensities as a result of the conventional mapping and in Figures 4.7e and 4.7f, the intensities as a result of the proposed mappings are presented for  $z = 0$  and  $z = d$  planes. Please note that since we do the computations in DFT domain, the figures represent one period of their corresponding periodic patterns with period  $N_0 = 512$ .

From the figures, it can be seen that the proposed scalar-to-vector mapping outperforms the conventional scalar-to-vector mapping in this phase retrieval problem in terms of the generation of two optical intensity patterns. For the patterns at  $z = 0$  plane, the excessive amplification due to  $\mathcal{G}_{\{x,y\}}(\hat{\mathbf{k}})$  is compensated in the proposed mapping. Also, at both planes, the initial intensity patterns are preserved in the proposed mapping, whereas, in the conventional mapping, some noisy patterns appear.

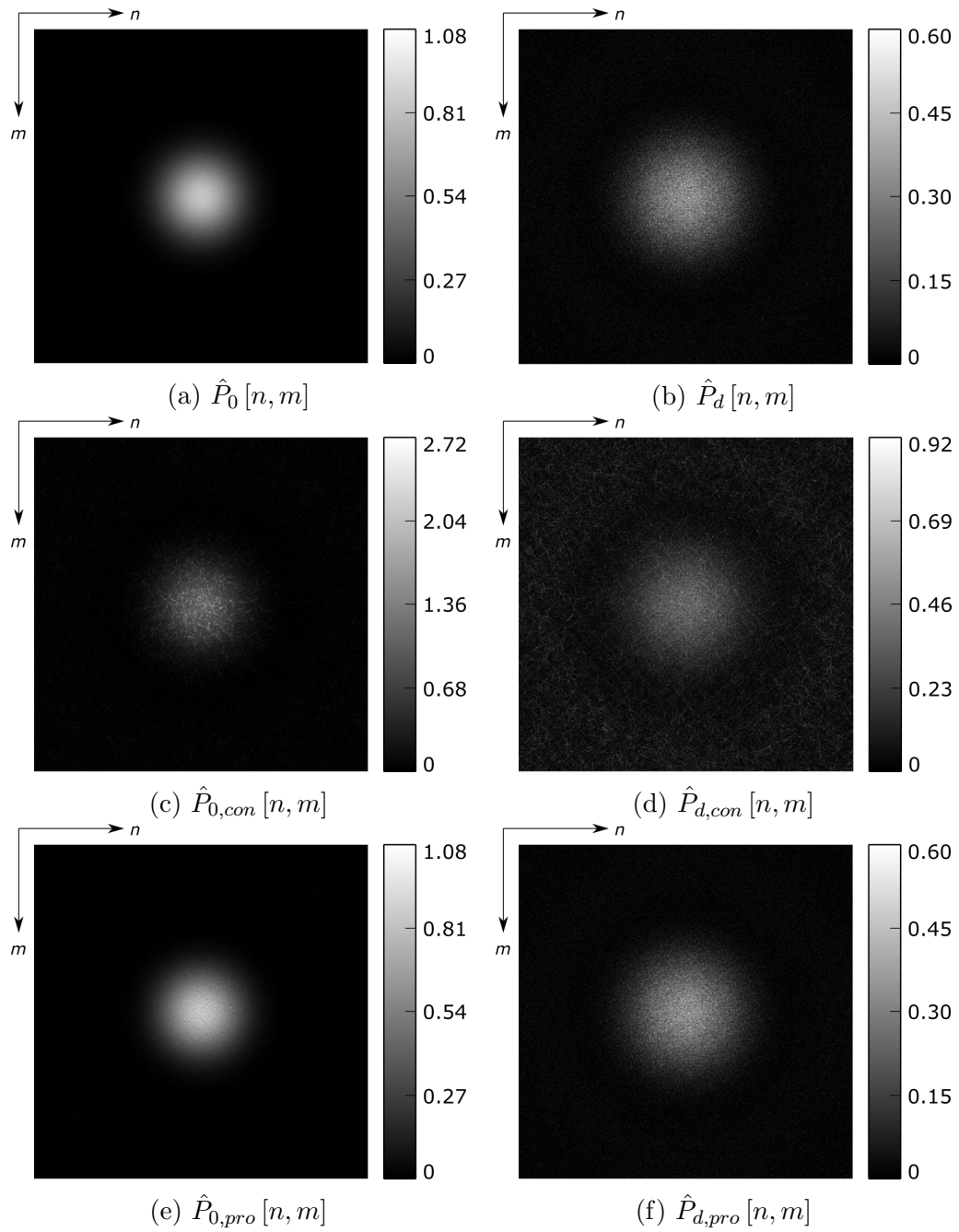


Figure 4.7: The simulation results are shown as gray scale images at  $z = 0$  and  $z = d = 20 \text{ cm}$  for  $N = 512$ . The top-left corners correspond to  $(n, m) = (0, 0)$ ,  $n$  and  $m$  increase from left to right and from top to bottom, respectively. Different gray scales are used in Figures 4.7c and 4.7d, as indicated by the color bars, for the sake of visibility of the underlying Gaussian pattern which is dominated by the amplified random noise due to the uncompensated highpass effect in the conventional procedure. The results indicate that the scalar intensity patterns are preserved if the proposed mapping is applied instead of the conventional mapping. (©2017 OSA. Reprinted with permission. Published in [102].)

## Chapter 5

# Local Polarization-Constrained Scalar-to-Polarized Optical Field Transformation Technique

In this chapter, another method for the scalar-to-vector field mapping is presented. The developed method arises as a special case of the power spectrum equalizing scalar-to-polarized optical field mapping described in Chapter 4. In this case, the filters which are used to generate the electric field components from a given scalar field provides to obtain intended scalar results in wide-viewing-angle holographic displays. In this technique, we assume that an observer which is located at a tilted and rotated plane can capture a locally paraxial segment of the optical field at that plane; this is the case for common imaging sensors [4]. As a result of the imposed polarization constraint, the local paraxial segment of a polarized optical field at a tilted and rotated plane has a simple local polarization property. In this way, it is provided that the physically captured locally paraxial segments at different planes have the same magnitude and phase properties of the corresponding paraxial segments of a given scalar field that are intended to be captured by the observers.

## 5.1 Mapping a Given Scalar Field to a Local Polarization-Constrained Electric Field

In this section, we extend the simple polarization approach to wide-angle fields that is utilized in conventional scalar-to-vector field mapping for paraxial fields. In this approach, the locally paraxial segment of a polarized optical field at a tilted and rotated plane will be imposed to have a simple polarization property. Then, the locally paraxial segments of a given scalar field will be matched to the locally transverse field components of this polarization-constrained electric field.

Here we first define the variables of a rotated coordinate frame,  $\mathbf{r}_{\mathbf{k}} = [x_{\mathbf{k}} \ y_{\mathbf{k}} \ z_{\mathbf{k}}]^T \in \mathbb{R}^3$ , where, this coordinate frame is generated such that the locally longitudinal component along  $z_{\mathbf{k}}$  direction of the plane wave whose propagation direction is implied by  $\mathbf{k}$ , is zero. The relation between  $\mathbf{r}_{\mathbf{k}}$  and  $\mathbf{r}$  can be written as

$$\mathbf{r}_{\mathbf{k}} = \mathbf{K}(\hat{\mathbf{k}}) \mathbf{r} \quad , \quad (5.1)$$

where the rotation matrix  $\mathbf{K}(\hat{\mathbf{k}})$  is in the form

$$\mathbf{K}(\hat{\mathbf{k}}) = \begin{bmatrix} \boldsymbol{\kappa}_{x_{\mathbf{k}}}^T(\hat{\mathbf{k}}) \\ \boldsymbol{\kappa}_{y_{\mathbf{k}}}^T(\hat{\mathbf{k}}) \\ \boldsymbol{\kappa}_{z_{\mathbf{k}}}^T(\hat{\mathbf{k}}) \end{bmatrix} = \begin{bmatrix} \kappa_{11}(\hat{\mathbf{k}}) & \kappa_{12}(\hat{\mathbf{k}}) & \kappa_{13}(\hat{\mathbf{k}}) \\ \kappa_{21}(\hat{\mathbf{k}}) & \kappa_{22}(\hat{\mathbf{k}}) & \kappa_{23}(\hat{\mathbf{k}}) \\ k_x/k & k_y/k & k_z/k \end{bmatrix} \quad . \quad (5.2)$$

The third row of  $\mathbf{K}(\hat{\mathbf{k}})$ , which is  $\boldsymbol{\kappa}_{z_{\mathbf{k}}}^T(\hat{\mathbf{k}})$ , represents the unit vector along the propagation direction of the corresponding plane wave in the global coordinates. The second and third rows,  $\boldsymbol{\kappa}_{x_{\mathbf{k}}}^T(\hat{\mathbf{k}})$  and  $\boldsymbol{\kappa}_{y_{\mathbf{k}}}^T(\hat{\mathbf{k}})$ , are the representations of the unit vectors along the  $x_{\mathbf{k}}$  and  $y_{\mathbf{k}}$ , directions, respectively. The  $x_{\mathbf{k}}-y_{\mathbf{k}}$  plane is the locally transverse plane of the plane wave in the global coordinates and for a given  $\hat{\mathbf{k}}$  there are infinitely many options for  $\boldsymbol{\kappa}_{x_{\mathbf{k}}}(\hat{\mathbf{k}})$  and  $\boldsymbol{\kappa}_{y_{\mathbf{k}}}(\hat{\mathbf{k}})$  to represent such a transverse plane, where each  $\boldsymbol{\kappa}_{x_{\mathbf{k}}}(\hat{\mathbf{k}})$  and  $\boldsymbol{\kappa}_{y_{\mathbf{k}}}(\hat{\mathbf{k}})$  pair which makes  $\mathbf{K}(\hat{\mathbf{k}})$  an appropriate rotation matrix describes a different orientation for  $x_{\mathbf{k}}-y_{\mathbf{k}}$  plane. We are going to discuss the selection method of an appropriate  $\boldsymbol{\kappa}_{x_{\mathbf{k}}}(\hat{\mathbf{k}})$  and  $\boldsymbol{\kappa}_{y_{\mathbf{k}}}(\hat{\mathbf{k}})$

pair for a 3DTV setup in Section 5.4. Also,  $\mathbf{K}$  becomes a function of  $\hat{\mathbf{k}} = [k_x \ k_y]^T$  as it depends on the propagation direction of each plane wave.

Then, in order to compute the amplitude vector of the corresponding plane wave along  $x_{\mathbf{k}}$ ,  $y_{\mathbf{k}}$  and  $z_{\mathbf{k}}$  directions, we compute the projection of  $\boldsymbol{\mathcal{E}}(\hat{\mathbf{k}}) e^{j\mathbf{k}^T \mathbf{r}}$  vector onto these axes as

$$\begin{aligned} \mathbf{K}(\hat{\mathbf{k}}) \begin{bmatrix} \mathcal{E}_x(\hat{\mathbf{k}}) e^{j\mathbf{k}^T \mathbf{r}} \\ \mathcal{E}_y(\hat{\mathbf{k}}) e^{j\mathbf{k}^T \mathbf{r}} \\ \mathcal{E}_z(\hat{\mathbf{k}}) e^{j\mathbf{k}^T \mathbf{r}} \end{bmatrix} &= \mathbf{K}(\hat{\mathbf{k}}) \begin{bmatrix} \mathcal{E}_x(\hat{\mathbf{k}}) \\ \mathcal{E}_y(\hat{\mathbf{k}}) \\ \mathcal{E}_z(\hat{\mathbf{k}}) \end{bmatrix} e^{j\mathbf{k}^T \mathbf{r}} \\ &= \begin{bmatrix} \mathcal{E}_{x_{\mathbf{k}}}(\hat{\mathbf{k}}) \\ \mathcal{E}_{y_{\mathbf{k}}}(\hat{\mathbf{k}}) \\ \mathcal{E}_{z_{\mathbf{k}}}(\hat{\mathbf{k}}) \end{bmatrix} e^{j\mathbf{k}^T \mathbf{r}} = \begin{bmatrix} \mathcal{E}_{x_{\mathbf{k}}}(\hat{\mathbf{k}}) \\ \mathcal{E}_{y_{\mathbf{k}}}(\hat{\mathbf{k}}) \\ 0 \end{bmatrix} e^{j\mathbf{k}^T \mathbf{r}} \quad , \quad (5.3) \end{aligned}$$

where  $\mathbf{K}(\hat{\mathbf{k}})$  behaves as a projection matrix in this case and since  $\mathbf{K}(\hat{\mathbf{k}})$  is generated with the assumption that the locally longitudinal component of the plane wave is zero,  $\mathcal{E}_{z_{\mathbf{k}}}(\hat{\mathbf{k}})$  becomes zero. Please note that the resultant vector wave in Equation 5.3 is still defines the vector field at point  $\mathbf{r}$ , but, the vector coefficient of the corresponding plane wave is decomposed along  $x_{\mathbf{k}}$ ,  $y_{\mathbf{k}}$  and  $z_{\mathbf{k}}$  directions.

The relation between  $\mathcal{E}_{x_{\mathbf{k}}}(\hat{\mathbf{k}})$  and  $\mathcal{E}_{y_{\mathbf{k}}}(\hat{\mathbf{k}})$  in Equation 5.3 determines the local polarization state of this plane wave. So, we impose a local polarization constraint for the electric field generated by a display. This constraint can be written as  $\mathcal{E}_{y_{\mathbf{k}}}(\hat{\mathbf{k}})/\mathcal{E}_{x_{\mathbf{k}}}(\hat{\mathbf{k}}) = C(\hat{\mathbf{k}})$ , where  $C(\hat{\mathbf{k}})$  is a predetermined polarization state function. If  $C(\hat{\mathbf{k}}) = 0$  for a given  $\hat{\mathbf{k}}$ , for example, the field is locally  $x$ -polarized at this spatial frequency, or if  $C(\hat{\mathbf{k}}) = \infty$ , the field is a locally  $y$ -polarized field. Similarly,  $C(\hat{\mathbf{k}}) = j$  and  $C(\hat{\mathbf{k}}) = -j$  correspond to the locally right-hand and locally left-hand circularly polarized fields, respectively.

Then, the locally polarization-constrained electric field is generated from a

given scalar field as

$$\begin{bmatrix} \mathcal{E}_{x\mathbf{k}}(\hat{\mathbf{k}}) \\ \mathcal{E}_{y\mathbf{k}}(\hat{\mathbf{k}}) \end{bmatrix} e^{j\mathbf{k}^T \mathbf{r}} = \frac{1}{\sqrt{1 + |C(\hat{\mathbf{k}})|^2}} \begin{bmatrix} \mathcal{S}(\hat{\mathbf{k}}) \\ C(\hat{\mathbf{k}}) \mathcal{S}(\hat{\mathbf{k}}) \end{bmatrix} e^{j\mathbf{k}^T \mathbf{r}} \quad , \quad (5.4)$$

where the coefficient  $\left(1 + |C(\hat{\mathbf{k}})|^2\right)^{-1/2}$  provides the equality between the power spectra of the scalar and electric fields. Hence the value of  $C(\hat{\mathbf{k}})$  for a given  $\hat{\mathbf{k}}$  does not introduce a bias in the power of the corresponding plane wave. As a result of the transformation given by Equation 5.4, a given scalar field is represented by an electric field whose plane wave components have a simple local polarization state, as opposed to the conventional mapping, where it is assumed that the electric field has a globally simple polarization relation. Moreover, the globally longitudinal component is taken into account in the proposed technique, which is neglected in the conventional mapping.

By using Equations 5.3 and 5.4, the vector components along  $x$  and  $y$  directions in the Fourier domain become

$$\mathcal{E}_x(\hat{\mathbf{k}}) = \frac{\mathcal{S}(\hat{\mathbf{k}}) \left( \kappa_{11}(\hat{\mathbf{k}}) + C(\hat{\mathbf{k}}) \kappa_{21}(\hat{\mathbf{k}}) \right)}{\sqrt{1 + |C(\hat{\mathbf{k}})|^2}} \quad , \quad (5.5)$$

$$\mathcal{E}_y(\hat{\mathbf{k}}) = \frac{\mathcal{S}(\hat{\mathbf{k}}) \left( \kappa_{12}(\hat{\mathbf{k}}) + C(\hat{\mathbf{k}}) \kappa_{22}(\hat{\mathbf{k}}) \right)}{\sqrt{1 + |C(\hat{\mathbf{k}})|^2}} \quad . \quad (5.6)$$

So, the local polarization constraint ends up with the polarization constraint in the global coordinates as

$$C_g(\hat{\mathbf{k}}) = \frac{\mathcal{E}_y(\hat{\mathbf{k}})}{\mathcal{E}_x(\hat{\mathbf{k}})} = \frac{\kappa_{12}(\hat{\mathbf{k}}) + C(\hat{\mathbf{k}}) \kappa_{22}(\hat{\mathbf{k}})}{\kappa_{11}(\hat{\mathbf{k}}) + C(\hat{\mathbf{k}}) \kappa_{21}(\hat{\mathbf{k}})} \quad . \quad (5.7)$$

As a result,  $C(\hat{\mathbf{k}}) = \mathcal{E}_{y\mathbf{k}}(\hat{\mathbf{k}}) / \mathcal{E}_{x\mathbf{k}}(\hat{\mathbf{k}})$  and  $C_g(\hat{\mathbf{k}}) = \mathcal{E}_y(\hat{\mathbf{k}}) / \mathcal{E}_x(\hat{\mathbf{k}})$  give the imposed polarization constraints with respect to the local and global coordinate frames and they are related to each other through Equation 5.7

Next, from the given scalar field, the locally polarization-constrained vector field at  $z = 0$  plane, where the planar display is assumed to be located at this plane, becomes

$$\begin{aligned} \mathbf{E}(\hat{\mathbf{r}}, 0) &= \frac{1}{4\pi^2} \int_P \mathbf{K}^T(\hat{\mathbf{k}}) \left[ \frac{1}{\sqrt{1 + |C(\hat{\mathbf{k}})|^2}} \begin{bmatrix} \mathcal{S}(\hat{\mathbf{k}}) \\ C(\hat{\mathbf{k}}) \mathcal{S}(\hat{\mathbf{k}}) \\ 0 \end{bmatrix} \right] e^{j\hat{\mathbf{k}}^T \hat{\mathbf{r}}} d\hat{\mathbf{k}} \\ &= \frac{1}{4\pi^2} \int_P \frac{\mathcal{S}(\hat{\mathbf{k}})}{\sqrt{1 + |C(\hat{\mathbf{k}})|^2}} \mathbf{K}^T(\hat{\mathbf{k}}) \begin{bmatrix} 1 \\ C(\hat{\mathbf{k}}) \\ 0 \end{bmatrix} e^{j\hat{\mathbf{k}}^T \hat{\mathbf{r}}} d\hat{\mathbf{k}} \quad . \end{aligned} \quad (5.8)$$

where the subscript  $P$  indicates that the integration is taken in the propagation region, that is  $|\hat{\mathbf{k}}| < k$ . It can be shown that the electric field components calculated as in Equation 5.8 satisfy Gauss's law given by Equation 1.31.

The computation of  $E_{\{x,y\}}(\hat{\mathbf{r}}, 0)$  can be interpreted as two different LSI systems in the Fourier domain as

$$\begin{aligned} \mathcal{E}_x(\hat{\mathbf{k}}) &= \mathcal{T}_{x_C}(\hat{\mathbf{k}}) \mathcal{S}(\hat{\mathbf{k}}) \quad , \\ \mathcal{E}_y(\hat{\mathbf{k}}) &= \mathcal{T}_{y_C}(\hat{\mathbf{k}}) \mathcal{S}(\hat{\mathbf{k}}) \quad , \end{aligned} \quad (5.9)$$

where the explicit forms of the transfer functions,  $\mathcal{T}_{x_C}(\hat{\mathbf{k}})$  and  $\mathcal{T}_{y_C}(\hat{\mathbf{k}})$ , are given in Equations 5.5 and 5.6, respectively. It can be shown that these transfer functions are some special cases of the power spectrum equalized filter model developed in Chapter 4. That is,  $\mathcal{T}_{x_C}(\hat{\mathbf{k}})$  and  $\mathcal{T}_{y_C}(\hat{\mathbf{k}})$  satisfy

$$1 = \left| \mathcal{T}_{x_C}(\hat{\mathbf{k}}) \right|^2 + \left| \mathcal{T}_{y_C}(\hat{\mathbf{k}}) \right|^2 + \left| \mathcal{T}_{x_C}(\hat{\mathbf{k}}) \mathcal{G}_x(\hat{\mathbf{k}}) + \mathcal{T}_{y_C}(\hat{\mathbf{k}}) \mathcal{G}_y(\hat{\mathbf{k}}) \right|^2 \quad . \quad (5.10)$$

Moreover, since the scalar-to-polarized optical field transformation is performed through multiplications in the Fourier domain, fast computation of the electric field components can be achieved using the fast Fourier transform (FFT) algorithm [67].

The imposed local polarization constraint given by Equation 5.4 can be seen as a general constraint, where the local polarization depends on the propagation

direction of the plane waves. However, if an observer captures a collection of plane waves rather than a single plane wave, which is common in imaging applications, then, it is more convenient to choose the local polarization state as constant for all the plane waves captured by that observer. Moreover, when locations and viewing angles of observers are not predetermined, then, choosing the local polarization state as constant for all plane waves that form the 3D field is needed. Therefore, for this case, we rewrite Equation 5.8 by making local polarization representation  $C(\hat{\mathbf{k}})$  independent from  $\hat{\mathbf{k}}$  as

$$\begin{aligned}\mathbf{E}(\hat{\mathbf{r}}, 0) &= \frac{1}{4\pi^2} \int_P \frac{\mathcal{S}(\hat{\mathbf{k}})}{\sqrt{1+|C|^2}} \mathbf{K}^T(\hat{\mathbf{k}}) \begin{bmatrix} 1 \\ C \\ 0 \end{bmatrix} e^{j\hat{\mathbf{k}}^T \hat{\mathbf{r}}} d\hat{\mathbf{k}} \\ &= \frac{1}{4\pi^2 \sqrt{1+|C|^2}} \int_P \mathcal{S}(\hat{\mathbf{k}}) \mathbf{K}^T(\hat{\mathbf{k}}) \begin{bmatrix} 1 \\ C \\ 0 \end{bmatrix} e^{j\hat{\mathbf{k}}^T \hat{\mathbf{r}}} d\hat{\mathbf{k}} \quad . \end{aligned} \quad (5.11)$$

So, the 2D FT of the vector field components can be written in the global frequency coordinates as

$$\boldsymbol{\mathcal{E}}(\hat{\mathbf{k}}) = \frac{\mathcal{S}(\hat{\mathbf{k}})}{\sqrt{1+|C|^2}} \mathbf{K}^T(\hat{\mathbf{k}}) \begin{bmatrix} 1 \\ C \\ 0 \end{bmatrix} \quad (5.12)$$

and the polarization constraint with respect to the global coordinates becomes

$$C_g(\hat{\mathbf{k}}) = \frac{\mathcal{E}_y(\hat{\mathbf{k}})}{\mathcal{E}_x(\hat{\mathbf{k}})} = \frac{\kappa_{12}(\hat{\mathbf{k}}) + C\kappa_{22}(\hat{\mathbf{k}})}{\kappa_{11}(\hat{\mathbf{k}}) + C\kappa_{21}(\hat{\mathbf{k}})} \quad . \quad (5.13)$$

The value of  $C$  may not be chosen freely due to some limitations. For example, if a display is able to generate a restricted set of polarized fields, then the choice of  $C$  becomes limited to the values which can be obtained by that set of fields. Or, if the viewers has a polarization selectivity, then,  $C$  should be chosen such that it matches with the preferred polarization state of the viewers.

Even if the local polarization constraint is chosen independent from  $\hat{\mathbf{k}}$ , the globally polarization constraint still depends on the propagation direction of the

corresponding plane wave according to Equation 5.13. For a given viewer,  $V$ , located at a tilted and rotated plane, it is assumed that the captured polarization state represented in the global coordinates become  $C_V = C_g(\hat{\mathbf{k}}_{V_c})$ , where the subscript  $V$  denotes that the orientation of the plane where the given viewer is located is a parameter of the captured polarization state in the global coordinates. Here  $\hat{\mathbf{k}}_{V_c} = [k_{x_{V_c}} \ k_{y_{V_c}}]^T$  is the center spatial frequency of the paraxial segment captured by that viewer and also implies the unit normal of the observation plane, that is equal to  $[k_{x_{V_c}}/k \ k_{y_{V_c}}/k \ k_{z_{V_c}}/k]$  for  $k_{z_{V_c}} = \left(k^2 - k_{x_{V_c}}^2 - k_{y_{V_c}}^2\right)^{1/2}$ . However, in the locally constant polarization case, if  $\boldsymbol{\kappa}_{x_{\mathbf{k}}}(\hat{\mathbf{k}})$  and  $\boldsymbol{\kappa}_{y_{\mathbf{k}}}(\hat{\mathbf{k}})$  are chosen to be continuous and slowly varying functions of  $\hat{\mathbf{k}}$ , where the details of this requirement are discussed in Section 5.3, the polarization state of the captured electric field by an observer becomes almost the same at all points at the observation plane, that is  $E_{y,V}(\mathbf{r}')/E_{x,V}(\mathbf{r}') \approx C_V \in \mathbb{C}$ , where  $\mathbf{r}'$  denotes the set of spatial points which are included in the 2D observation plane of the given viewer. Please note that here  $E_{x,V}(\mathbf{r}')$  and  $E_{y,V}(\mathbf{r}')$  are the globally transverse field components of the electric field vector. It will be also shown that, for such an observer, the locally transverse field components will also have a simple polarization relation. For this purpose and also in order to show that the developed model is suitable for a holographic 3DTV application, we will first formulate the captured electric field by a paraxial field observer located at a tilted and rotated plane in Section 5.2. Then, we will discuss the requirements for the choice of  $\mathbf{K}(\hat{\mathbf{k}})$ 's and for the imaging characteristics of the viewers, such that the generated electric field satisfactorily ends up with the desired scalar results under these requirements in Section 5.3.

## 5.2 Scalar and Electric Fields Recorded by a Viewer Located at an Oblique Angle

In the envisioned holographic 3DTVs, viewers may look at generated ghost image from any angle and at any distance. So, in order to show that the developed electric field model ends up with the desired scalar results at any angle, it is

firstly needed to formulate the scalar field which is intended to be captured and the electric field which is actually captured by a viewer located at a tilted and rotated plane.

Let  $V$  denote a viewer located at a tilted and rotated plane. The normal vector of such a plane, and so the observer located in this plane, can be specified by a pair of angular coordinate variables,  $(\theta, \phi)$ , where  $\theta \in [0, \pi/2]$  and  $\phi \in [0, 2\pi)$  are shown in Figure 5.1.

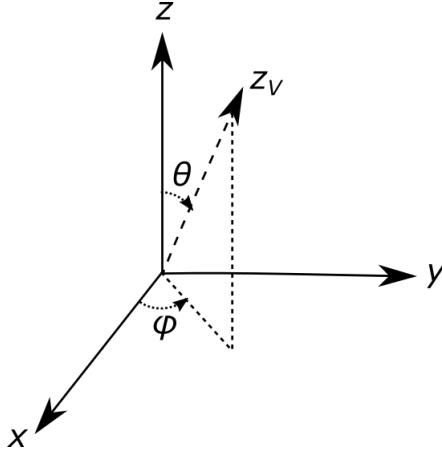


Figure 5.1: The angular variables of a unit normal of a viewer,  $V$ , which is located at a  $z_V = l_V \in \mathbb{R}^+$  plane is shown.

In order to formulate the scalar field which is desired to be recorded by a given  $V$ , we first define a coordinate frame,  $\mathbf{r}_V = [x_V \ y_V \ z_V]^T \in \mathbb{R}^3$ , such that the unit vector of the plane of observation lies on the  $z_V$  axis. In other words, the observation plane of  $V$  is a  $z_V = l_V \in \mathbb{R}^+$  plane. Let  $\mathbf{r}_{z_V}$  denote the unit vector along  $z_V$  axis in the global coordinates. Then, the relation between  $\mathbf{r}_V$  and  $\mathbf{r}$  can be written as

$$\mathbf{r}_V = \mathbf{R}_V \mathbf{r} \quad , \quad (5.14)$$

where  $\mathbf{R}_V$  is a  $3 \times 3$  rotation matrix in the form

$$\mathbf{R}_V = \begin{bmatrix} \mathbf{r}_{x_V}^T \\ \mathbf{r}_{y_V}^T \\ \mathbf{r}_{z_V}^T \end{bmatrix} = \begin{bmatrix} r_{11V} & r_{12V} & r_{13V} \\ r_{21V} & r_{22V} & r_{23V} \\ r_{31V} & r_{32V} & r_{33V} \end{bmatrix} . \quad (5.15)$$

As being for  $\mathbf{K}(\hat{\mathbf{k}})$  matrices, in this case, the orientation of the locally transverse,  $x_V$ - $y_V$ , plane can be chosen as desired, as well. Hence, there are infinitely many options for the choice of  $\mathbf{r}_{x_V}$  and  $\mathbf{r}_{y_V}$  vectors which make  $\mathbf{R}_V$  a proper rotation matrix.

Then, we express a given scalar field,  $S(\mathbf{r})$ , in the local coordinate frame associated with  $V$  as [91–96]

$$\begin{aligned}
S(\mathbf{r}) &= S(\mathbf{R}_V^T \mathbf{r}_V) \\
&= \frac{1}{4\pi^2} \int_P \mathcal{S}(\hat{\mathbf{k}}) e^{j\mathbf{k}^T(\mathbf{R}_V^T \mathbf{r}_V)} d\hat{\mathbf{k}} \\
&= \frac{1}{4\pi^2} \int_P \mathcal{S}(\hat{\mathbf{k}}) e^{j(\mathbf{R}_V \mathbf{k})^T \mathbf{r}_V} d\hat{\mathbf{k}} \\
&= \frac{1}{4\pi^2} \int_{P_V} \mathcal{S}(\hat{\mathbf{R}}_V^T \mathbf{k}_V) e^{j\mathbf{k}_V^T \mathbf{r}_V} \left| \frac{r_{13_V} k_{x_V} + r_{23_V} k_{y_V} + r_{33_V} k_{z_V}}{k_{z_V}} \right| d\hat{\mathbf{k}}_V \quad , \quad (5.16)
\end{aligned}$$

where  $\mathbf{R}_V \mathbf{k} = \mathbf{k}_V = [k_{x_V} \ k_{y_V} \ k_{z_V}]^T$ ,  $\hat{\mathbf{k}}_V = [k_{x_V} \ k_{y_V}]^T$  and

$$\hat{\mathbf{R}}_V = \begin{bmatrix} r_{11_V} & r_{12_V} \\ r_{21_V} & r_{22_V} \\ r_{31_V} & r_{32_V} \end{bmatrix} \quad . \quad (5.17)$$

$P_V$  denotes the region of the values of  $\hat{\mathbf{k}}_V$  where the integral is computed. The term  $|r_{13_V} k_{x_V} + r_{23_V} k_{y_V} + r_{33_V} k_{z_V}|/|k_{z_V}|$  is the Jacobian term that appears due to the coordinate rotation and arises during the change of variable from  $d\hat{\mathbf{k}}$  to  $d\hat{\mathbf{k}}_V$ .

For this rotated coordinate frame,  $\hat{\mathbf{k}}_V = [0 \ 0]^T$  denotes the lowest local spatial frequency, i.e. DC component of the scalar field captured by  $V$ . In other words, the plane wave component whose local spatial frequency variables are  $(k_{x_V}, k_{y_V}) = (0, 0)$  is the plane wave which directly propagates towards the observation plane of the viewer,  $V$ . If this viewer records a locally paraxial segment of the incoming plane waves, it captures the plane wave components whose local spatial frequencies are near the neighborhood of the plane wave whose local spatial frequencies are  $(k_{x_V}, k_{y_V}) = (0, 0)$ . This operation can be analytically

formulated as a lowpass filter in the Fourier domain, where the passband of the filter includes the frequency range  $|\hat{\mathbf{k}}_V| \geq k_c$ , where  $0 < k_c \ll k$ , with the center frequency  $(k_{x_V}, k_{y_V}) = (0, 0)$ . So, the recorded scalar field by  $V$ , which is denoted as  $S_V(\mathbf{R}_V^T \mathbf{r}_V)$ , can be written as

$$\begin{aligned}
S_V \left( \mathbf{R}_V^T \begin{bmatrix} x_V \\ y_V \\ l_V \end{bmatrix} \right) &= \frac{1}{4\pi^2} \int_{P_V} \mathcal{S}(\hat{\mathbf{R}}_V^T \mathbf{k}_V) \mathcal{L}(\hat{\mathbf{k}}_V) e^{jk_{z_V} l_V} e^{j\hat{\mathbf{k}}_V^T \hat{\mathbf{r}}_V} \\
&\times \left| \frac{r_{13_V} k_{x_V} + r_{23_V} k_{y_V} + r_{33_V} k_{z_V}}{k_{z_V}} \right| d\hat{\mathbf{k}}_V \quad , \\
&= \frac{1}{4\pi^2} \int_{P_V} \mathcal{S}_V(\hat{\mathbf{R}}_V^T \mathbf{k}_V) e^{jk_{z_V} l_V} e^{j\hat{\mathbf{k}}_V^T \hat{\mathbf{r}}_V} \\
&\times \left| \frac{r_{13_V} k_{x_V} + r_{23_V} k_{y_V} + r_{33_V} k_{z_V}}{k_{z_V}} \right| d\hat{\mathbf{k}}_V \quad , \quad (5.18)
\end{aligned}$$

where  $\mathcal{L}(\cdot, \cdot)$  is a 2D narrowband lowpass filter with the cutoff frequency  $k_c$  for  $0 < |k_c| \ll k$  and  $\mathcal{S}_V(\hat{\mathbf{R}}_V^T \mathbf{k}_V) = \mathcal{S}(\hat{\mathbf{R}}_V^T \mathbf{k}_V) \mathcal{L}(\hat{\mathbf{k}}_V)$ . Please note that, here we assume that all the viewers which can be located at different angles have the same bandwidth. In this respect, we do not insert a subscript  $V$  in the notation of  $\mathcal{L}(\cdot, \cdot)$ . In the literature, this lowpass filter is generally assumed to have a circular or rectangular band [4]. However, in some cases, apodization can be applied to reduce the ringing artifacts that arise due to a sharp-edge lowpass filter [4]. Please note that, in order not to complicate the formulation and notations, we assume a lensless imaging device as the viewer. Therefore, the positive or negative magnification introduced by a thin lens is not included. However, if needed, it is straightforward to modify the formulation if a lens is present [4].

Although  $\mathcal{L}(\hat{\mathbf{k}}_V)$  is defined as a lowpass filter in  $\hat{\mathbf{k}}_V$  domain, and blocks locally high-frequency components, due to the coordinate rotation in the 3D spatial frequency domain, this lowpass filter behaves as a bandpass filter in the global spatial frequency coordinates, which is  $\hat{\mathbf{k}}$  domain. We denote this bandpass filter as  $\mathcal{L}_V(\hat{\mathbf{k}})$  in the global coordinate space and is related to  $\mathcal{L}(\hat{\mathbf{k}}_V)$  as

$$\mathcal{L}(\hat{\mathbf{k}}_V) = \mathcal{L}(\tilde{\mathbf{R}}_V \mathbf{k}) = \mathcal{L}_V(\hat{\mathbf{k}}) \quad , \quad (5.19)$$

where  $\tilde{\mathbf{R}}_V = [\mathbf{r}_{x_V} \ \mathbf{r}_{y_V}]^T$ . Please note that, since the passband region of the bandpass filter,  $\mathcal{L}_V(\hat{\mathbf{k}})$ , depends on the location of the observer,  $V$ , we insert the parameter  $V$  as a subscript in this case. For a given  $V$ , both  $\mathcal{L}(\hat{\mathbf{k}}_V)$  and  $\mathcal{L}_V(\hat{\mathbf{k}})$  are different representations of the same operation applied on a given 3D scalar field in local and global 2D transverse coordinates, respectively. That is, by applying this filter, a viewer captures a paraxial segment of the 3D field from different observation angles. However, since the projection of the passband region of this 3D filter to the 2D  $\hat{\mathbf{k}}$  and  $\hat{\mathbf{k}}_V$  domains cover different parts of these 2D frequency planes, the bandwidth of the lowpass filter,  $\mathcal{L}(\hat{\mathbf{k}}_V)$ , in  $\hat{\mathbf{k}}_V$  domain becomes larger than the bandwidth of the corresponding bandpass filter,  $\mathcal{L}_V(\hat{\mathbf{k}})$ , in  $\hat{\mathbf{k}}$  domain.

In Figure 5.2, a simple drawing, which includes the projections of the passband of a filter to the both global and local spatial frequency domains, is shown. For the sake of a simpler illustration, the figure does not include  $k_x$  and  $k_{x_V}$  axes. In the figure, the dashed semi-circle indicates the  $(k_y, k_z)$  pairs such that  $k_y^2 + k_z^2 = k^2$  for positive-valued  $k_z$ 's. Hence, this semi-circle is the set of frequency points in the global frequency variables that can physically exist in the 3D space. The thick arc drawn on this semi-circle is the passband of a narrowband filter. Therefore, this arc implies that the applied filter captures the paraxial segment associated with the frequency locations in the frequency plane. This filter behaves as a lowpass filter in local  $[k_{y_V} \ k_{z_V}]^T$  domain and its projection to  $k_{y_V}$  axis includes  $-k_c/2 < k_{y_V} < k_c/2$ . On the other hand, the filter becomes a bandpass filter in the global frequency coordinates,  $[k_y \ k_z]^T$  domain. The projection of the passband of the filter to  $k_y$  axis cover the interval  $k_2 < k_y < k_1$ . From this figure, it is seen that,  $k_c > |k_1 - k_2|$  and hence, the bandwidth in  $k_{y_V}$  domain is larger than the bandwidth in  $k_y$  domain. In other words, the bandwidth of the narrowband lowpass filter is larger than the bandwidth of the corresponding bandpass filter.

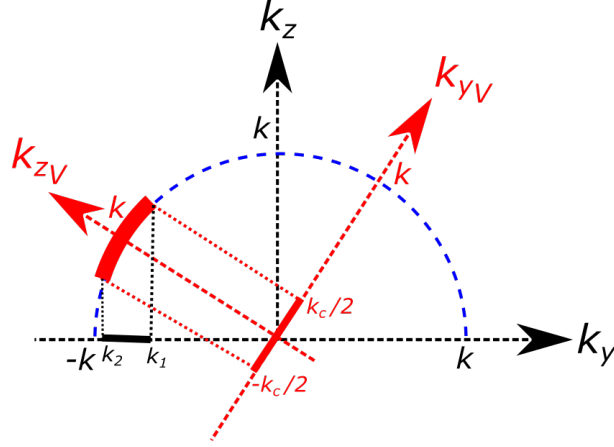


Figure 5.2: The projections of the passband of a filter, that is shown as a red thick arc, to both local and global spatial frequency domains are shown. For simplicity, the illustration includes a 2D frequency domain associated with a 2D space, by omitting the  $k_x$  and  $k_{x_V}$  axes. The projection of the passband region onto the global frequency axis includes the frequency interval  $k_2 < k_y < k_1$  and the projection onto the local frequency axis includes the interval  $-k_c/2 < k_{y_V} < k_c/2$ . It can be seen that the bandwidth in the local frequency axis is larger than the bandwidth in the global frequency axis. That is,  $k_c > |k_1 - k_2|$ .

As a result,  $\mathcal{S}_V \left( \hat{\mathbf{R}}_V^T \mathbf{k}_V \right)$ , as given by Equation 5.18, is related to the 2D FT of the scalar field which is intended to be captured by an observer located at a tilted and rotated plane for a 3D scalar field whose 2D FT at  $z = 0$  plane is given as  $\mathcal{S} \left( \hat{\mathbf{k}} \right)$ . Therefore,  $\mathcal{S}_V \left( \hat{\mathbf{R}}_V^T \mathbf{k}_V \right)$  completely specifies the scalar field which is desired to be captured by  $V$ . In the global coordinates, the same field can be written as

$$\mathcal{S}_V \left( \hat{\mathbf{R}}_V^T \mathbf{k}_V \right) = \mathcal{S} \left( \hat{\mathbf{R}}_V^T \mathbf{k}_V \right) \mathcal{L} \left( \hat{\mathbf{k}}_V \right) = \mathcal{S} \left( \hat{\mathbf{k}} \right) \mathcal{L}_V \left( \hat{\mathbf{k}} \right) = \mathcal{S}_V \left( \hat{\mathbf{k}} \right) \quad . \quad (5.20)$$

Now, we present the electric field recorded by an observer located at an oblique angle. This field can be regarded as the actual and physical field recorded by the viewer,  $V$ . Since each electric field component behaves as a separate scalar wave field and propagates according to the scalar diffraction theory, these components

in the local coordinate frame can be written similar to Equation 5.18, as [76]:

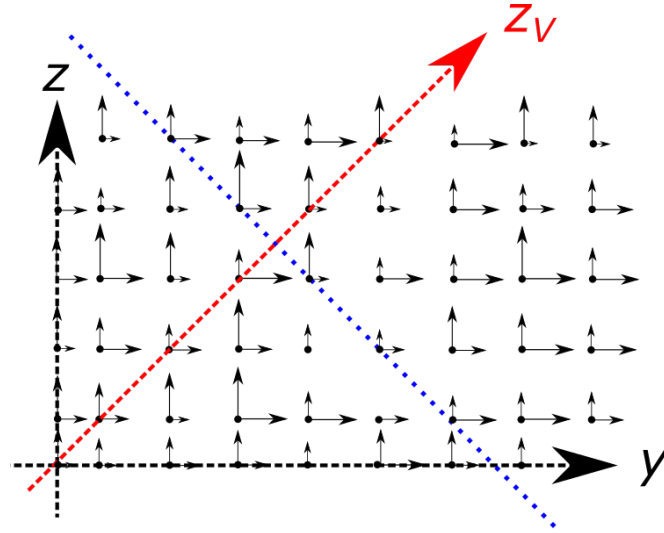
$$\begin{aligned}
\mathbf{E}(\mathbf{r}) &= \mathbf{E}(\mathbf{R}_V^T \mathbf{r}_V) \\
&= \frac{1}{4\pi^2} \int_P \boldsymbol{\mathcal{E}}(\hat{\mathbf{k}}) e^{j\mathbf{k}^T(\mathbf{R}_V^T \mathbf{r}_V)} d\hat{\mathbf{k}} \\
&= \frac{1}{4\pi^2} \int_P \boldsymbol{\mathcal{E}}(\hat{\mathbf{k}}) e^{j(\mathbf{R}_V \mathbf{k})^T \mathbf{r}_V} d\hat{\mathbf{k}} \\
&= \frac{1}{4\pi^2} \int_{P_V} \boldsymbol{\mathcal{E}}(\hat{\mathbf{R}}_V^T \mathbf{k}_V) e^{j\mathbf{k}_V^T \mathbf{r}_V} \left| \frac{r_{13_V} k_{x_V} + r_{23_V} k_{y_V} + r_{33_V} k_{z_V}}{k_{z_V}} \right| d\hat{\mathbf{k}}_V \quad . \quad (5.21)
\end{aligned}$$

Here,  $\mathbf{E}(\mathbf{R}_V^T \mathbf{r}_V)$  represents the electric field vector at point  $\mathbf{R}_V^T \mathbf{r}_V$ , but the vector is decomposed along the unit vectors of the axes of the global coordinates, i.e.  $x$ ,  $y$  and  $z$  directions. Therefore,  $x$  and  $y$  components of  $\mathbf{E}(\mathbf{R}_V^T \mathbf{r}_V)$  represent the globally transverse field components at point  $\mathbf{R}_V^T \mathbf{r}_V$  and its  $z$  component represents the globally longitudinal component. In Figure 5.3a, we show an example collection of electric field vectors whose scalar components are decomposed along the global  $y$  and  $z$  directions. For simplicity,  $x$ -axis is excluded and the figure is shown for a 2D space. In the figure, the cross-section at a  $z_V$  plane is shown as the dotted line.

Next, in order to compute that locally transverse and longitudinal components of the electric field with respect to the location of the viewer,  $V$ , we compute the projection of  $\mathbf{E}(\mathbf{R}_V^T \mathbf{r}_V)$  onto the unit vectors of the  $x_V$ ,  $y_V$  and  $z_V$  axes by using  $\mathbf{R}_V$  as

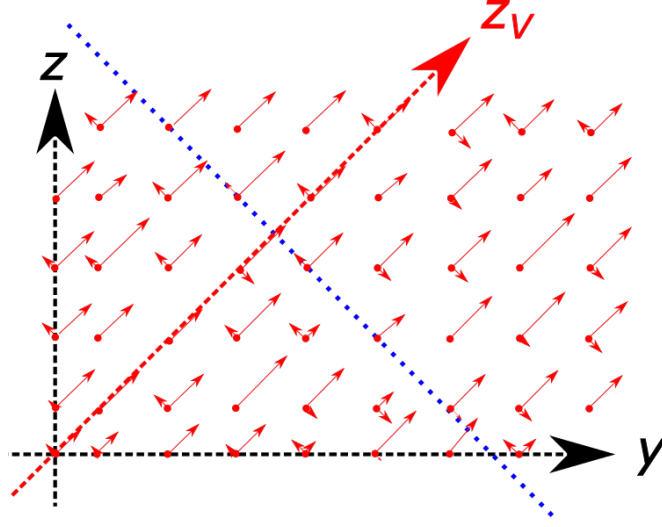
$$\begin{aligned}
\tilde{\mathbf{E}}(\mathbf{R}_V^T \mathbf{r}_V) &= \mathbf{R}_V \mathbf{E}(\mathbf{R}_V^T \mathbf{r}_V) \\
&= \frac{1}{4\pi^2} \mathbf{R}_V \left[ \int_{P_V} \boldsymbol{\mathcal{E}}(\hat{\mathbf{R}}_V^T \mathbf{k}_V) e^{j\mathbf{k}_V^T \mathbf{r}_V} \left| \frac{r_{13_V} k_{x_V} + r_{23_V} k_{y_V} + r_{33_V} k_{z_V}}{k_{z_V}} \right| d\hat{\mathbf{k}}_V \right] \\
&= \frac{1}{4\pi^2} \int_{P_V} \mathbf{R}_V \left[ \boldsymbol{\mathcal{E}}(\hat{\mathbf{R}}_V^T \mathbf{k}_V) e^{j\mathbf{k}_V^T \mathbf{r}_V} \left| \frac{r_{13_V} k_{x_V} + r_{23_V} k_{y_V} + r_{33_V} k_{z_V}}{k_{z_V}} \right| \right] d\hat{\mathbf{k}}_V \\
&= \frac{1}{4\pi^2} \int_{P_V} \left[ \mathbf{R}_V \boldsymbol{\mathcal{E}}(\hat{\mathbf{R}}_V^T \mathbf{k}_V) \right] e^{j\mathbf{k}_V^T \mathbf{r}_V} \left| \frac{r_{13_V} k_{x_V} + r_{23_V} k_{y_V} + r_{33_V} k_{z_V}}{k_{z_V}} \right| d\hat{\mathbf{k}}_V \quad . \quad (5.22)
\end{aligned}$$

Here, the electric field vector,  $\tilde{\mathbf{E}}(\mathbf{R}_V^T \mathbf{r}_V) = \left[ \tilde{E}_x(\mathbf{R}_V^T \mathbf{r}_V) \quad \tilde{E}_y(\mathbf{R}_V^T \mathbf{r}_V) \quad \tilde{E}_z(\mathbf{R}_V^T \mathbf{r}_V) \right]^T$ , represents a vector at a point  $\mathbf{R}_V^T \mathbf{r}_V$  whose scalar components are the projections onto the unit vector along the coordinate axes along  $x_V$ ,  $y_V$  and  $z_V$  directions. Therefore,  $\tilde{E}_x(\mathbf{R}_V^T \mathbf{r}_V)$  and  $\tilde{E}_y(\mathbf{R}_V^T \mathbf{r}_V)$  become the locally transverse field components and  $\tilde{E}_z(\mathbf{R}_V^T \mathbf{r}_V)$  become the locally longitudinal component with respect to the viewer,  $V$ . In Figure 5.3b, the projections of the vectors shown in Figure 5.3a onto the  $x_V$ ,  $y_V$  and  $z_V$  directions are shown. It can also be seen from the figure that, in the rotated coordinates,  $\tilde{E}_y(\mathbf{R}_V^T \mathbf{r}_V)$  becomes the locally transverse field component, and  $\tilde{E}_z(\mathbf{R}_V^T \mathbf{r}_V)$  becomes the locally longitudinal component.



(a) A sample  $\mathbf{E}(\mathbf{R}_V^T \mathbf{r}_V)$ 's, whose components are decomposed along the global  $y$  and  $z$  directions, are shown. The components along the  $y$  direction are the global transverse field and the components along the  $z$  direction are the global longitudinal field components.

(Continues to the next page)



(b) A sample  $\tilde{\mathbf{E}}(\mathbf{R}_V^T \mathbf{r}_V) = \mathbf{R}_V \mathbf{E}(\mathbf{R}_V^T \mathbf{r}_V)$ 's, whose components are decomposed along the local  $y_V$  and  $z_V$  directions, are shown. The components along the  $y_V$  direction are the local transverse field and the components along the  $z_V$  direction are the local longitudinal field components.

Figure 5.3: (Continues from the previous page) A sample collection of electric field vectors are shown in a 2D space ( $x$  and  $x_V$  axes are omitted). The dotted line in both figures indicates the 2D cross-section of the field at a  $z_V$  plane. For simplicity,  $y_V$  coordinate axis is not shown. The sum of the vector components at each point are the same in both figures. However, their decomposition along different coordinate axes become different in two figures.

When the lowpass filter associated with the viewer located at  $z_V = l_V$  plane is applied to the electric field components, the recorded field components,  $\mathbf{E}_V(\mathbf{R}_V^T \mathbf{r}_V) = [E_{x_V, V}(\mathbf{R}_V^T \mathbf{r}_V) \ E_{y_V, V}(\mathbf{R}_V^T \mathbf{r}_V) \ E_{z_V, V}(\mathbf{R}_V^T \mathbf{r}_V)]^T$ , become

$$\begin{aligned}
\mathbf{E}_V \left( \mathbf{R}_V^T \begin{bmatrix} x_V \\ y_V \\ l_V \end{bmatrix} \right) &= \frac{1}{4\pi^2} \int_{P_V} \mathbf{R}_V \mathcal{E}(\hat{\mathbf{R}}_V^T \mathbf{k}_V) \mathcal{L}(\hat{\mathbf{k}}_V) e^{jk_{z_V} l_V} e^{j\hat{\mathbf{k}}_V^T \hat{\mathbf{r}}_V} \\
&\times \left| \frac{r_{13_V} k_{x_V} + r_{23_V} k_{y_V} + r_{33_V} k_{z_V}}{k_{z_V}} \right| d\hat{\mathbf{k}}_V \\
&= \frac{1}{4\pi^2} \int_{P_V} \mathcal{E}_V(\hat{\mathbf{R}}_V^T \mathbf{k}_V) e^{jk_{z_V} l_V} e^{j\hat{\mathbf{k}}_V^T \hat{\mathbf{r}}_V} \\
&\times \left| \frac{r_{13_V} k_{x_V} + r_{23_V} k_{y_V} + r_{33_V} k_{z_V}}{k_{z_V}} \right| d\hat{\mathbf{k}}_V \quad . \quad (5.23)
\end{aligned}$$

So, the term  $\boldsymbol{\mathcal{E}}_V \left( \hat{\mathbf{R}}_V^T \mathbf{k}_V \right)$  in Equation 5.23 is related to the amplitudes of the plane wave components of the vector field which are captured by the viewer,  $V$ , and specifies the physically captured polarized optical field. In the global frequency variables, the same vector field can be written as

$$\boldsymbol{\mathcal{E}}_V \left( \hat{\mathbf{R}}_V^T \mathbf{k}_V \right) = \mathbf{R}_V \boldsymbol{\mathcal{E}} \left( \hat{\mathbf{R}}_V^T \mathbf{k}_V \right) \mathcal{L} \left( \hat{\mathbf{k}}_V \right) = \mathbf{R}_V \boldsymbol{\mathcal{E}} \left( \hat{\mathbf{k}} \right) \mathcal{L}_V \left( \hat{\mathbf{k}} \right) = \boldsymbol{\mathcal{E}}_V \left( \hat{\mathbf{k}} \right) \quad . \quad (5.24)$$

Please note that, although  $\boldsymbol{\mathcal{E}}_V \left( \hat{\mathbf{k}} \right)$  is expressed in the global spatial frequency variables, it represents the 2D FT of the electric field vector whose components are decomposed along the unit vectors of the coordinate axes of the  $\mathbf{r}_V$  domain.

In order to find the relation between the given scalar field and the actually captured electric field, we replace  $\boldsymbol{\mathcal{E}} \left( \hat{\mathbf{k}} \right)$  in Equation 5.24 by the electric field model developed using the given scalar field as given by Equation 5.12 and write the captured electric field in the global spatial frequency variables as

$$\begin{aligned} \boldsymbol{\mathcal{E}}_V \left( \hat{\mathbf{k}} \right) &= \frac{\mathcal{S} \left( \hat{\mathbf{k}} \right)}{\sqrt{1 + |C|^2}} \mathcal{L}_V \left( \hat{\mathbf{k}} \right) \mathbf{R}_V \mathbf{K}^T \left( \hat{\mathbf{k}} \right) \begin{bmatrix} 1 \\ C \\ 0 \end{bmatrix} \\ &= \frac{\mathcal{S}_V \left( \hat{\mathbf{k}} \right)}{\sqrt{1 + |C|^2}} \mathbf{R}_V \mathbf{K}^T \left( \hat{\mathbf{k}} \right) \begin{bmatrix} 1 \\ C \\ 0 \end{bmatrix} \quad . \end{aligned} \quad (5.25)$$

So far, we have represented the desired scalar field and the actual vector field captured by a viewer.  $\mathcal{S}_V \left( \hat{\mathbf{k}} \right)$  is given by Equation 5.20 and the actually captured electric field,  $\boldsymbol{\mathcal{E}}_V \left( \hat{\mathbf{k}} \right)$ , is given by Equation 5.25. For any  $V$ , it is desired that, the magnitude and the individual phase values of the scalar components of  $\boldsymbol{\mathcal{E}}_V \left( \hat{\mathbf{k}} \right)$  are the same as the magnitude and the phase of  $\mathcal{S}_V \left( \hat{\mathbf{k}} \right)$ . Similar to the the paraxial fields, this can be achieved if the locally longitudinal component of  $\boldsymbol{\mathcal{E}}_V \left( \hat{\mathbf{k}} \right)$ , which is  $\mathcal{E}_{z_V, V} \left( \hat{\mathbf{k}} \right)$ , becomes negligibly small and the locally transverse field components have a simple polarization relation. In this case, intended scalar results can be realized at any tilted and rotated plane. These results also include the equivalence of the magnitude squares of the scalar and vector fields for intensity imaging,

which is common. In the following section, we are going to discuss the cases where the prescribed scalar results can be obtained through the actual polarized vector fields which are generated according to Equation 5.25.

### 5.3 Conditions for a Satisfactory Reconstruction of a Given Scalar Field by the Local Polarization-Constrained Electric Field

If the relation between  $\mathcal{S}_V(\hat{\mathbf{k}})$  and  $\boldsymbol{\mathcal{E}}_V(\hat{\mathbf{k}})$  could be written for all  $V$  and  $\hat{\mathbf{k}}$  such that

$$\boldsymbol{\mathcal{E}}_V(\hat{\mathbf{k}}) = \frac{\mathcal{S}_V(\hat{\mathbf{k}})}{\sqrt{1 + |C|^2}} \begin{bmatrix} 1 \\ C \\ 0 \end{bmatrix} . \quad (5.26)$$

then, in terms of the magnitude and phase of the scalar field, a perfect matching between  $\mathcal{S}_V(\hat{\mathbf{k}})$  and  $\boldsymbol{\mathcal{E}}_V(\hat{\mathbf{k}})$  can be achieved. Equation 5.26 is satisfied if the equality, which is derived from Equation 5.25,

$$\mathbf{R}_V \mathbf{K}^T(\hat{\mathbf{k}}) \mathcal{L}_V(\hat{\mathbf{k}}) = \mathbf{I}_{3 \times 3} \mathcal{L}_V(\hat{\mathbf{k}}) \quad (5.27)$$

holds for all  $\hat{\mathbf{k}}$ , where  $\mathbf{I}_{3 \times 3}$  is the  $3 \times 3$  identity matrix. However, the matrix elements of  $\mathbf{R}_V$  associated with a given  $V$  are constant whereas the matrix elements of  $\mathbf{K}(\hat{\mathbf{k}})$  are varying functions of  $\hat{\mathbf{k}}$ . So, Equation 5.27 is satisfied for all  $\hat{\mathbf{k}}$  only when  $\mathcal{L}(\hat{\mathbf{k}}_V)$  is chosen as

$$\mathcal{L}(\hat{\mathbf{k}}_V) = \delta(\hat{\mathbf{k}}_V) , \quad (5.28)$$

where  $\delta(\cdot, \cdot)$  is the 2D impulse function [4]. In this case, since  $\mathcal{L}(\hat{\mathbf{k}}_V) = 0$  except for  $\hat{\mathbf{k}}_V = [0 \ 0]^T$ , both sides of Equation 5.27 become identically zero when  $\hat{\mathbf{k}}_V \neq [0 \ 0]^T$ . The physical implication of this filtering operation is, an arbitrary viewer  $V$  is restricted to capture only the DC component of the incoming plane

waves, i.e. the plane wave which propagates directly towards the viewer. In the global frequency variables, the corresponding bandpass filter becomes

$$\mathcal{L}_V(\hat{\mathbf{k}}) = \delta(k_x - r_{31_V}k, k_y - r_{32_V}k) \quad . \quad (5.29)$$

Equation 5.29 is obtained as follows. The 3D local frequency variables which make  $\delta(\hat{\mathbf{k}}_V)$  nonzero are  $\mathbf{k}_V = [0 \ 0 \ k]^T$ . In the global coordinates, the corresponding spatial frequency becomes

$$\mathbf{R}_V^T \begin{bmatrix} 0 \\ 0 \\ k \end{bmatrix} = \begin{bmatrix} r_{31_V}k \\ r_{32_V}k \\ r_{33_V}k \end{bmatrix} \quad . \quad (5.30)$$

So, in the global coordinates, the frequency variables which are allowed to pass through the filter are  $\hat{\mathbf{k}} = [r_{31_V}k \ r_{32_V}k]^T$ . So, this condition leads to Equation 5.29 in representing the associated bandpass filter in the global frequency domain.

By inserting Equation 5.29 into Equation 5.27, we obtain

$$\begin{aligned} \mathbf{R}_V \mathbf{K}^T(\hat{\mathbf{k}}) \delta(k_x - r_{31_V}k, k_y - r_{32_V}k) = \\ \mathbf{R}_V \mathbf{K}^T(r_{31_V}k, r_{32_V}k) \delta(k_x - r_{31_V}k, k_y - r_{32_V}k) = \mathbf{I}_{3 \times 3} \delta(k_x - r_{31_V}k, k_y - r_{32_V}k) \quad . \end{aligned} \quad (5.31)$$

Here, the 3<sup>rd</sup> rows of  $\mathbf{R}_V$  and  $\mathbf{K}(r_{31_V}k, r_{32_V}k)$ , which are  $\mathbf{r}_{z_V}^T$  and  $\boldsymbol{\kappa}_{z_k}^T(r_{31_V}k, r_{32_V}k)$ , respectively, become necessarily equal, as they both indicate the unit vector of  $z_V$  axis or the propagation direction of the plane wave which directly propagates towards the  $z_V = l_V$  plane. In addition this, although the orientations of the respective transversal planes, which are determined by  $\mathbf{r}_{x_V}$  and  $\mathbf{r}_{y_V}$  for  $\mathbf{R}_V$  and  $\boldsymbol{\kappa}_{x_k}(r_{31_V}k, r_{32_V}k)$  and  $\boldsymbol{\kappa}_{y_k}(r_{31_V}k, r_{32_V}k)$  for  $\mathbf{K}(r_{31_V}k, r_{32_V}k)$ , can be chosen independently from each other, since our aim is to satisfy that  $\mathbf{R}_V \mathbf{K}^T(\hat{\mathbf{k}}) \delta(k_x - r_{31_V}k, k_y - r_{32_V}k) = \mathbf{I}_{3 \times 3}$ , we assume that the orientation of the transversal planes are chosen equal, that is  $\mathbf{r}_{x_V} = \boldsymbol{\kappa}_{x_k}(r_{31_V}k, r_{32_V}k)$  and  $\mathbf{r}_{y_V} = \boldsymbol{\kappa}_{y_k}(r_{31_V}k, r_{32_V}k)$ . This choice implies that the local orientation of the observation plane of the viewer and the local orientation of the local transverse plane of the captured plane wave are the same. Therefore, the intended scalar results and the specified polarization state can be achieved for such a viewer, which capture only the locally DC component in its local coordinates.

Although, the assumption that a viewer is restricted to capture only the DC component of the incoming wave field is not realistic and not desirable for common holographic 3DTV applications, the developments that have been made so far will be useful for more generic imaging sensors, which capture a paraxial collection of plane waves rather than a single plane wave. In order to consider such cases,  $\mathcal{L}(\hat{\mathbf{k}}_V)$  can be assumed as a narrowband lowpass filter. As an example, we take such a filter which has a circular passband as

$$\mathcal{L}(\hat{\mathbf{k}}_V) = \begin{cases} 1 & \text{if } |\hat{\mathbf{k}}_V|^2 < k_c^2 \\ 0 & \text{otherwise} \end{cases} \quad (5.32)$$

for a given  $k_c$  such that  $0 < |k_c| \ll k$ . The associated bandpass filter can be written as

$$\mathcal{L}_V(\hat{\mathbf{k}}) = \begin{cases} 1 & \text{if } (\mathbf{r}_{x_V}^T \mathbf{k})^2 + (\mathbf{r}_{y_V}^T \mathbf{k})^2 < k_c^2 \\ 0 & \text{otherwise} \end{cases} \quad (5.33)$$

As it is discussed in Section 5.2 and shown in Figure 5.2,  $\mathcal{L}_V(\hat{\mathbf{k}})$  has a narrow passband around  $k_x = r_{31_V}k$  and  $k_y = r_{32_V}k$ , which is the frequency variable of the locally DC component represented in the global frequencies. In this respect, it can be said that, the propagation directions of the plane waves which lie within the passband of  $\mathcal{L}_V(\hat{\mathbf{k}})$  do not deviate significantly from the propagation direction of the plane wave whose spatial frequency is  $k_x = r_{31}k$  and  $k_y = r_{32}k$ . Since the propagation directions of the plane waves do not change significantly within the passband, the locally transverse planes of the plane waves which fall to the passband region do not change significantly, as well. Therefore, if the individual local transverse coordinate directions of each plane wave, which are determined by  $\boldsymbol{\kappa}_{x_{\mathbf{k}}}(\hat{\mathbf{k}})$  and  $\boldsymbol{\kappa}_{y_{\mathbf{k}}}(\hat{\mathbf{k}})$ , can be chosen close enough to each other, then, the orientations of the local transverse planes of these plane waves which fall to the passband become almost the same, as well. The closeness conditions can be achieved if the elements of  $\boldsymbol{\kappa}_{x_{\mathbf{k}}}(\hat{\mathbf{k}})$  and  $\boldsymbol{\kappa}_{y_{\mathbf{k}}}(\hat{\mathbf{k}})$  vectors are generated as continuous functions of  $\hat{\mathbf{k}}$  and vary slowly as  $\hat{\mathbf{k}}$  changes.

Hereupon, in order to compute the approximation error which arises due to

the variation in the local transverse plane of each plane wave, the error measure,

$$\epsilon_V(\hat{\mathbf{k}}) = \mathcal{L}_V(\hat{\mathbf{k}}) \left\| \mathbf{R}_V \mathbf{K}^T(\hat{\mathbf{k}}) - \mathbf{I}_{3 \times 3} \right\|_2, \quad (5.34)$$

which is derived from Equation 5.27 can be used. This quantitative error measure also indicates the success of the developed electric field model on the representation of a given scalar field and is required to be small for all  $\hat{\mathbf{k}}$ s for a satisfactory representation. Here,  $\|\cdot\|$  is the matrix  $l_2$ -norm [110].

If the bandwidth of the lowpass filter, that is related to  $k_c$ , increases, the radius of the cone of the light beams which are captured by  $V$  increases. In other words, for large values of  $k_c$ , both the differences between the propagation directions of the plane waves which fall to the passband region and the difference between the propagation direction of the plane waves whose locally spatial frequencies are near  $k_c$  and the unit normal of the plane at which  $V$  is located increase. In this case, the difference between the orientations of the local transverse planes of the plane waves which fall to the passband region becomes large even if  $\kappa_{x_{\mathbf{k}}}(\hat{\mathbf{k}})$  and  $\kappa_{y_{\mathbf{k}}}(\hat{\mathbf{k}})$  are chosen slowly varying functions of  $\hat{\mathbf{k}}$ . As a result, for the values of  $\hat{\mathbf{k}}$ 's which are close to the cutoff frequencies of the bandpass filter,  $\epsilon_V(\hat{\mathbf{k}})$  becomes also large especially for the large values of  $k_c$ . Therefore, the desired scalar results may not be obtained for viewers whose associated lowpass filter has a large bandwidth. On the other hand, if the bandwidth of  $\mathcal{L}(\hat{\mathbf{k}}_V)$  is large, then the paraxial approximations, which are used in the analysis of many imaging devices [3,4], may not hold. Therefore, it can be loosely said that, the model that we developed in this chapter is valid as long as the paraxial approximations are valid for the imaging formulations of the viewers.

In summary, two conditions should be met to observe the desired scalar results through polarized optical fields generated according to the electric field model proposed in Equation 5.11. Firstly,  $\kappa_{x_{\mathbf{k}}}(\hat{\mathbf{k}})$  and  $\kappa_{y_{\mathbf{k}}}(\hat{\mathbf{k}})$  should be chosen as slowly varying functions of  $\hat{\mathbf{k}}$ . Secondly, the bandwidth of the lowpass  $\mathcal{L}(\hat{\mathbf{k}}_V)$  associated with a viewer should be small enough to satisfy the paraxial imaging formulations.

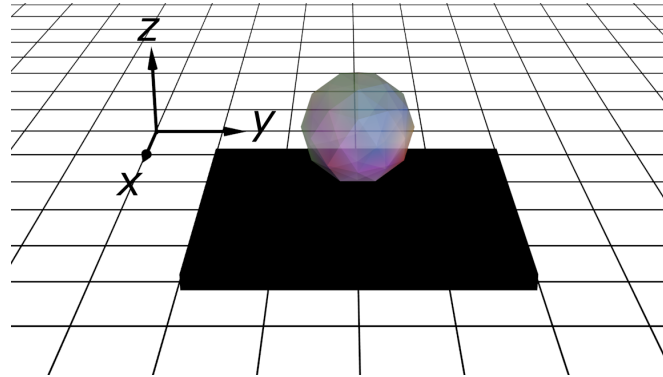
Please note that, the choice of  $\kappa_{x_{\mathbf{k}}}(\hat{\mathbf{k}})$  and  $\kappa_{y_{\mathbf{k}}}(\hat{\mathbf{k}})$  is not arbitrary; only the

ones which form an orthonormal basis with  $\boldsymbol{\kappa}_{z_{\mathbf{k}}}(\hat{\mathbf{k}})$  are in the set of options. We will describe the computation steps of  $\boldsymbol{\kappa}_{x_{\mathbf{k}}}(\hat{\mathbf{k}})$  and  $\boldsymbol{\kappa}_{y_{\mathbf{k}}}(\hat{\mathbf{k}})$  from a given  $\boldsymbol{\kappa}_{z_{\mathbf{k}}}(\hat{\mathbf{k}})$  for a realistic holographic display setup in the following section.

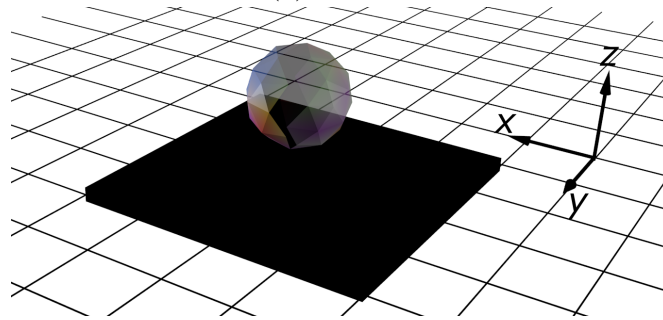
## 5.4 Design of Rotation Matrices Applicable to a Table-top Holographic Display Configuration

For a holographic 3DTV application, the matrices,  $\mathbf{R}_V$  and  $\mathbf{K}(\hat{\mathbf{k}})$ 's, should be chosen such that  $\epsilon_V(\hat{\mathbf{k}})$  becomes small for all  $\hat{\mathbf{k}}$ , where general constraints to achieve this aim was discussed in the previous section. The physical geometry of the optical setup, capabilities of the display to be used or the orientations and the polarization selectivity characteristics of the viewers may impose further restrictions on the choice of the rotation matrices,  $\mathbf{R}_V$  and  $\mathbf{K}(\hat{\mathbf{k}})$ 's. In this respect, we are going to describe the computation steps of  $\mathbf{K}(\hat{\mathbf{k}})$  matrices from the propagation direction  $\mathbf{k}$ , where the resulting  $\mathbf{K}(\hat{\mathbf{k}})$ 's are appropriate to use in table-top displays.

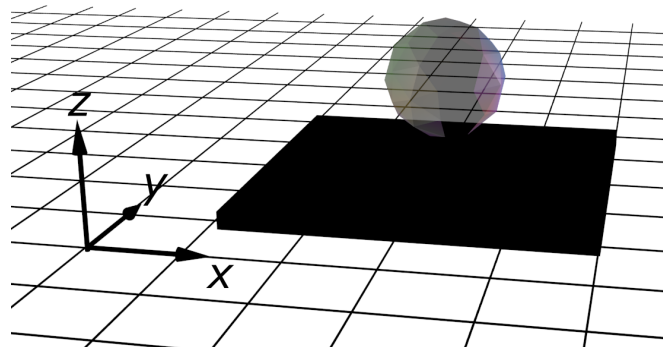
As the initial step, we emphasize that, for a given  $V$  and the unit vector orthogonal to the plane where  $V$  is located at, which is  $\mathbf{r}_{z_V} = [r_{31_V} \ r_{32_V} \ r_{33_V}]^T$ , we choose  $\mathbf{R}_V$  equal to  $\mathbf{K}(r_{31_V}k, r_{32_V}k)$ . So,  $\mathbf{R}_V$  and  $\mathbf{K}(r_{31_V}k, r_{32_V}k)$  end up with the same coordinate frame orientation for  $(k_x, k_y) = (r_{31_V}k, r_{32_V}k)$  and  $\epsilon_V$  becomes zero for this propagation direction. In other words, the locally transverse plane of the plane wave which directly propagates towards to the observation plane of  $V$  is the same as the orientation of that observation plane. Also, in this setup, we assume that the display lies parallel to the ground, which we choose this plane as the  $x$ - $y$  plane, and the  $z$ -axis points upwards. Such a placement of the display and the viewers is shown in Figure 5.4. Also, the display setups in [35, 36] are realized based on the geometry described in this section.



(a) Scene 1



(b) Scene 2



(c) Scene 3

Figure 5.4: A generic table-top wide-viewing-angle holographic display is shown. The planar display which is shown in solid black color lies on the  $x$ - $y$  plane. The 3D image, which is represented as a colored ghost icosahedron, is generated by the display. Each figure shows a different scene of the ghost image captured from a different angle. So, each captured scene is a different paraxial segment of the field diffracted from the display.

In Figure 5.5, a sample rotated coordinate frame as a result of the procedure adopted to generate the rotation matrices for the geometry shown in Figure 5.4 is shown for a given  $\hat{\mathbf{k}}$ . In the figure,  $\boldsymbol{\kappa}_{z_k}(\hat{\mathbf{k}})$  indicates the propagation direction of the corresponding plane wave as well as the unit normal of the observation plane of a given  $V$ , that is shown in transparent gray color. As a result of this procedure of computing the rotation matrices, the basis vectors  $\boldsymbol{\kappa}_{y_k}(\hat{\mathbf{k}})$ ,  $\boldsymbol{\kappa}_{z_k}(\hat{\mathbf{k}})$  and the positive  $z$ -axis always lie at the same 2D plane and  $\boldsymbol{\kappa}_{x_k}(\hat{\mathbf{k}})$  lie at the  $x$ - $y$  plane. However, for a better illustration, in Figure 5.5, the vectors  $\boldsymbol{\kappa}_{x_k}(\hat{\mathbf{k}})$ ,  $\boldsymbol{\kappa}_{y_k}(\hat{\mathbf{k}})$  and  $\boldsymbol{\kappa}_{z_k}(\hat{\mathbf{k}})$  are translated to the center of the observation. As a result of this translation,  $\boldsymbol{\kappa}_{y_k}(\hat{\mathbf{k}})$  vector points towards the  $z$ -axis and  $\boldsymbol{\kappa}_{x_k}(\hat{\mathbf{k}})$  vector lies parallel to the  $x$ - $y$  plane.

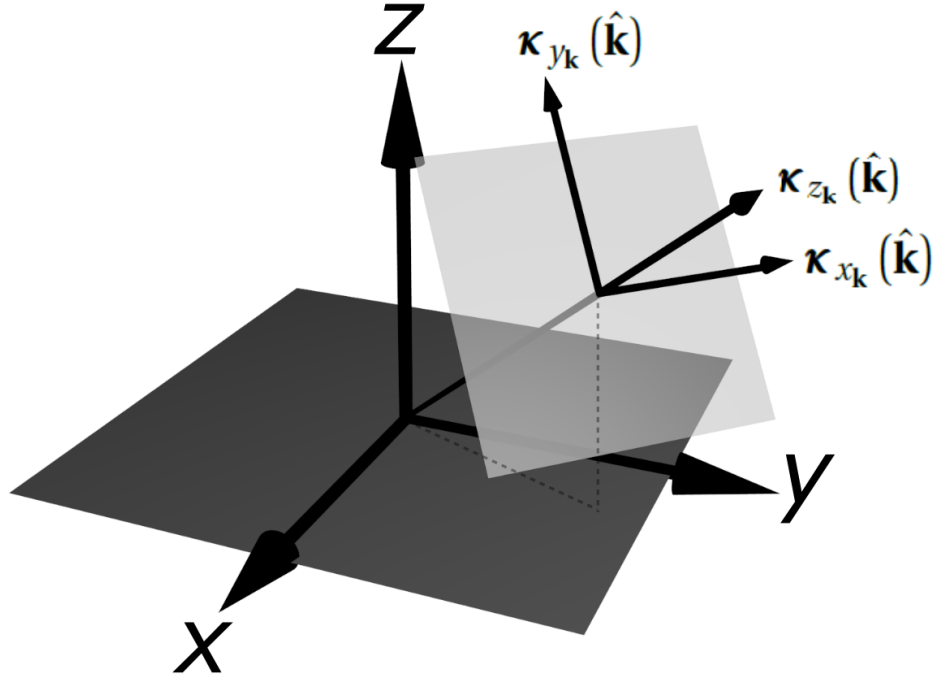


Figure 5.5: A sample rotated coordinate frame on a transverse plane are shown for a given  $\hat{\mathbf{k}}$ , where  $\boldsymbol{\kappa}_{z_k}(\hat{\mathbf{k}})$  is the unit vector along the propagation direction implied by  $\hat{\mathbf{k}}$  and also represents the unit normal of the observation plane of a viewer  $V$ , that is shown in transparent gray color. The axis whose unit vector is denoted as  $\boldsymbol{\kappa}_{y_k}(\hat{\mathbf{k}})$  points towards the positive  $z$ -axis and intersects with it. Also, the axis whose unit vector is denoted as  $\boldsymbol{\kappa}_{x_k}(\hat{\mathbf{k}})$  lies parallel to the  $x$ - $y$  plane.

In order to present the details the computation steps of the rotation matrices, firstly, we define  $\mathbf{n}_z = [0 \ 0 \ 1]^T$  as the unit vector along the  $z$  direction. Then, we compute  $\boldsymbol{\kappa}_{y_{\mathbf{k}}}(\hat{\mathbf{k}})$  from a given  $\boldsymbol{\kappa}_{z_{\mathbf{k}}}(\hat{\mathbf{k}}) = [k_x/k \ k_y/k \ k_z/k]^T$  as

$$\boldsymbol{\kappa}_{y_{\mathbf{k}}}(\hat{\mathbf{k}}) = \frac{\mathbf{n}_z - \langle \mathbf{n}_z, \boldsymbol{\kappa}_{z_{\mathbf{k}}}(\hat{\mathbf{k}}) \rangle \boldsymbol{\kappa}_{z_{\mathbf{k}}}(\hat{\mathbf{k}})}{\left| \mathbf{n}_z - \langle \mathbf{n}_z, \boldsymbol{\kappa}_{z_{\mathbf{k}}}(\hat{\mathbf{k}}) \rangle \boldsymbol{\kappa}_{z_{\mathbf{k}}}(\hat{\mathbf{k}}) \right|} , \quad (5.35)$$

where  $\langle \cdot, \cdot \rangle$  is the vector inner product and  $|\cdot|$  indicates the vector  $l_2$ -norm [110]. In Equation 5.35,  $\boldsymbol{\kappa}_{y_{\mathbf{k}}}(\hat{\mathbf{k}})$  becomes the normalized difference of  $\mathbf{n}_z$  and the projection vector of  $\mathbf{n}_z$  onto  $\boldsymbol{\kappa}_{z_{\mathbf{k}}}(\hat{\mathbf{k}})$ . In other words,  $\boldsymbol{\kappa}_{y_{\mathbf{k}}}(\hat{\mathbf{k}})$  becomes the normalized rejection vector of  $\mathbf{n}_z$  from  $\boldsymbol{\kappa}_{z_{\mathbf{k}}}(\hat{\mathbf{k}})$ . So,  $\boldsymbol{\kappa}_{y_{\mathbf{k}}}(\hat{\mathbf{k}})$ ,  $\boldsymbol{\kappa}_{z_{\mathbf{k}}}(\hat{\mathbf{k}})$  and  $\mathbf{n}_z$  lie at the same 2D plane. Then, we compute  $\boldsymbol{\kappa}_{x_{\mathbf{k}}}(\hat{\mathbf{k}})$  from the resulting  $\boldsymbol{\kappa}_{y_{\mathbf{k}}}(\hat{\mathbf{k}})$  and the corresponding  $\boldsymbol{\kappa}_{z_{\mathbf{k}}}(\hat{\mathbf{k}})$  as

$$\boldsymbol{\kappa}_{x_{\mathbf{k}}}(\hat{\mathbf{k}}) = \boldsymbol{\kappa}_{y_{\mathbf{k}}}(\hat{\mathbf{k}}) \times \boldsymbol{\kappa}_{z_{\mathbf{k}}}(\hat{\mathbf{k}}) , \quad (5.36)$$

where  $\times$  denotes the cross product. Since the resulting vector of a cross product becomes orthogonal to the vectors which are subject to the cross product,  $\boldsymbol{\kappa}_{x_{\mathbf{k}}}(\hat{\mathbf{k}})$  becomes orthogonal to the plane which is formed by the coordinate axes whose unit vectors are  $\boldsymbol{\kappa}_{y_{\mathbf{k}}}(\hat{\mathbf{k}})$  and  $\boldsymbol{\kappa}_{z_{\mathbf{k}}}(\hat{\mathbf{k}})$  [110]. As a result, since  $\boldsymbol{\kappa}_{y_{\mathbf{k}}}(\hat{\mathbf{k}})$ ,  $\boldsymbol{\kappa}_{z_{\mathbf{k}}}(\hat{\mathbf{k}})$  and  $\mathbf{n}_z$  lie at the same 2D plane,  $\boldsymbol{\kappa}_{x_{\mathbf{k}}}(\hat{\mathbf{k}})$  vector becomes also orthogonal to the  $z$ -axis. Hence,  $\boldsymbol{\kappa}_{x_{\mathbf{k}}}(\hat{\mathbf{k}})$  lie at the  $x$ - $y$  plane and so,  $\kappa_{13}(\hat{\mathbf{k}})$  becomes zero for all  $\hat{\mathbf{k}}$ .

Since  $\boldsymbol{\kappa}_{y_{\mathbf{k}}}(\hat{\mathbf{k}})$ 's and the positive  $z$ -axis always lie at the same plane and  $\boldsymbol{\kappa}_{x_{\mathbf{k}}}(\hat{\mathbf{k}})$  always lies at the  $x$ - $y$  plane for all  $\hat{\mathbf{k}}$ 's, an observer which is sensitive to the polarization state of the incoming light can freely move around the  $z$ -axis without changing its own polarization selectivity characteristics, as the rotation of a viewer around the  $z$ -axis does not introduce a change on the local polarization state of the captured optical field. For example, a human observer who wears a polarization filtered goggle can walk around the display without changing the orientation of the goggle or his head. This allows simultaneous generation of two distinct 3D ghost images by a wide-angle holographic 3D display, where each

scalar field is represented through orthogonally polarized fields, as being in the stereoscopic displays [33]. Therefore, hypothetically, two different TV channels can be holographically displayed simultaneously by a single holographic 3DTV and these channels can be watched by wearing a polarization filtering goggle.

On the other hand, the computed  $\mathbf{K}(\hat{\mathbf{k}})$ 's based on this model have a discontinuity at around  $k_z \approx k$  since  $\kappa_{y_{\mathbf{k}}}(\hat{\mathbf{k}})$ 's and the positive  $z$ -axis always lie at the same plane. Hence, if  $\mathcal{L}_V(\hat{\mathbf{k}})$  is not zero at this region,  $\epsilon_V(\hat{\mathbf{k}})$  becomes large. Since being  $\mathcal{L}_V(\hat{\mathbf{k}})$  nonzero at around  $k_z \approx k$  implies that a viewer is located at around  $z$ -axis, in this display setup, we assume that the viewers do not look at the 3D image from very low angles with respect to the  $z$ -axis. Therefore, the  $\theta$  angles associated with the viewers should not be close to 0. However, this method of computing  $\mathbf{K}(\hat{\mathbf{k}})$  matrices provides a circular symmetry on the performance of the display. That is,  $\epsilon_V(\hat{\mathbf{k}})$  remains the same for all  $V$ 's whose associated  $\phi$  angles are the same. Moreover  $\epsilon_V(\hat{\mathbf{k}})$  gets smaller as the  $\theta$  angle associated with the viewer increases.

Please note that, in order to generate a continuous  $\mathbf{K}(\hat{\mathbf{k}})$  distribution, which can be used in an application where the observation plane of the viewers can be arbitrary in space, the tangential vector field generation methods on a sphere can be used [111–114]. However, if these methods are used, the error  $\epsilon_V(\hat{\mathbf{k}})$  may not show a circular symmetry; furthermore, in an application where the polarization state is important, the orientation of the polarization filter should be rearranged at each location of the viewer accordingly since the local polarization state becomes different at each point.

In the following section, we present some computer simulation results which show the validity of the developed electric field model on the representation of a given wide-angle scalar field; we also compare the proposed scalar-to-vector field mapping to the conventional mapping.

## 5.5 Simulation Results

Since we perform computer simulations to test the success of the developed model, we first present the details of the discretization procedure before showing the results.

We assume that a 2D cross-section of a 3D scalar field in the discrete domain is given at  $z = 0$  plane. We denote this field as  $S_d[m, n, 0]$  for  $m \in [-M/2, M/2 - 1]$  and  $n \in [-N/2, N/2 - 1]$ , where  $M$  and  $N$  are even and positive integers and specify the display size. Since we perform the computations in the discrete Fourier domain,  $S_d[m, n, 0]$  represents the samples of one period of the periodic continuous time signal,  $S(x, y, 0)$ , as,

$$S_d[m, n, 0] = S(mX_s, nY_s, 0) \quad , \quad (5.37)$$

where  $X_s$  and  $Y_s$  are the sampling periods along the  $x$  and  $y$  directions, respectively. So,  $S(x, y, 0)$  is periodic by  $MX_s$  and  $NY_s$  along  $x$  and  $y$  directions, respectively. Next, we compute the 2D centered discrete FT (DFT) of  $S_d[m, n, 0]$  as,

$$\mathcal{S}_d[q, p] = \sum_{q=-\frac{M}{2}}^{\frac{M}{2}-1} \sum_{p=-\frac{N}{2}}^{\frac{N}{2}-1} S_d[m, n, 0] e^{j2\pi\left(\frac{qm}{M} + \frac{pn}{N}\right)} \quad , \quad (5.38)$$

for  $q \in [-M/2, M/2 - 1]$  and  $p \in [-N/2, N/2 - 1]$ . Here  $\mathcal{S}_d[q, p]$  represents the samples of one period of  $\mathcal{S}(\hat{\mathbf{k}})$  which is periodic by  $2\pi/X_s$  and  $2\pi/Y_s$  along  $k_x$  and  $k_y$  directions, respectively. So,  $\mathcal{S}_d[q, p]$  can be associated with one period of  $\mathcal{S}(\hat{\mathbf{k}})$  as,

$$\mathcal{S}_d[q, p] = \mathcal{S}\left(\frac{2\pi}{MX_s}q, \frac{2\pi}{NY_s}p\right) \quad . \quad (5.39)$$

We also generate the rotation matrices in the 2D DFT domain as,

$$\mathbf{K}_d[q, p] = \mathbf{K}\left(\frac{2\pi}{MX_s}q, \frac{2\pi}{NY_s}p\right) \quad , \quad (5.40)$$

where the elements of the rotation matrix  $\mathbf{K}(\hat{\mathbf{k}})$  are generated based on the procedure described in Section 5.4 for each  $(q, p)$  pair. Then, from a given local

polarization state,  $C$ , we generate the electric field vector in the 2D DFT domain by using the proposed scalar-to-vector field mapping as,

$$\boldsymbol{\mathcal{E}}_{\text{pro},d}[q,p] = \frac{\mathcal{S}_d[q,p]}{\sqrt{1+|C|^2}} \mathbf{K}_d^T[q,p] \begin{bmatrix} 1 \\ C \\ 0 \end{bmatrix} . \quad (5.41)$$

In order to compare the results of the proposed mapping to that of the conventional mapping, we also generate the  $x$  and  $y$  components of the electric field vector using the conventional technique, that is  $\boldsymbol{\mathcal{E}}_{\text{con},d}[q,p]$ , as,

$$\begin{bmatrix} \mathcal{E}_{\text{con},x,d}[q,p] \\ \mathcal{E}_{\text{con},y,d}[q,p] \end{bmatrix} = \frac{\mathcal{S}_d[q,p]}{\sqrt{1+|C|^2}} \begin{bmatrix} 1 \\ C \\ 0 \end{bmatrix} , \quad (5.42)$$

and generate the corresponding  $z$  component in the 2D DFT domain as,

$$\mathcal{E}_{\text{con},z,d}[q,p] = \mathcal{E}_{\text{con},x,d}[q,p] \mathcal{G}_{x,d}[q,p] + \mathcal{E}_{\text{con},y,d}[q,p] \mathcal{G}_{y,d}[q,p] \quad , \quad (5.43)$$

where

$$\mathcal{G}_{\{x,y\},d}[q,p] = \mathcal{G}_{\{x,y\}} \left( \frac{2\pi}{MX_s} q, \frac{2\pi}{NY_s} p \right) . \quad (5.44)$$

Then, we specify the spatial coordinates of a given oblique plane where a viewer  $V$  is located. In order to do that, at a given tilted and rotated  $z_V = l_V \in \mathbb{R}^+$  plane associated with a viewer  $V$ , we sample the field on a regular rectangular grid on that plane and choose the sampling points as  $m'X'_s$  and  $n'Y'_s$  along  $x_V$  and  $y_V$  directions, respectively, for  $m' \in [-M'/2 + M'_c, M'/2 - 1 + M'_c]$  and  $n' \in [-N'/2 + N'_c, N'/2 - 1 + N'_c]$ , where  $M'_c$  and  $N'_c$  are chosen such that the center point of the generated field on the tilted plane corresponds to  $(M'_c, N'_c)$  in the  $x_V$ - $y_V$  coordinate frame. So,  $m'$  and  $n'$  indicate the sample indices on the oblique plane. Please note that, although the values of  $X'_s$ ,  $Y'_s$ ,  $M'$  and  $N'$  may depend on the physical dimension and geometrical properties of a given  $V$ , since we choose these numbers as the same for all  $V$  in our simulation, we do not insert  $V$  as a subscript in the notation of these parameters. In this respect, since  $X'_s$ ,  $Y'_s$ ,  $M'$  and  $N'$  are variables related to the viewers, they can be chosen independently

from  $X_s, Y_s, M$  and  $N$ , which are variables related to the display. As a result, in  $\mathbf{r}_V$  domain, the sampling points of the 3D scalar field at  $z_V = l_V$  plane become

$$\mathbf{r}_{d,V} = \begin{bmatrix} m'X'_s \\ n'Y'_s \\ l_V \end{bmatrix} \quad (5.45)$$

By using  $\mathbf{r}_{d,V}$ , the sampling points in the global coordinates can be written as

$$\mathbf{r}_d = \begin{bmatrix} x_d \\ y_d \\ z_d \end{bmatrix} = \mathbf{R}_V^T \mathbf{r}_{d,V} = \mathbf{R}_V^T \begin{bmatrix} m'X'_s \\ n'Y'_s \\ l_V \end{bmatrix} . \quad (5.46)$$

Then by using the sampling points  $\mathbf{r}_d$  in the global coordinates, computation formula for the scalar field in the tilted and rotated plane can be written as,

$$\begin{aligned} S_d[\mathbf{r}_d] &= S_d[\mathbf{R}^T \mathbf{r}_{d,V}] \\ &= \frac{1}{MN} \sum_{q=-\frac{M}{2}}^{\frac{M}{2}-1} \sum_{p=-\frac{N}{2}}^{\frac{N}{2}-1} \mathcal{S}_d[q, p] H_{z_d}[q, p] e^{j2\pi\left(\frac{qx_d}{MX_s} + \frac{py_d}{NY_s}\right)} , \end{aligned} \quad (5.47)$$

where  $H_{z_d}[q, p]$  is the transfer function of the free space propagation in the 2D DFT domain for propagating fields and written as,

$$H_{z_d}[q, p] = \begin{cases} e^{j2\pi z_d \sqrt{\frac{1}{\lambda^2} - \frac{q^2}{M^2 X_s^2} - \frac{p^2}{N^2 Y_s^2}}} & \text{if } \frac{q^2}{M^2 X_s^2} + \frac{p^2}{N^2 Y_s^2} < \frac{1}{\lambda^2} \\ 0 & \text{otherwise} \end{cases} . \quad (5.48)$$

Please note that, we compute the summations in Equation 5.47 for each  $(x_d, y_d, z_d)$ , separately, and do not use a fast algorithm, like the fast Fourier transform.

Similarly, by using Equation 5.47, we compute the samples of the vector field at  $z_V = l_V$  plane from  $\mathcal{E}_{\text{pro},d}[q, p]$  as,

$$\begin{aligned} \tilde{\mathbf{E}}_{\text{pro},d}[\mathbf{r}_d] &= \mathbf{R}_V \mathbf{E}_{\text{pro},d}[\mathbf{r}_d] = \mathbf{R}_V \mathbf{E}_{\text{pro}}[\mathbf{R}_V^T \mathbf{r}_{d,V}] \\ &= \frac{1}{MN} \sum_{q=-\frac{M}{2}}^{\frac{M}{2}-1} \sum_{p=-\frac{N}{2}}^{\frac{N}{2}-1} \mathbf{R} \mathcal{E}_{\text{pro},d}[q, p] H_{z_d}[q, p] e^{j2\pi\left(\frac{qx_d}{MX_s} + \frac{py_d}{NY_s}\right)} . \end{aligned} \quad (5.49)$$

We also use the same formula to compute  $\tilde{\mathbf{E}}_{\text{con},d}[\mathbf{r}_d]$  from  $\mathbf{E}_{\text{con},d}[q, p]$ .

Please note that, for a given  $z_d$ ,  $S(x_d, y_d, z_d)$  becomes a periodic function along  $x$  and  $y$  directions by  $MX_s$  and  $NY_s$ , respectively. Hence, the scalar field shows a periodicity relation between tilted planes in 3D space, where more detailed discussion about this relation can be found in [91]. The same periodicity relation can also be obtained for the components of the vector fields, since they behave as separate scalar fields. On the other hand, both the scalar and the vector fields may not exhibit such a periodic pattern along  $x_V$  and  $y_V$  directions at a tilted and rotated  $z_V$  plane. That is, over a single  $z_V$  plane, a periodic pattern may not be observed. Moreover, the field values at a  $z_V$  plane can be nonzero all over the plane. As a result, since we are able to store only a finite portion of the field, we assume that,  $S_d[\mathbf{R}_V^T \mathbf{r}_{d,V}]$ ,  $\tilde{\mathbf{E}}_{\text{pro},d}[\mathbf{R}_V^T \mathbf{r}_{d,V}]$  and  $\tilde{\mathbf{E}}_{\text{con},d}[\mathbf{R}_V^T \mathbf{r}_{d,V}]$  are always zero when  $m' \notin [-M'/2 + M'_c, M'/2 - 1 + M'_c]$  and  $n' \notin [-N'/2 + N'_c, N'/2 - 1 + N'_c]$ . This assumption also overlaps with realistic applications as all the field recording devices can capture only a finite portion of the field on their observation plane.

As the lowpass filter, we use a Gaussian filter whose 2D frequency response is defined as,

$$\mathcal{L}(\hat{\mathbf{k}}_V) = e^{-\frac{\mathbf{k}_V^2}{2k_c^2}} \quad . \quad (5.50)$$

The 2D IFT of this filter, apart from a constant multiplier, is [4]

$$L(\hat{\mathbf{r}}_V) = e^{-\frac{k_c^2 \hat{\mathbf{r}}_V^2}{2}} \quad . \quad (5.51)$$

Please note that, in order to prevent the ringing effect in the resulting images after the lowpass filtering, here we choose a Gaussian lowpass filter, instead of a sharp-edge filter [67]. Then, we discretize  $L(\hat{\mathbf{r}}_V)$  as  $L_d[m', n'] = L(m'X'_s, n'Y'_s)$  and find the lowpass filtered scalar and vector field components at the tilted and rotated plane as,

$$\begin{aligned} S_{V,d}[\mathbf{R}_V^T \mathbf{r}_{d,V}] &= S_d[\mathbf{R}_V^T \mathbf{r}_{d,V}] ** L_d[m', n'] \quad , \\ \mathbf{E}_{\text{pro},V,d}[\mathbf{R}_V^T \mathbf{r}_{d,V}] &= \tilde{\mathbf{E}}_{\text{pro},d}[\mathbf{R}_V^T \mathbf{r}_{d,V}] ** L_d[m', n'] \quad , \\ \mathbf{E}_{\text{con},V,d}[\mathbf{R}_V^T \mathbf{r}_{d,V}] &= \tilde{\mathbf{E}}_{\text{con},d}[\mathbf{R}_V^T \mathbf{r}_{d,V}] ** L_d[m', n'] \quad , \end{aligned} \quad (5.52)$$

where “\*\*” denotes 2D linear convolution in discrete domain. Since  $S_d[\mathbf{r}_d]$  and the components of  $\mathbf{E}_{\text{pro},V,d}[\mathbf{r}_d]$  and  $\mathbf{E}_{\text{con},V,d}[\mathbf{r}_d]$  are assumed to be confined in a finite interval, the convolution outputs are also confined in a finite interval. We also choose the window size of  $L_d[m', n']$  large enough such that the tails of the lowpass filter which fall outside of the window are negligible.

Finally, for comparison, we compute three intensity patterns for the given  $l_V$  as

$$\begin{aligned} I_s[m', n'] &= |S_{V,d}[\mathbf{R}_V^T \mathbf{r}_{d,V}]|^2 \quad , \\ I_{E,\text{pro}}[m', n'] &= |\mathbf{E}_{\text{pro},V,d}[\mathbf{R}_V^T \mathbf{r}_{d,V}]|^2 \quad , \\ I_{E,\text{con}}[m', n'] &= |\mathbf{E}_{\text{con},V,d}[\mathbf{R}_V^T \mathbf{r}_{d,V}]|^2 \quad . \end{aligned} \quad (5.53)$$

In the simulations, we choose  $\lambda = 500 \text{ nm}$ . Since we assume that the scalar field may include all the propagating plane waves propagating along any direction, we choose  $X_s = Y_s = X'_s = Y'_s = \lambda/2$  to prevent aliasing if a lowpass filter is used during conversion to an analog signal [67] and assume that the pixels of the display are infinitely small to achieve that there is no bandwidth limitation for the propagated waves. We also choose  $N = M = 2048$ . Please note that, as a result of the chosen parameters, the actual dimension of the display becomes  $0.512 \text{ mm} \times 0.512 \text{ mm}$ , which is too small for a realistic 3DTV application. However, as it will be shown below, these parameters are sufficient to test the success of the developed scalar-to-vector field mapping technique. So we do not choose a larger dimension for the display in order not to increase the computational complexity.

As the simulation pattern, we take a 3D computer generated rigid object, as shown in Figure 5.6. We sample the surface of the object and assume that each sample behaves as a point source for the scalar field. So, we reach a point cloud representation for the surface of this object, where each point has a 3D location and an amplitude information and these amplitude values determine the 3D scalar field associated with the object. Then, we compute the samples of the 2D cross-section of the 3D scalar field at the display surface as

$$S_d[m, n, 0] = \sum_{i=1}^{N_p} A_i \frac{e^{-jkR_{m,n,i}}}{R_{m,n,i}} \quad , \quad (5.54)$$

where

$$R_{m,n,i} = \sqrt{(x_i - mX_s)^2 + (y_i - nY_s)^2 + z_i^2} \quad . \quad (5.55)$$

Here  $N_p$  is the total number of points in the point cloud representation and in our case  $N_p \approx 5 \times 10^5$ .  $A_i$  and  $(x_i, y_i, z_i)$  represent the real-valued amplitude and the 3D location of the  $i^{\text{th}}$  point, respectively. The dimension and the location of the object as well as the dimension of the display are chosen such that a satisfactory reconstruction by the SLM is achieved [31]. That is, the ghost image is reconstructed at a distance to the display close enough such that the reconstruction in large angles can be performed by the display whose size is  $2048 \times 2048$ .

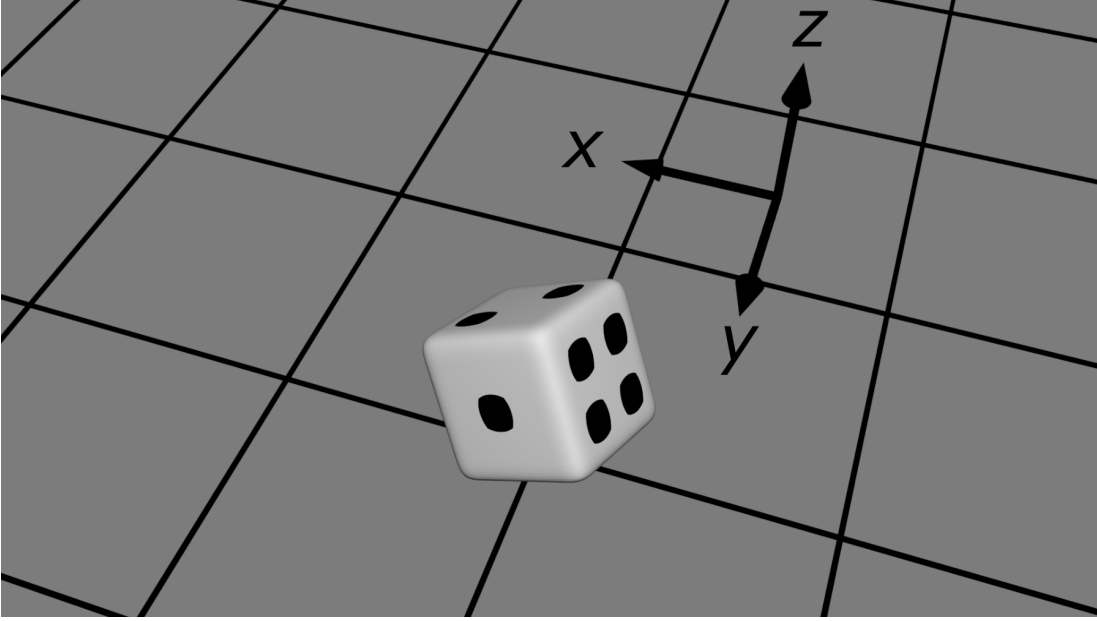


Figure 5.6: The 3D rigid object whose hologram is generated for the computer simulation and the chosen coordinate frame are shown.

Please note that, although we perform the simulations on a computer generated object, the hologram of a real object can be generated by using the methods described in [37] and the references therein. Also, since the scalar field is given over a curved surface, the hologram written on the SLM using Equation 5.54 does not achieve a perfect reconstruction of the given scalar field since the points on the object are assumed to be sources and since their reconstruction using a field propagated from the display results in mutual couplings [115]. However, due to its simplicity, we use this technique to generate the field on the SLM plane, where

it is already utilized in the literature [38, 39, 116, 117]. If perfect reconstruction of the given scalar field is desired, the methods given in [98–101] can be used.

In the simulation we take the constant local polarization state as the diagonal linear polarization, i.e.  $C = 1$ . By using the generated  $S_d[m, n, 0]$  and Equations 5.38, 5.42 and 5.41, we compute the 2D centered DFTs of the given scalar field and the  $x$  and  $y$  components of the electric field at  $z = 0$  plane for the conventional and proposed models, respectively. In Figure 5.7, the magnitudes of the electric field patterns written on the SLM surface, that are  $E_{\text{con},x,d}[m, n, 0]$ ,  $E_{\text{con},y,d}[m, n, 0]$ ,  $E_{\text{pro},x,d}[m, n, 0]$  and  $E_{\text{pro},y,d}[m, n, 0]$ , are shown. Please note that, since we choose  $C = 1$ ,  $E_{\text{con},x,d}[m, n, 0]$  and  $E_{\text{con},y,d}[m, n, 0]$  become equal to each other and they also equal to  $S_d[m, n, 0]$  apart from a constant multiplier. However,  $E_{\text{pro},x,d}[m, n, 0]$  and  $E_{\text{pro},y,d}[m, n, 0]$  become different as they are generated so as to satisfy the imposed polarization constraint at each tilted plane. Please note that  $\mathcal{G}_x(\hat{\mathbf{k}})$  amplifies the horizontally oriented features of the  $x$  component of the electric field, as shown by Figure 2.4a. So, if the  $x$  component has such features, they are excessively amplified and the  $z$  component becomes dominant over the other components. As it can be seen from Figures 5.7a and 5.7b, the magnitude of the horizontally oriented features in the scalar field decreases in the  $x$  component of the resulting electric field due to the filters used in the proposed mapping. Therefore, the frequency components which are excessively amplified by  $\mathcal{G}_x(\hat{\mathbf{k}})$  disappear in the  $x$  component of the proposed model. Similarly, in the resultant  $y$  component due to the proposed mapping, the vertically oriented features, which are excessively amplified by  $\mathcal{G}_y(\hat{\mathbf{k}})$ , are filtered out.

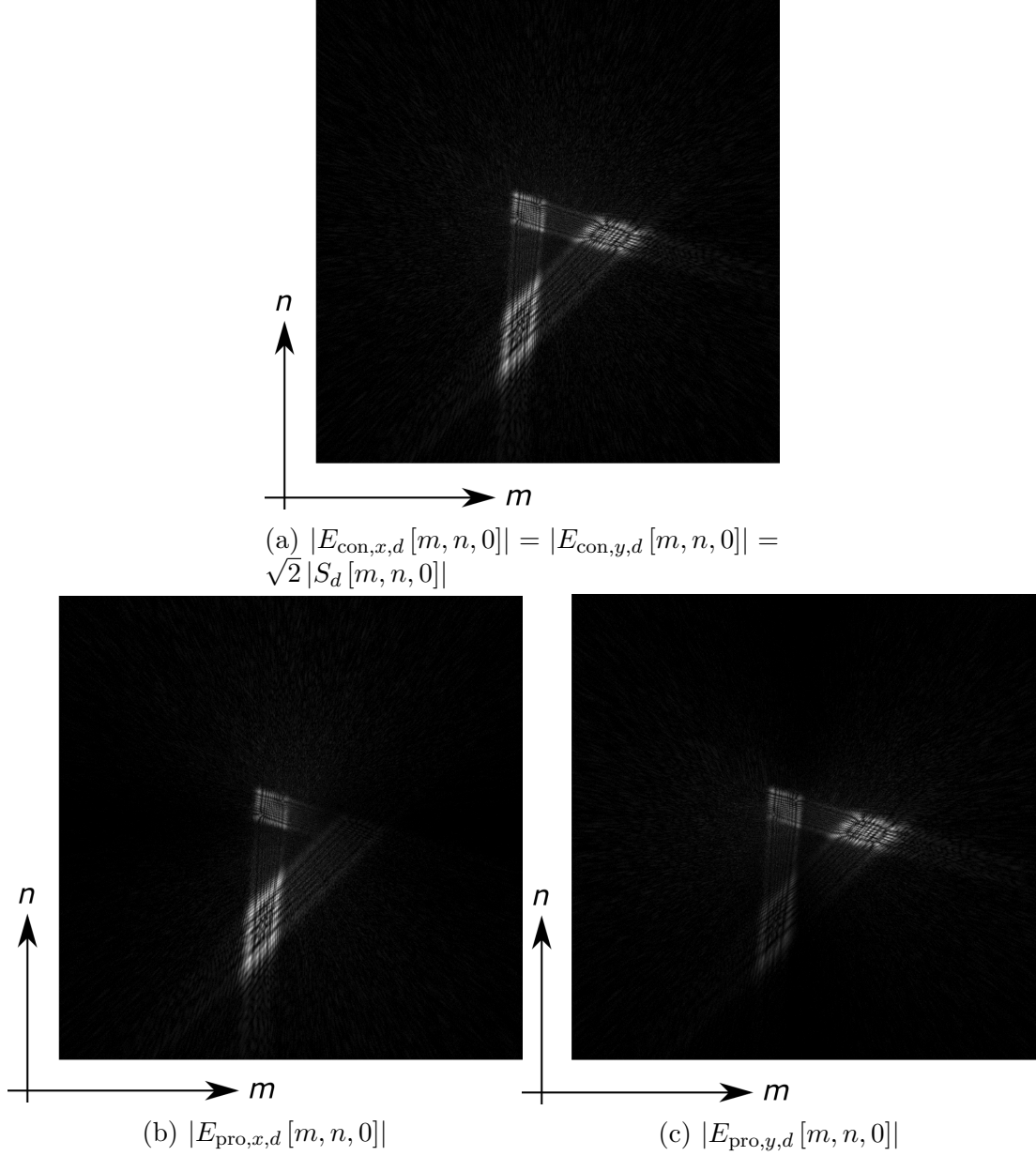


Figure 5.7: The magnitudes of the field components on the SLM surface are shown. Figure 5.7a shows the patterns for the conventional method, where the scalar field and the  $x$  and  $y$  components of the electric field are, apart from a constant multiplier, equal. Figures 5.7b and 5.7c show the  $x$  and  $y$  components for the proposed model, respectively. The centers of the images correspond to  $(m, n) = (0, 0)$ .

Then, by using  $S_d[m, n, 0]$ , we compute three different 2D scalar fields at the planes associated with the angles  $(\theta, \phi) = (37^\circ, 316^\circ)$ ,  $(\theta, \phi) = (60^\circ, 176^\circ)$  and  $(\theta, \phi) = (70^\circ, 74)$ , which correspond to the planes on the die where the numbers 2, 4 and 1 are located, respectively. The  $z_V$  planes at which the scalar fields are computed at these angles are chosen such that the object location coincides with the chosen  $z_V$  plane. Therefore, a viewer is assumed to be directly focused to the plane where the object is located. For this object and the chosen planes for the simulations, we choose  $(M', N') = (512, 512)$  for all  $(\theta, \phi)$  pairs. These values are sufficient to display the 3D image of the object at the corresponding tilted planes and the reconstructed field components become negligible outside of the interval implied by the chosen  $(M', N')$  pair. Finally, after applying the lowpass filter, which is given by Equation 5.51, with  $k_c = k/3$ , we compute the scalar field intensity patterns,  $I_s$ 's, for each angle. These scalar field intensity patterns can be considered as the intensity patterns which are desired to be generated by the electric field propagated from the SLM. In other words, the computed  $I_s$  is the intensity pattern that is desired to be generated by the display.

Next, we compute the electric field components at the specified tilted planes and compare the intensity patterns generated by two methods to the scalar field intensity pattern at these planes. In Figure 5.8, the results for the  $(\theta, \phi) = (37^\circ, 316)$  case, which corresponds to die face 2, are shown. Figures 5.8a, 5.8b and 5.8c show the resulting intensity patterns, for the desired scalar field  $I_s$ , for the conventionally obtained vector field  $I_{E,con}$  and for the proposed scalar-to-vector converted case  $I_{E,pro}$ , respectively. From these results, it can be said that, since the angle  $\theta$  is small, there is no difference between the proposed and conventional mappings in terms of generating the given scalar field intensity pattern. Therefore, it can be said that the conventional method also performs well at this oblique angle in terms of generating the desired scalar results.

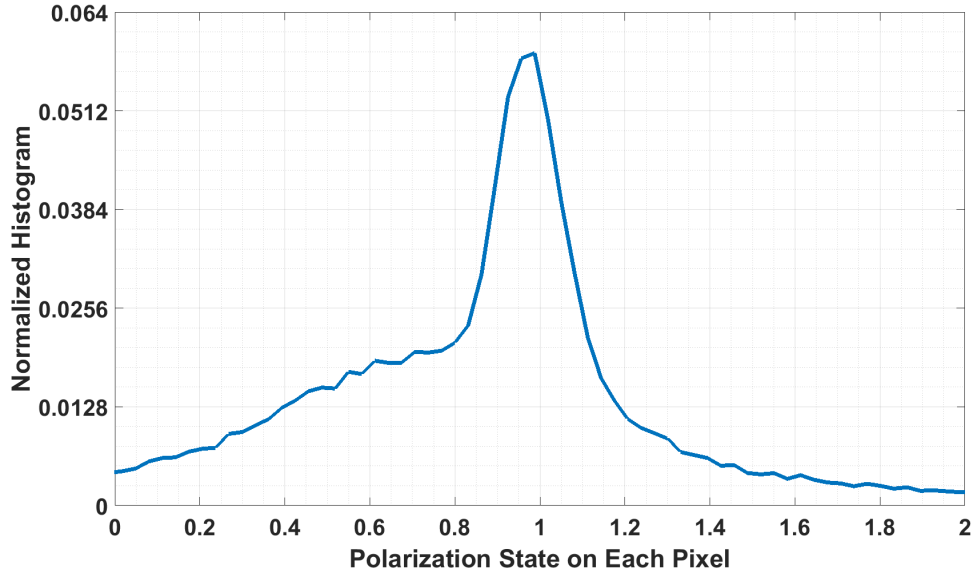
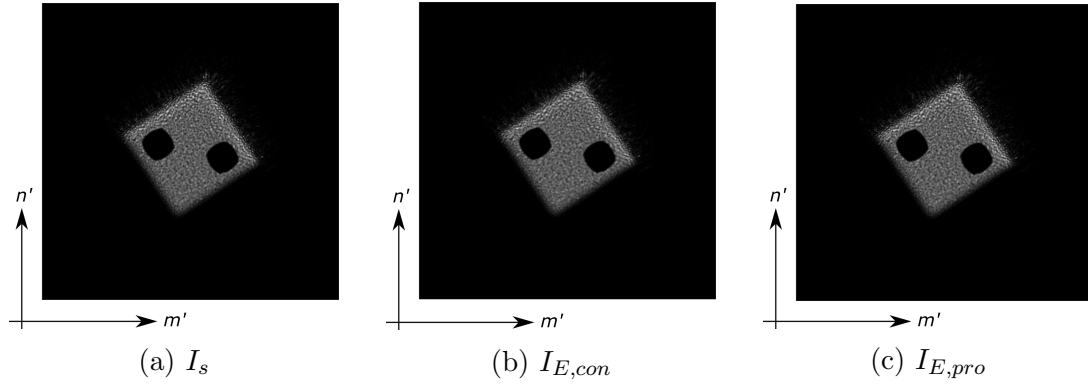
In order to show that the chosen polarization state, which is  $C = 1$ , is obtained on the reconstruction plane, we compute the histogram of the pointwise polarizations on that plane for the proposed model. That is, we define the pointwise polarization for a given pixel,  $(m', n')$ , as  $E_{pro,d,y,V} [\mathbf{R}^T \mathbf{r}_{d,V}] / E_{pro,d,x,V} [\mathbf{R}^T \mathbf{r}_{d,V}]$ . After computing the pointwise polarization for each  $m'$  and  $n'$ , we compute

the histogram of the resulting polarization states. We also normalize the histogram with the total pixel count. The real part of the normalized histogram for  $(\theta, \phi) = (37^\circ, 316^\circ)$  case is shown in Figure 5.8d. Since the imaginary parts of the pointwise polarization states are almost zero for all  $(m', n')$ 's, the histogram of the imaginary parts is not shown. From the figure, it can be seen that, the desired polarization state, which is  $C = 1$ , is almost achieved. Please note that, since the desired polarization state is completely lost in the conventional mapping, we do not show the resulting polarization histogram for that case. Therefore, even if the scalar intensity pattern can be obtained at this angle by the conventional technique, it fails to generate a specified polarization state. On the other hand the proposed technique ends up with both satisfactory intensity results and the specified polarization state.

In Figure 5.9, same results are shown for  $(\theta, \phi) = (60^\circ, 176^\circ)$  case, which corresponds to die face 4. In these figures, it can be seen that the intensity pattern due to the conventional mapping becomes brighter than the desired scalar field intensity pattern. So, it can be said that, as  $\theta$  increases, the deviation of the intensity pattern due to the conventional mapping from the desired scalar field intensity pattern increases, due to the neglected  $z$  component of the electric field. On the other hand, if the proposed mapping is used, the desired scalar field intensity pattern is satisfactorily generated. The success of the proposed mapping can be seen from these figures, as well. Moreover, it can be seen from the corresponding histogram plots that, the desired polarization state is also obtained for this case.

The results for  $(\theta, \phi) = (70^\circ, 74^\circ)$  case, which corresponds to die face 1, are shown in Figure 5.10. In this case, the deviation of the intensity pattern due to the conventional method from the desired scalar intensity pattern becomes more severe than the  $(\theta, \phi) = (37^\circ, 316^\circ)$  and  $(\theta, \phi) = (60^\circ, 176^\circ)$  cases, where in this case the magnitude of the  $z$  component of the electric field is dominant over the  $x$  and  $y$  components in the conventional technique. Therefore,  $I_{E,con}$  becomes much brighter than  $I_s$  and  $I_{E,pro}$ , such that  $I_s$  and  $I_{E,pro}$  cannot be noticed from Figures 5.10a and 5.10c, where  $I_s$  and  $I_{E,pro}$  are mapped to the grayscale levels jointly with  $I_{E,con}$ . In order to show that the proposed mapping ends up with the

correct intensity pattern, we exclude  $I_{E,con}$  and map  $I_s$  and  $I_{E,pro}$  to the grayscale levels jointly. We show these patterns in Figures 5.10d and 5.10e, where it can be seen that the desired scalar field intensity pattern is generated as result of the proposed mapping. Moreover, at the bottom region of the reconstructed die face 1, there are some features which are located at a plane with a deviation angle from the  $z$ -axis being larger than  $70^\circ$ . Since the change on  $\mathcal{G}_{\{x,y\}}(\hat{\mathbf{k}})$  is abrupt at these angles, which can be seen from Figure 2.3, besides the excessive intensity amplification, some undesired local features arise in  $I_{E,con}$  at these angles, that can be seen as a tilted bright line at the bottom of the die face in Figure 5.10b. The proposed mapping, on the other hand, compensates such undesired artifacts, too. Also, the desired polarization state is almost achieved in this case, as well.



(d) Histogram of the Polarization State

Figure 5.8: Simulation results for  $(\theta, \phi) = (37^\circ, 316^\circ)$  case is shown. Figures 5.8a, 5.8b and 5.8c are the desired scalar field intensity, the obtained intensity pattern due to the conventional mapping and the obtained intensity pattern due to the proposed mapping, respectively, where  $I_s$ ,  $I_{E,con}$  and  $I_{E,pro}$  are jointly mapped to the grayscale levels. Figure 5.8d shows the normalized histogram of the pointwise polarization state of the resulting electric field due to the proposed mapping.

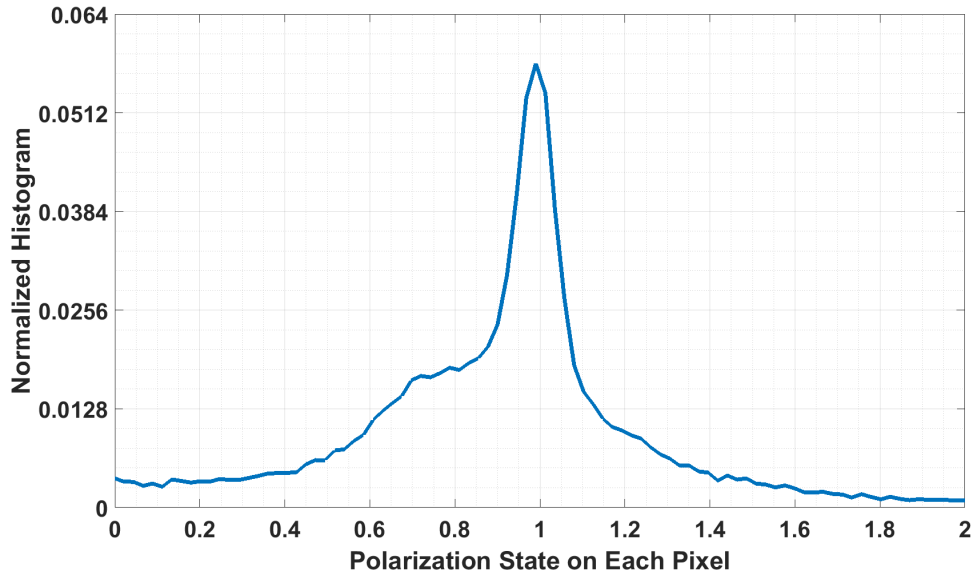
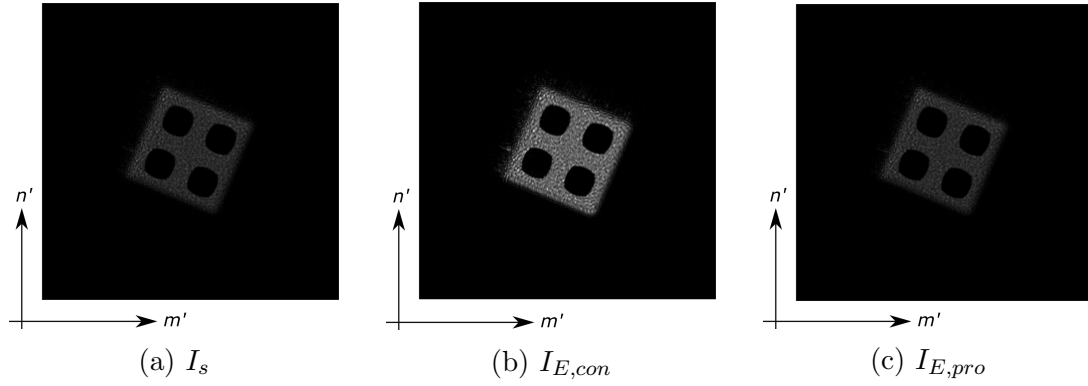
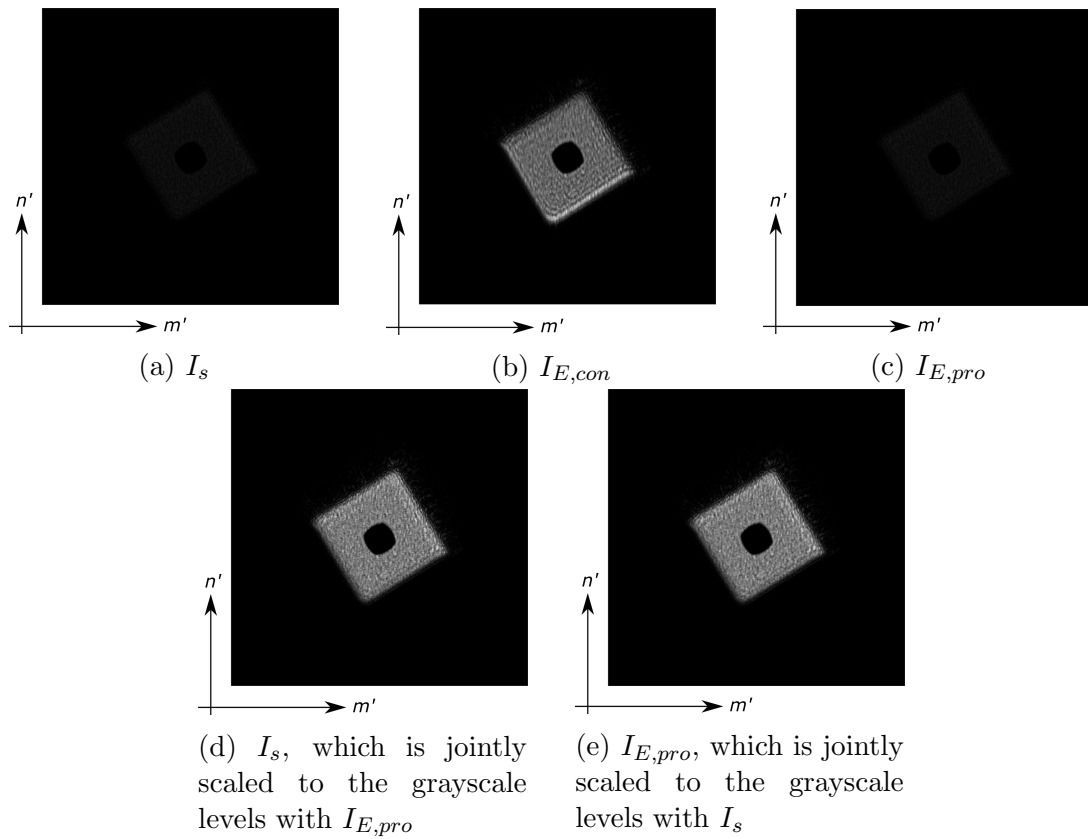
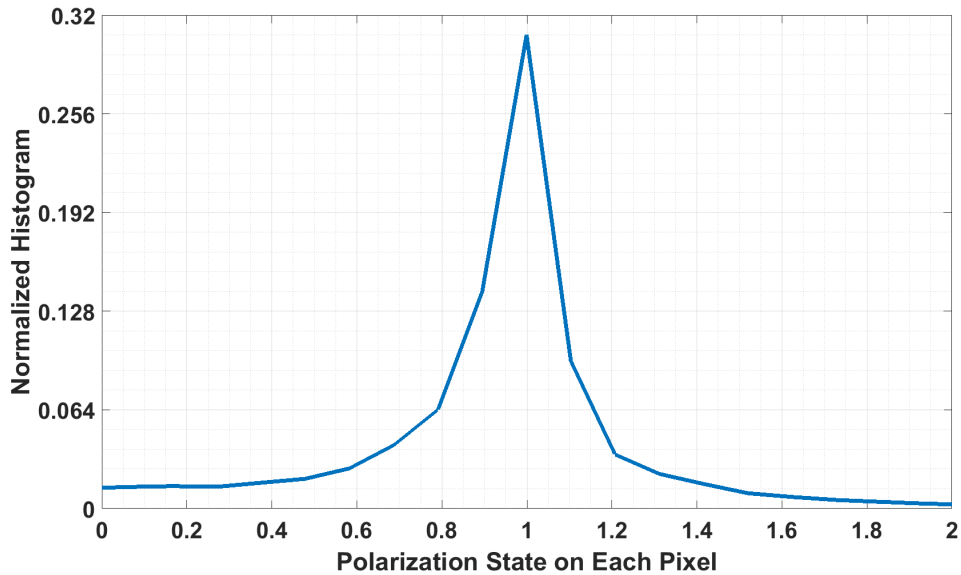


Figure 5.9: Simulation results for  $(\theta, \phi) = (60^\circ, 176^\circ)$  case is shown. Figures 5.9a, 5.9b and 5.9c are the desired scalar field intensity, the obtained intensity pattern due to the conventional mapping and the obtained intensity pattern due to the proposed mapping, respectively, where  $I_s$ ,  $I_{E,con}$  and  $I_{E,pro}$  are jointly mapped to the grayscale levels. Figure 5.9d shows the normalized histogram of the pointwise polarization state of the resulting electric field due to the proposed mapping.



(Continues to the next page)



(f) Histogram of the Polarization State

Figure 5.10: (Continues from the previous page) Simulation results for  $(\theta, \phi) = (70^\circ, 74^\circ)$  case is shown. Figures 5.10a, 5.10b and 5.10c are the desired scalar field intensity, the obtained intensity pattern due to the conventional mapping and the obtained intensity pattern due to the proposed mapping, respectively, where  $I_s$ ,  $I_{E,con}$  and  $I_{E,pro}$  are jointly mapped to the grayscale levels. Since  $I_s$  and  $I_{E,pro}$  cannot be seen clearly in Figures 5.10a, and 5.10c, we map  $I_s$  and  $I_{E,pro}$  jointly to the grayscale levels and show in Figures 5.10d and 5.10e, respectively. Figure 5.10f shows the normalized histogram of the pointwise polarization state of the resulting electric field due to the proposed mapping.

# Chapter 6

## Conclusions

In this dissertation, different scalar-to-polarized field transformation techniques for wide-viewing-angle holographic displays are proposed and their limitations are discussed. The contributions can be briefly summarized as follows. First, it is analytically and numerically shown by using the linear-shift invariant (LSI) system concept that the conventional scalar-to-polarized optical field mapping causes large error in wide-angle fields. Then we proved that if the transverse field components of electric field have an imposed one-to-one LSI relation between them at a 2D plane, then a one-to-one relation between a given scalar field and a polarized optical field can be established. In this case, a simple one-to-one relation between the given scalar field and the scalar components of the electromagnetic field turns out to be another imposed 2D LSI system. Although some other one-to-one relations can be established between scalar and polarized optical fields, imposing LSI relations as described in this dissertation paves the way for low computational complexity and high flexibility in obtaining the desired scalar results through polarized wave fields, as all the computations can be performed through multiplications in the 2D Fourier domain. Then, we proposed different LSI scalar-to-vector field transformation methods in order to achieve desired scalar results in different holographic display applications. The first one, which is the power spectrum equalized model, achieves that the scalar field and the resulting electromagnetic field have the same power spectra, that is, the magnitude

squares of the Fourier transforms of the given scalar field and the electromagnetic field become equal. The second proposed method achieves that the local paraxial segments of the polarized field at tilted and rotated planes have a simple polarization state. So, paraxial segments of a given scalar field at such planes can be characterized through this simply polarized optical field.

In order to analyze the limitations of the conventional scalar approximation quantitatively, we first developed a tool which includes a 2D LSI transform whose inputs are the transverse components of the electric field and the output is the longitudinal component. Since the longitudinal component is the source of error in the conventional scalar-to-vector field mapping, the magnitude response of the filters which are used in the computation of the longitudinal component becomes the indicator of the error. By investigating the transfer functions of the filters, we observed that the amount of error increases rapidly near the limiting spatial frequency  $k$  for the propagating fields. So, if the conventional scalar-to-vector field is performed for a given scalar field which has those large spatial frequency components, then, a large error arises in obtaining the desired scalar results by the polarized field generated by the display. Moreover, we developed an appropriate digital simulator that successfully computes the longitudinal component from the transverse field components of the electric field for the propagating case. The simulator output gives the exact samples of the continuous longitudinal field if the filter size is chosen such that each frequency content of the continuous input fields is represented in the 2D DFT computations. Furthermore, if this condition is satisfied, the exact continuous longitudinal field can also be found from the discrete simulation output using the well-known Shannon's digital-to-analog reconstruction algorithm. By using a 2D discrete chirp signal as the test input to the simulator, the strength of the resulting longitudinal component is investigated for different frequency regions. The results overlap with the expectations that the longitudinal component is too large in the large frequency regions. So, it can be said that the conventional scalar theory fails at these regions.

Since pixellated displays are widely used in holographic 3DTV applications, we analyzed the effect of pixel and display parameters on the validity of the conventional scalar mapping, as well. For this purpose, we first derived the formula

for the computation of the longitudinal component of a monochromatic electric field produced by a flat and pixelated display. Then, the validity of the conventional scalar approximation in the displays are quantitatively evaluated. We find that, for a single pixel, the error due to the conventional method increases up to 45% when the width of a pixel is about  $1.5\lambda$ . Moreover, when the output field is generated through multiple pixels, and if the propagation direction of plane wave components of an electric field are confined in a narrow band in  $k_x$ - $k_y$  plane, then, the error in the scalar approximation can be reduced if the output linear polarization direction becomes vertical to the propagation direction of the plane waves.

Also, if the optical field has a wide extent in space and it contains the same frequency components at different locations of a plane, then the location of an observer or an optical sensor on that plane becomes important. In this respect, a 2D short-space Fourier transform (STFT) based analysis method for the local error due the use of the conventional scalar approximation is developed. A numerical simulation using a chirp signal showed that, although the error is negligible in low-frequency regions, it becomes close to 100% in the highest frequency region.

In order to develop some other scalar-to-polarized field transformation techniques which do not produce the errors which arise due to the conventional technique, we first developed a general constraint on the electromagnetic fields such that the electromagnetic fields having this constraint can be fully and simply represented by a single scalar field. In this way, a one-to-one mapping between the set of scalar fields and the set of electromagnetic fields which have this constraint can be established. In order to do this, we first showed that, as the longitudinal component of the electric field, the scalar components of the magnetic field vector can be computed from the transverse field components of the electric field using different 2D LSI systems, where both the transfer functions and the impulse responses of the filters which are used in the systems are specified. These relations are the results of Maxwell's equations and remain valid at all 2D cross-sections of the 3D space. Then, we put the constraint as, if the transverse field components of the electric field are related each other through an imposed one-to-one LSI system, then knowing just one of the two transverse field components becomes

sufficient to characterize the entire electromagnetic field. In addition to this, if a given scalar field is related to the scalar components of the vector field through another imposed one-to-one LSI systems, then that given scalar field characterizes the electromagnetic field. Therefore, the scalar components of the electromagnetic field can be computed from this scalar field by using the same filters at all 2D cross-sections of 3D space. In this respect, this general constraint extends the usability of the scalar wave theory of optics by using different LSI systems whose input is the given scalar field and the output is the independent component of the vector field. The conventional scalar theory remains as a special case of this general condition, as well. As it is stated before, although some other set of constraints for a one-to-one mapping between scalar and polarized fields can be established, the constraint proposed in this dissertation provides a computationally simple relation between the scalar and electromagnetic fields.

By using the general constraint, we developed our first scalar-to-vector field transformation technique. Under the proposed mapping, the power spectra of the scalar field and the corresponding electromagnetic field become equal if the transverse components of the electric field are generated from the scalar field as

$$\begin{aligned}\mathcal{E}_x(\hat{\mathbf{k}}) &= \mathcal{S}(\hat{\mathbf{k}}) \mathcal{T}_x(\hat{\mathbf{k}}) \\ \mathcal{E}_y(\hat{\mathbf{k}}) &= \mathcal{S}(\hat{\mathbf{k}}) \mathcal{T}_y(\hat{\mathbf{k}}) \quad ,\end{aligned}\tag{6.1}$$

where the linear-shift invariant filters  $\mathcal{T}_{\{x,y\}}(\hat{\mathbf{k}})$  satisfy

$$1 = \left| \mathcal{T}_x(\hat{\mathbf{k}}) \right|^2 + \left| \mathcal{T}_y(\hat{\mathbf{k}}) \right|^2 + \left| \mathcal{T}_x(\hat{\mathbf{k}}) \mathcal{G}_x(\hat{\mathbf{k}}) + \mathcal{T}_y(\hat{\mathbf{k}}) \mathcal{G}_y(\hat{\mathbf{k}}) \right|^2 \quad .\tag{6.2}$$

As a result of the power spectrum equalization, total powers of the scalar field and the corresponding electric field become always equal at any arbitrary  $z$  plane. The filters are also specified for electric fields with either zero longitudinal component or simple polarization features. The resulting filters for simple polarization cases compensate the excessive amplification of  $\mathcal{G}_{\{x,y\}}(\hat{\mathbf{k}})$  when  $|\hat{\mathbf{k}}| \approx k$ . The performance of the power spectrum equalized model is tested by some computer simulations and compared to the performance of the conventional scalar-to-vector wave field mapping. In the simulations, the scalar field intensity and the corresponding electric field intensities in space domain are produced. It is observed

that, the intensity pattern of the scalar field is nearly the same as the intensity pattern of the corresponding electric field due to the proposed mapping in different frequency regions. However, if the conventional scalar-to-vector wave field mapping is used, the difference between the corresponding intensity patterns can be quite large. In this respect, the power equalizing scalar-to-vector wave field mapping should be preferred over the conventional mapping; this is particularly important in some applications, such as in wide-angle imaging, optical communications or Fourier transforming systems. The use of the proposed model is also tested in a phase retrieval of a discrete Gaussian signal with a random phase. In this simulation, we again observed that the proposed mapping outperforms the conventional mapping in terms of the pointwise matching of the scalar intensity to the electric field intensity and the filters suppresses the undesired noise components which arise in the conventional mapping.

All the filters,  $\mathcal{T}_{\{x,y\}}(\hat{\mathbf{k}})$ , that satisfy Equation 6.2 can be used in imaging systems where the Fourier transform of the field is captured. In other words, if the Fourier transform of the optical field is captured by an imaging system, then, the filters,  $\mathcal{T}_{\{x,y\}}(\hat{\mathbf{k}})$  satisfying Equation 6.2 provides that the desired scalar results are obtained without error. However, if the imaging system does not capture the Fourier transform of the optical field, an arbitrary  $\mathcal{T}_{\{x,y\}}(\hat{\mathbf{k}})$  pair satisfying Equation 6.2 may not end up with the desired scalar intensity. For such systems, we develop our second scalar-to-polarized optical field transformation technique. This mapping is performed such that each propagating plane wave component has a simple polarization feature at its locally transverse plane and these simply polarized components are directly matched with the plane wave components of a given scalar field. Under the constraint that an observer captures a paraxial segment of the generated optical field, the developed algorithm is useful in wide-viewing-angle holographic 3DTV applications. In order to obtain satisfactory results, the coordinate frames of the locally transverse planes of the propagating plane waves should be chosen such that the orientation of the frames vary slowly. As opposed to the conventional scalar-to-vector field mapping, which requires that the plane where an observer is located should be almost parallel to the display plane, in this mapping, the observer can be located at an arbitrary

tilted and rotated plane. However, as in the paraxial conventional scalar imaging formulations, a viewer located at a tilted and rotated plane should capture a paraxial segment of the field on that oblique plane. Using a computer code which simulates a 3DTV setup where the display is located at a  $z$  plane and the observers are assumed to be located at a tilted and rotated plane with respect to a  $z$  plane, we tested the success of the developed mapping and compare it to the conventional mapping. It is observed that, in large angles, the optical intensity due to the conventional mapping arises as an excessively amplified version of a desired scalar field intensity pattern, where the amplification is caused by the longitudinal component which is neglected during the mapping. On the other hand, the proposed mapping ends up with almost exactly the same scalar field intensity pattern at all the angles under test. Moreover, it is also shown that the given polarization states are preserved at each tilted and rotated plane. So, in an application where the polarization information is important, the proposed algorithm can be used. In conclusion, the proposed model enables the scalar wave theory to be used in wide-viewing angle holographic display applications under the given constraints.

Thanks to this work and the dissertation, we believe that, the developed transformation techniques for the scalar-to-polarized optical field mappings can be used in wide-viewing-angle holographic display applications. Although the conventional scalar field generation method can be used to obtain the desired scalar results only in paraxial fields, the developed algorithms make the scalar theory of light useful in wide-angle fields.

# Bibliography

- [1] D. Gabor, “A new microscopic principle,” *Nature*, vol. 161, pp. 777–778, 1948.
- [2] H. M. Ozaktas, “Three-dimensional television: Consumer, social, and gender issues,” in *Three-Dimensional Television Capture, Transmission Display*, pp. 599–629, Heidelberg: Springer-Verlag Berlin Heidelberg, 2008.
- [3] M. Born and E. Wolf, *Principles of Optics: Electromagnetic Theory of Propagation, Interference and Diffraction of Light*. Cambridge: Cambridge University Press, 7th ed., 1999.
- [4] J. W. Goodman, *Introduction to Fourier Optics*. New York: McGraw-Hill, 2nd ed., 1996.
- [5] C. J. Bouwkamp, “Diffraction theory,” *Reports on Progress in Physics*, vol. 17, no. 1, p. 35, 1954.
- [6] R. K. Luneburg and M. Herzberger, *Mathematical Theory of Optics*. Los Angeles: University of California Press, 1964.
- [7] J. D. Gaskill, *Linear Systems, Fourier Transforms, and Optics*. Hoboken, New Jersey: Wiley, 1978.
- [8] H. M. Ozaktas, Z. Zalevsky, and M. A. Kutay, *The Fractional Fourier transform with applications in Optics and signal processing*. Hoboken, New Jersey: Wiley, 2001.
- [9] A. Papoulis, *Systems and Transforms With Applications in Optics*. McGraw-Hill, Robert Krieger Publishing Company, 1968.

- [10] E. Hecht, *Optics*. London: Pearson Education, 5th ed., 2016.
- [11] G. C. Sherman, “Application of the convolution theorem to Rayleigh’s integral formulas,” *Journal of the Optical Society of America*, vol. 57, no. 4, pp. 546–547, 1967.
- [12] B. E. A. Saleh and M. C. Teich, *Fundamentals of Photonics*. Hoboken, New Jersey: Wiley, 2nd ed., 2007.
- [13] Y. Shechtman, Y. C. Eldar, O. Cohen, H. N. Chapman, J. Miao, and M. Segev, “Phase retrieval with application to optical imaging: A contemporary overview,” *IEEE Signal Processing Magazine*, vol. 32, no. 3, pp. 87–109, 2015.
- [14] E. J. Candès, Y. C. Eldar, T. Strohmer, and V. Voroninski, “Phase retrieval via matrix completion,” *SIAM Review*, vol. 57, no. 2, pp. 225–251, 2015.
- [15] E. J. Candès, X. Li, and M. Soltanolkotabi, “Phase retrieval via Wirtinger flow: Theory and algorithms,” *IEEE Transactions on Information Theory*, vol. 61, no. 4, pp. 1985–2007, 2015.
- [16] J. Zhang, N. Pégard, J. Zhong, H. Adesnik, and L. Waller, “3D computer-generated holography by non-convex optimization,” *Optica*, vol. 4, no. 10, pp. 1306–1313, 2017.
- [17] J. R. Fienup, “Phase retrieval algorithms: a comparison,” *Applied Optics*, vol. 21, no. 15, pp. 2758–2769, 1982.
- [18] N. Antipa, G. Kuo, R. Heckel, B. Mildenhall, E. Bostan, R. Ng, and L. Waller, “Diffusercam: lensless single-exposure 3D imaging,” *Optica*, vol. 5, no. 1, pp. 1–9, 2018.
- [19] M. Rostykus, F. Soulez, M. Unser, and C. Moser, “Compact lensless phase imager,” *Optics Express*, vol. 25, no. 4, pp. 4438–4445, 2017.
- [20] Y. Rivenson, A. Stern, and B. Javidi, “Overview of compressive sensing techniques applied in holography,” *Applied Optics*, vol. 52, no. 1, pp. A423–A432, 2013.

- [21] E. N. Leith and J. Upatnieks, “Reconstructed wavefronts and communication theory,” *Journal of the Optical Society of America*, vol. 52, no. 10, pp. 1123–1130, 1962.
- [22] Y. N. Denisyuk, “Photographic reconstruction of the optical properties of an object in its own scattered radiation field,” in *Soviet Physics Doklady*, vol. 7, p. 543, 1962.
- [23] H. J. Caulfield, *Handbook of optical holography*. New York: Academic Press, 2012.
- [24] T. Kreis, *Handbook of Holographic Interferometry*. Hoboken, New Jersey: Wiley, 2005.
- [25] G. Nehmetallah and P. P. Banerjee, “Applications of digital and analog holography in three-dimensional imaging,” *Advances in Optics and Photonics*, vol. 4, pp. 472–553, Dec 2012.
- [26] G. Saxby, *Practical Holography*. CRC Press, 3rd ed., 2003.
- [27] G. Nehmetallah, R. Aylo, and L. Williams, *Analog and Digital Holography with MATLAB*. SPIE, 2015.
- [28] L. Onural and P. D. Scott, “Digital decoding of in-line holograms,” *Optical Engineering*, vol. 26, no. 11, p. 261124, 1987.
- [29] V. M. Bove, “Display holography’s digital second act,” *Proceedings of the IEEE*, vol. 100, no. 4, pp. 918–928, 2012.
- [30] L. Onural, A. Gotchev, H. M. Ozaktas, and E. Stoykova, “A survey of signal processing problems and tools in holographic three-dimensional television,” *IEEE Transactions on Circuits and Systems for Video Technology*, vol. 17, no. 11, pp. 1631–1646, 2007.
- [31] L. Onural, F. Yaras, and H. Kang, “Digital holographic three-dimensional video displays,” *Proceedings of the IEEE*, vol. 99, no. 4, pp. 576–589, 2011.
- [32] F. Yaras, H. Kang, and L. Onural, “State of the art in holographic displays: A survey,” *Journal of Display Technology*, vol. 6, no. 10, pp. 443–454, 2010.

- [33] J. Geng, “Three-dimensional display technologies,” *Advances in Optics and Photonics*, vol. 5, no. 4, pp. 456–535, 2013.
- [34] E. Lueder, *3D Displays*. Hoboken, New Jersey: Wiley, 2011.
- [35] Y. Lim, K. Hong, H. Kim, H.-E. Kim, E.-Y. Chang, S. Lee, T. Kim, J. Nam, H.-G. Choo, J. Kim, and J. Hahn, “360-degree tabletop electronic holographic display,” *Optics Express*, vol. 24, no. 22, pp. 24999–25009, 2016.
- [36] T. Inoue and Y. Takaki, “Table screen 360-degree holographic display using circular viewing-zone scanning,” *Optics Express*, vol. 23, no. 5, pp. 6533–6542, 2015.
- [37] E.-Y. Chang, J. Choi, S. Lee, S. Kwon, J. Yoo, M. Park, and J. Kim, “360-degree color hologram generation for real 3D objects,” *Applied Optics*, vol. 57, no. 1, pp. A91–A100, 2018.
- [38] F. Yaraş, H. Kang, and L. Onural, “Circular holographic video display system,” *Optics Express*, vol. 19, no. 10, pp. 9147–9156, 2011.
- [39] F. Yaraş, H. Kang, and L. Onural, “Real-time phase-only color holographic video display system using LED illumination,” *Applied Optics*, vol. 48, no. 34, pp. H48–H53, 2009.
- [40] B. Javidi and F. Okano, eds., *Three-Dimensional Television, Video, and Display Technologies*. Heidelberg: Springer-Verlag Berlin Heidelberg, 2002.
- [41] H. Ozaktas and L. Onural, eds., *Three-Dimensional Television: Capture, Transmission, Display*. Heidelberg: Springer-Verlag Berlin Heidelberg, 2008.
- [42] H. Sasaki, K. Yamamoto, K. Wakunami, Y. Ichihashi, R. Oi, and T. Senoh, “Large size three-dimensional video by electronic holography using multiple spatial light modulators,” *Scientific Reports*, vol. 4, 2014.
- [43] Z. Zeng, H. Zheng, Y. Yu, A. K. Asundi, and S. Valyukh, “Full-color holographic display with increased-viewing-angle,” *Applied Optics*, vol. 56, no. 13, pp. F112–F120, 2017.

- [44] T. Kozacki and M. Chlipala, “Color holographic display with white light LED source and single phase only SLM,” *Optics Express*, vol. 24, no. 3, pp. 2189–2199, 2016.
- [45] L. Onural, *3D Video Technologies: An Overview of Research Trends*. SPIE, 2011.
- [46] L. Onural, “Television in 3-D: What are the prospects?,” *Proceedings of the IEEE*, vol. 95, no. 6, pp. 1143–1145, 2007.
- [47] L. Onural and H. M. Ozaktas, “Signal processing issues in diffraction and holographic 3DTV,” in *13th European Signal Processing Conference*, (Antalya, Turkey), pp. 1–4, Sept 2005.
- [48] T. Kozacki, “Holographic display with tilted spatial light modulator,” *Applied Optics*, vol. 50, no. 20, pp. 3579–3588, 2011.
- [49] M. Yamaguchi, “Light-field and holographic three-dimensional displays,” *Journal of the Optical Society of America A*, vol. 33, no. 12, pp. 2348–2364, 2016.
- [50] T. M. Kreis, “Frequency analysis of digital holography,” *Optical Engineering*, vol. 41, no. 4, pp. 771–778, 2002.
- [51] L. Yaroslavsky, *Digital holography and digital image processing: principles, methods, algorithms*. Heidelberg: Springer, 2004.
- [52] H. Urey, K. V. Chellappan, E. Erden, and P. Surman, “State of the art in stereoscopic and autostereoscopic displays,” *Proceedings of the IEEE*, vol. 99, no. 4, pp. 540–555, 2011.
- [53] B. Javidi, E. Tajahuerce, and P. Andres, eds., *Multi-dimensional imaging*. Hoboken, New Jersey: Wiley, 2014.
- [54] P. Benzie, J. Watson, P. Surman, I. Rakkolainen, K. Hopf, H. Urey, V. Sainov, and C. von Kopylow, “A survey of 3DTV displays: Techniques and technologies,” *IEEE Transactions on Circuits and Systems for Video Technology*, vol. 17, no. 11, pp. 1647–1658, 2007.

- [55] T. Okoshi, *Three-Dimensional Imaging Techniques*. New York: Academic Press, 1976.
- [56] L. Onural and M. T. Özgen, “Extraction of three-dimensional object-location information directly from in-line holograms using Wigner analysis,” *Journal of the Optical Society of America A*, vol. 9, no. 2, pp. 252–260, 1992.
- [57] M. Testorf, B. Hennelly, and J. Ojeda-Castaneda, *Phase-Space Optics: Fundamentals and Applications: Fundamentals and Applications*. New York: McGraw-Hill, 2009.
- [58] G. W. Forbes, V. I. Man’ko, H. M. Ozaktas, R. Simon, and K. B. Wolf, “Wigner distributions and phase space in optics,” *Journal of the Optical Society of America A*, vol. 17, no. 12, pp. 2274–2274, 2000.
- [59] M. A. Alonso, “Wigner functions in optics: describing beams as ray bundles and pulses as particle ensembles,” *Advances in Optics and Photonics*, vol. 3, no. 4, pp. 272–365, 2011.
- [60] P. Yeh and C. Gu, *Optics of Liquid Crystal Displays*. Hoboken, New Jersey: Wiley, 2nd ed., 2009.
- [61] Z. Zhang, Z. You, and D. Chu, “Fundamentals of phase-only liquid crystal on silicon (LCOS) devices,” *Light: Sci. & Appl.*, vol. 3, no. 10, p. e213, 2014.
- [62] S. Osten, S. Krüger, and A. Steinhoff, “Spatial light modulators based on reflective micro-displays,” *Technisches Messen*, vol. 73, no. 3, pp. 149–156, 2006.
- [63] G. Lazarev, A. Hermerschmidt, S. Krüger, and S. Osten, “LCOS spatial light modulators: Trends and applications,” in *Optical Imaging and Metrology*, pp. 1–29, Hoboken, New Jersey: Wile, 2012.
- [64] O. Theimer, G. D. Wassermann, and E. Wolf, “On the foundation of the scalar diffraction theory of optical imaging,” *Proceedings of the Royal Society A*, vol. 212, no. 1110, pp. 426–437, 1952.

- [65] J. Kong, *Electromagnetic Wave Theory*. Hoboken, New Jersey: Wiley, 1986.
- [66] J. Hahn, H. Kim, Y. Lim, G. Park, and B. Lee, “Wide viewing angle dynamic holographic stereogram with a curved array of spatial light modulators,” *Optics Express*, vol. 16, no. 16, pp. 12372–12386, 2008.
- [67] A. V. Oppenheim, R. W. Schaffer, and J. R. Buck, *Discrete-Time Signal Processing*. Upper Saddle River, New Jersey: Prentice Hall, 2nd ed., 1999.
- [68] L. Onural, “Impulse functions over curves and surfaces and their applications to diffraction,” *Journal of Mathematical Analysis and Applications*, vol. 322, no. 1, pp. 18 – 27, 2006.
- [69] C. A. Balanis, *Advanced Engineering Electromagnetics*. Hoboken, New Jersey: Wiley, 2nd ed., 2012.
- [70] C. A. Balanis, *Antenna Theory: Analysis and Design*. Hoboken, New Jersey: Wiley, 3rd ed., 2005.
- [71] R. E. Collin, *Antennas and Radiowave Propagation*. New York: McGraw-Hill, 1985.
- [72] D. Rhodes, “On the stored energy of planar apertures,” *IEEE Transactions on Antennas and Propagation*, vol. 14, no. 6, pp. 676–683, 1966.
- [73] G. Borgiotti, “Fourier transforms method in aperture antennas problems,” *Alta Frequenza*, vol. 32, no. 32, pp. 196–204, 1963.
- [74] O. Kulce, L. Onural, and H. M. Ozaktas, “Evaluation of the validity of the scalar approximation in optical wave propagation using a systems approach and an accurate digital electromagnetic model,” *Journal of Modern Optics*, vol. 63, no. 21, pp. 2382–2391, 2016.
- [75] O. Kulce and L. Onural, “Analysis of the longitudinal component of the electric field generated by flat and pixelated liquid crystal displays,” in *2016 3DTV-Conference: The True Vision - Capture, Transmission and Display of 3D Video (3DTV-CON)*, (Hamburg, Germany), pp. 1–4, July 2016.

- [76] O. Kulce and L. Onural, “Local error analysis arising from the conventional scalar approximation in wide optical fields,” in *25th Signal Processing and Communications Applications Conference (SIU)*, (Antalya, Turkey), pp. 1–4, May 2017.
- [77] C. G. Chen, P. T. Konkola, J. Ferrera, R. K. Heilmann, and M. L. Schattenburg, “Analyses of vector Gaussian beam propagation and the validity of paraxial and spherical approximations,” *Journal of the Optical Society of America A*, vol. 19, no. 2, pp. 404–412, 2002.
- [78] P. C. Chaumet, “Fully vectorial highly nonparaxial beam close to the waist,” *Journal of the Optical Society of America A*, vol. 23, no. 12, pp. 3197–3202, 2006.
- [79] W. H. Carter, “Electromagnetic field of a Gaussian beam with an elliptical cross section,” *Journal of the Optical Society of America A*, vol. 62, no. 10, pp. 1195–1201, 1972.
- [80] A. Erdélyi, W. Magnus, and F. Oberhettinger, *Tables of Integral Transforms*. New York: McGraw-Hill, 1954.
- [81] R. Martínez-Herrero, P. M. Mejías, and G. Piquero, *Characterization of Partially Polarized Light Fields*. Heidelberg: Springer-Verlag Berlin Heidelberg, 2009.
- [82] A. S. Marathay and G. B. Parrent, “Use of scalar theory in optics,” *Journal of the Optical Society of America*, vol. 60, no. 2, pp. 243–245, 1970.
- [83] P. Varga and P. Török, “The Gaussian wave solution of Maxwell’s equations and the validity of scalar wave approximation,” *Optics Communications*, vol. 152, no. 1-3, pp. 108–118, 1998.
- [84] A. Carnicer, I. Juvells, D. Maluenda, R. Martínez-Herrero, and P. M. Mejías, “On the longitudinal component of paraxial fields,” *European Journal of Physics*, vol. 33, no. 5, p. 1235, 2012.
- [85] H. S. Green and E. Wolf, “A scalar representation of electromagnetic fields,” *Proceedings of the Physical Society A*, vol. 66, no. 12, pp. 1129–1137, 1953.

- [86] E. Wolf, “A scalar representation of electromagnetic fields: II,” *Proceedings of the Physical Society*, vol. 74, no. 3, pp. 269–280, 1959.
- [87] P. Roman, “A scalar representation of electromagnetic fields: III,” *Proceedings of the Physical Society*, vol. 74, no. 3, pp. 281–289, 1959.
- [88] R. Mersereau, “The processing of hexagonally sampled two-dimensional signals,” *Proceedings of the IEEE*, vol. 67, no. 6, pp. 930–949, 1979.
- [89] L. Onural, “Some mathematical properties of the uniformly sampled quadratic phase function and associated issues in digital Fresnel diffraction simulations,” *Optical Engineering*, vol. 43, no. 11, pp. 2557–2563, 2004.
- [90] A. D. Poularikas, ed., *Transforms and Applications Handbook*. Boca Raton: CRC Press, 3rd ed., 2010.
- [91] G. B. Esmer, “Computation of holographic patterns between tilted planes,” Master’s thesis, Bilkent University, 2004.
- [92] G. B. Esmer and L. Onural, “Simulation of scalar optical diffraction between arbitrarily oriented planes,” in *1st International Symposium on Control, Communications and Signal Processing*, (Hammamet, Tunisia), pp. 225–228, March 2004.
- [93] N. Delen and B. Hooker, “Free-space beam propagation between arbitrarily oriented planes based on full diffraction theory: a fast Fourier transform approach,” *Journal of the Optical Society of America A*, vol. 15, no. 4, pp. 857–867, 1998.
- [94] T. Tommasi and B. Bianco, “Computer-generated holograms of tilted planes by a spatial frequency approach,” *Journal of the Optical Society of America A*, vol. 10, no. 2, pp. 299–305, 1993.
- [95] T. Tommasi and B. Bianco, “Frequency analysis of light diffraction between rotated planes,” *Optics Letters*, vol. 17, no. 8, pp. 556–558, 1992.
- [96] L. Onural, “Exact solution for scalar diffraction between tilted and translated planes using impulse functions over a surface,” *Journal of the Optical Society of America A*, vol. 28, no. 3, pp. 290–295, 2011.

- [97] O. Kulce and L. Onural, “Power spectrum equalized scalar representation of wide-angle optical field propagation,” *Journal of Mathematical Imaging and Vision*, 2018.
- [98] G. B. Esmer, V. Uzunov, L. Onural, H. M. Ozaktas, and A. Gotchev, “Diffraction field computation from arbitrarily distributed data points in space,” *Signal Processing: Image Communication*, vol. 22, no. 2, pp. 178 – 187, 2007.
- [99] G. B. Esmer, L. Onural, and H. M. Ozaktas, “Exact diffraction calculation from fields specified over arbitrary curved surfaces,” *Optics Communications*, vol. 284, no. 24, pp. 5537 – 5548, 2011.
- [100] E. Şahin and L. Onural, “Scalar diffraction field calculation from curved surfaces via Gaussian beam decomposition,” *Journal of the Optical Society of America A*, vol. 29, no. 7, pp. 1459–1469, 2012.
- [101] E. Şahin and L. Onural, “Calculation of the scalar diffraction field from curved surfaces by decomposing the three-dimensional field into a sum of Gaussian beams,” *Journal of the Optical Society of America A*, vol. 30, no. 3, pp. 527–536, 2013.
- [102] O. Kulce and L. Onural, “Phase retrieval from electric field intensity for wide angle optical fields,” in *Imaging and Applied Optics 2017 (3D, AIO, COSI, IS, MATH, pcAOP)*, p. CTu1B.4, June 2017.
- [103] A. M. Grigoryan, E. R. Dougherty, and S. S. Aghaian, “Optimal Wiener and homomorphic filtration: Review,” *Signal Processing*, vol. 121, pp. 111 – 138, 2016.
- [104] A. M. Grigoryan and E. R. Dougherty, “Optimization of linear filters under power-spectral-density stabilization,” *IEEE Transactions on Signal Processing*, vol. 49, pp. 2292–2300, 2001.
- [105] T. M. Cannon, *Digital image deblurring by nonlinear homomorphic filtering*. PhD thesis, Computer Science Department, University of Utah, 1974.

- [106] H. C. Andrews and B. R. Hunt, *Digital Image Restoration*. New Jersey: Prentice-Hall Inc., 1977.
- [107] M. Johansson, H. S. Lui, J. C. Bolomey, and M. Persson, “Source modeling using phaseless low-frequency near-field measurements,” *IEEE Transactions on Electromagnetic Compatibility*, vol. 54, no. 3, pp. 613–624, 2012.
- [108] T. Isernia, G. Leone, and R. Pierri, “Radiation pattern evaluation from near-field intensities on planes,” *IEEE Transactions on Antennas and Propagation*, vol. 44, no. 5, pp. 701–, 1996.
- [109] F. Las-Heras and T. K. Sarkar, “A direct optimization approach for source reconstruction and NF-FF transformation using amplitude-only data,” *IEEE Transactions on Antennas and Propagation*, vol. 50, no. 4, pp. 500–510, 2002.
- [110] T. Moon and W. Stirling, *Mathematical Methods and Algorithms for Signal Processing*. Upper Saddle River, New Jersey: Prentice Hall, 2000.
- [111] E. J. Fuselier and G. B. Wright, “Stability and error estimates for vector field interpolation and decomposition on the sphere with RBFs,” *SIAM Journal on Numerical Analysis*, vol. 47, no. 5, pp. 3213–3239, 2009.
- [112] M. Fan, D. Paul, T. Lee, and T. Matsuo, “Modeling tangential vector fields on a sphere,” *Journal of the American Statistical Association*, vol. 0, no. ja, pp. 0–0, 2017.
- [113] F. J. Narcowich, J. D. Ward, and G. B. Wright, “Divergence-free RBFs on surfaces,” *Journal of Fourier Analysis and Applications*, vol. 13, no. 6, pp. 643–663, 2007.
- [114] E. J. Fuselier, F. J. Narcowich, J. D. Ward, and G. B. Wright, “Error and stability estimates for surface-divergence free RBF interpolants on the sphere,” *Mathematics of Computation*, vol. 78, no. 268, pp. 2157–2186, 2009.
- [115] G. B. Esmer, L. Onural, H. M. Ozaktas, V. Uzunov, and A. Gotchev, “Performance assessment of a diffraction field computation method based

on source model,” in *2008 3DTV Conference: The True Vision - Capture, Transmission and Display of 3D Video (3DTV-CON)*, pp. 257–260, May 2008.

- [116] A. Symeonidou, D. Blinder, and P. Schelkens, “Colour computer-generated holography for point clouds utilizing the Phong illumination model,” *Optics Express*, vol. 26, no. 8, pp. 10282–10298, 2018.
- [117] R. H.-Y. Chen and T. D. Wilkinson, “Computer generated hologram from point cloud using graphics processor,” *Applied Optics*, vol. 48, no. 36, pp. 6841–6850, 2009.
- [118] I. S. Gradshteyn and I. M. Ryzhik, *Table of Integrals, Series, and Products*. San Diego: Academic Press, 7th ed., 2007.

# Appendix A

## Proof of the Energy of the Filter Functions $\mathcal{G}_{\{x,y\},p}(\hat{\mathbf{k}})$ Being Infinite

Here we prove that the energy of the filters in the propagating case are infinite. We give the analysis only for the filter  $\mathcal{G}_{x,p}(\hat{\mathbf{k}})$  since the analysis for  $\mathcal{G}_{y,p}(\hat{\mathbf{k}})$  is the same.

The energy of  $\mathcal{G}_{x,p}^{polar}(\kappa, \phi)$ ,  $\varepsilon_{\kappa'}$  function, that is defined in Equation 2.24, for the interval  $0 \leq \kappa \leq \kappa'$  can be written as

$$\begin{aligned}\varepsilon_{\kappa'} &= \frac{1}{4\pi^2} \int_0^{2\pi} \int_0^{\kappa'} |\mathcal{G}_{x,p}^{polar}(\kappa, \phi)|^2 \kappa d\kappa d\phi \\ &= \frac{1}{4\pi^2} \int_0^{2\pi} \cos^2 \phi \int_0^{\kappa'} \frac{\kappa^3}{k^2 - \kappa^2} d\kappa d\phi\end{aligned}\tag{A.1}$$

Then,

$$\begin{aligned}
\int_0^{\kappa'} \frac{\kappa^3}{k^2 - \kappa^2} d\kappa &= -\frac{\kappa^2}{2} \Big|_{\kappa=0}^{\kappa=\kappa'} + k^2 \int_0^{\kappa'} \frac{\kappa}{k^2 - \kappa^2} d\kappa \\
&= -\frac{\kappa'^2}{2} - \frac{k^2}{2} \ln(1 - \kappa^2) \Big|_{\kappa=0}^{\kappa=\frac{\kappa'}{k}} \\
&= -\frac{\kappa'^2}{2} - \frac{k^2}{2} \ln \left[ 1 - \left( \frac{\kappa'}{k} \right)^2 \right]
\end{aligned} \tag{A.2}$$

The integrals in Equation A.2 are obtained from [118]. When  $\kappa'$  goes to  $k$ , as a result of the logarithm in Equation A.2, the energy of  $\mathcal{G}_{x,p}(k_x, k_y)$  tends to infinity. If we choose  $\kappa' < k$ , then the energy of the filter function for  $0 \leq \kappa \leq \kappa'$  becomes

$$-\frac{\kappa'^2}{8\pi} - \frac{k^2}{8\pi} \ln \left[ 1 - \left( \frac{\kappa'}{k} \right)^2 \right] . \tag{A.3}$$